8-2003

"Enhancement of Sensitivity and Selectivity of Chemical Sensors Through Thin Film Coatings and Surface Modifications

Joseph Jeremy Headrick
University of Tennessee - Knoxville

To the Graduate Council:

I am submitting herewith a dissertation written by Joseph Jeremy Headrick entitled ""Enhancement of Sensitivity and Selectivity of Chemical Sensors Through Thin Film Coatings and Surface Modifications." I have examined the final electronic copy of this dissertation for form and content and recommend that it be accepted in partial fulfillment of the requirements for the degree of Doctor of Philosophy, with a major in Chemistry.

Dr. Michael J. Sepaniak, Major Professor

We have read this dissertation and recommend its acceptance:

Dr. James Q. Chambers, Dr. Ben Xue, Dr. Panos Datskos

Accepted for the Council:

Carolyn R. Hodges

Vice Provost and Dean of the Graduate School

(Original signatures are on file with official student records.)

To the Graduate Council:

I am submitting herewith a dissertation written by Joseph Jeremy Headrick entitled “Enhancement of Sensitivity and Selectivity of Chemical Sensors Through Thin Film Coatings and Surface Modifications.” I have examined the final electronic copy of this dissertation for form and content and recommend that it be accepted in partial fulfillment of the requirements for the degree of Doctor of Philosophy, with a major in Chemistry.

Dr. Michael J. Sepaniak
Major Professor

We have read this dissertation
and recommend its acceptance:

Dr. James Q. Chambers
Dr. Ben Xue
Dr. Panos Datskos

Accepted for the Council:
Dr. Anne Mayhew
Vice Provost and
Dean of Graduate Studies

(Original signatures are on file with official student records.)

ENHANCEMENT OF SENSITIVITY AND SELECTIVITY OF CHEMICAL SENSORS THROUGH THIN FILM COATINGS AND SURFACE MODIFICATIONS

A Dissertation

Presented for the

Doctor of Philosophy Degree

The University of Tennessee, Knoxville

Joseph Jeremy Headrick

August 2003

DEDICATION

This dissertation is dedicated to my parents,

Bob and Judy Headrick,

whose love and support have made all my endeavors possible,

and to my wife Sarah

for being my encourager, my confidant, my colleague,

and above all my friend.

ACKNOWLEDGMENTS

I would like to thank the people who have assisted in the fulfillment of this body of work. I owe my parents and family much gratitude for their love and support, which has made this possible. I thank my wife for her support, understanding and patience as I completed this project.

To past group members Tim Gibson, Will Nirode, Brian Fagan, and Jim Schaeper I would like to thank for all the insight that you provided me with and for the many conversations we had, both scientific and marginal. To present group members Chris Tipple, Shannon Fox, Marco DeJesus, Maggie Connaster Kathleen Giesfeldt, Lance Riddle, and Joe Payne thanks for all your help and assistance and good luck to you all. I would also like to thank my committee members (Dr. Chambers, Dr. Datskos, and Dr. Xue) for their time.

Finally, I would like to thank my advisor Dr. Mike Sepaniak, for all the guidance and advice he has provided me. It has been an experience I will never forget.

ABSTRACT

Chemical sensors have become major analytical tools for how we monitor and obtain information about the chemical nature of ourselves and our surroundings. Two characteristics of chemical sensors that are under constant development and improvement are their selectivity and their sensitivity. Selectivity is a concern of any chemical sensor, without it the signal obtained by a chemical sensor cannot be related to the target species concentration with any confidence. With chemical sensors the selectivity is generally created by the used of a chemical recognition layer such as a permeable membrane, or a thin chemical film. The sensitivity of a chemical sensor is a concern, as with any quantitative analytical method, so that small differences in analyte concentration are distinguishable and trace analysis can be performed. In this work the selectivity and sensitivity of two distinctly different devices used as chemical sensors are investigated. The first device combines a scintillation fiber with a selective polymer coating to create a chemical sensor selective for ^{137}Cs. Both the selectivity and sensitivity of the scintillation fiber are improved with the addition of the chemical recognition layer. The second device investigated is a microcantilever sensor. Microcantilevers have been used to monitor chemicals present in both air and liquid environments. However, in moving from measurements made in air to measurements made in liquids, a great deal of sensitivity is lost due to differences in the interfacial energies of the

microcantilevers in these two different environments. To overcome this limitation surface modification of the microcantilevers was investigated to improve the sensitivity of these devices. Surfaces of the microcantilevers were modified by several different methods, the binding of gold nanobeads to the surface, creation of a roughened dealloyed surface, and the physical milling and chemical etching of grooves into the surface of the microcantilevers, each of these surface modifications was shown to enhance the sensitivity of microcantilever chemical senors over microcantilever chemical sensors with smooth surfaces.

PREFACE

Chapter 1 is intended to introduce the reader to the basic concepts of chemical sensors. Descriptions of the four major areas of chemical sensors, thermal, electrochemical, optical, and mass, are discussed.

Chapter 2 discusses the development of a chelating scintillation fiber for use in the detection of radioactive materials. The major focus is the improvement of the selectivity and sensitivity of the chelating scintillation fiber over the traditional scintillation fiber.

Chapter 3 details the development of a disordered dealloyed surface structure for use with microcantilever sensors.

Chapter 4 examines further the effect of organized surface modifications on the sensitivity of microcantilevers.

Chapter 5 details some interesting other sensor work that was performed but did not reach a mature state, as well as provides a summary and conclusions to the body of work.

TABLE OF CONTENTS

Chapter Page

1: INTRODUCTION TO SENSOR TECHNOLOGIES……1

1.1 INTRODUCTION……1

1.2 HISTORICAL PERSCPECTIVE OF CHEMICAL SENSORS……..3

1.3 BASIC COMPONENTS OF CHEMICAL SENSORS……4

1.3.1 Recognition Layers…… 7

1.3.2 Transducers…….. 8

1.4 TYPES OF CHEMICAL SENSORS……9

1.4.1 Thermal Sensors…….. 9

Thermistors…….... 11

Catalytic Gas Sensors…… 13

Thermal Conductivity Sensors…….. 14

1.4.2 Electrochemical Sensors……... 17

Amperometric Sensors…….. 17

Potentiometric Sensors…… 20

Conductometric Sensors……... 26

1.4.3 Optical Sensors…… 26

1.4.4 Mass Sensors……34

Bulk Acoustic Wave Sensors……35

Surface Acoustic Wave Sensors……..37

Microcantilever Sensors…… 37

1.5 STATEMENT OF PROBLEM.....45

2: CHELATING SCINTILLATION FIBERS FOR MEASUREMENT OF ^{137}CS..... 48

2.1 INTRODUCTION.....48

2.2 EXPERIMENTAL SECTION..... 52

2.2.1 Instrumentation..... 52

2.2.2 Cs Selective DMBP..... 53

2.2.3 Materials and Chemicals..... 54

2.2.4 Coating of Scintillation Fibers..... 54

2.3 RESULTS AND DISCUSSION.....55

2.3.1 Signal Considerations..... 55

2.3.2 Coating Thickness Studies..... 60

2.3.3 Reproducibility..... 62

2.3.4 Fiber Uptake Kinetics With and Without Potential Interferences..... 63

2.3.5 Calibration Plots With and Without Potential Interferences..... 68

2.3.6 Non-Specific Resin Studies..... 72

2.4 CONCLUSIONS.....72

3: ENHANCED CHEMI-MECHANICAL TRANSDUCTION AT NANOSTRUCTURED INTERFACES.....74

3.1 INTRODUCTION.....74

3.2 EXPERIMENTAL SECTION..... 76

3.2.1 Materials and Chemicals..... 76

3.2.2 Instrumentation..... 78

3.2.3 Preparation of Cantilever Surfaces..... 80

3.3 RESULTS AND DISCUSSION.....82

3.4 CONCLUSIONS.....91

4: ENHANCING CHEMI-MECHANICAL TRANSDUCTION IN MICROCANTILEVER CHEMICAL SENSING BY SURFACE MODIFICATION.....93

4.1 INTRODUCTION.....93

4.2 EXPERIMENTAL SECTION.....97

4.3 RESULTS AND DISCUSSION.....103

4.4 CONCLUSIONS.....113

5: MISCELLANEOUS WORK AND CONCLUDING REMARKS.....114

5.1 INTRODUCTION.....114

5.2 b -PARTICLE DETECTION WITH MCs.....114

5.3 MATRIX ASSISTED PULSED LASER EVAPORATION (MAPLE)..... 116

5.4 CONCLUDING REMARKS.....122

REFERENCES..... 125

VITA..... 138

LIST OF FIGURES

Figure Page

1.1 Basic components of a chemical sensor……... 6

1.2 A thermistor sensor…….. 12

1.3 A typical pellistor sensor…….. 15

1.4 A thermal conductivity detector…….. 16

1.5 Schematic of a carbon paste electrode……. 19

1.6 Ion-selective electrode geometry for a bench or dip-type electrode…… 21

1.7 Schematic of an insulated gate field-effect transistor (IGFET)…….. 24

1.8 Schematic of a field-effect transistor with a chemical recognition layer (CHEMFET)…… 25

1.9 Diagram of fiber optic waveguide and conditions to achieve total internal reflection……..28

1.10 Modes of optical fiber use in sensors……. 30

1.11 Absorption and Emission bands of polystyrene fiber core……. 32

1.12 Light attenuation of different wavelengths of light through a polystyrene core fiber……. 33

1.13 Quartz crystal microbalance……. 36

1.14 Schematic of a typical surface acoustic wave (SAW) device……. 38

1.15 Focused Ion Beam image of a one-dimensional array of silicon microcantilevers……. 40

1.16 Transduction principles that are operative with microcantilever sensors ……. 41

1.17 Schematic of optical lever read-out arrangement for microcantilever sensing…… 46

2.1 Cesium selective dual mechanism bifunctional polymer…… 51

2.2 Cross sectional views of coated scintillation fiber…… 57

2.3 Signal and background versus percent epoxy and particles coating the fiber …… 61

2.4 Signal counts versus equilibration time…… 64

2.5 Signal counts versus activity for fibers measuring ^{137}Cs…… 69

2.6 Signal counts versus activity for fibers measuring ^{137}Cs in the presence of 10^{-5} M each of Cs (I), Rb (I), and Al (III)…….. 71

3.1 Preparation scheme of heptakis-6-mercapto-β-cyclodextrin……... 77

3.2 Image of gravity fed liquid flow cell used in microcantilever setup…… 79

3.3 Schematic Illustration of the techniques used in this study to prepare gold nanostructures…….. 81

3.4 AFM images of gold nanospheres assembly and 20nm thick dealloyed gold coating……... 83

3.5 Enhanced responses of β-cyclodextrin modified microcantilevers to DMN as a result of nanostructuring the gold coated side……... 86

3.6 Comparison of the sensitivities of receptor coated microcantilevers for two test analytes…… 87

4.1 Focused ion beam image of grooved microcantilever with 400nm deep grooves…… 98

4.2 V-shaped grooved microcantilever prepared by Ga^{+} doping of silicon surface and subsequent anisotropic etching with KOH…… 100

4.3 Monomeric units and general shape of the functionalized

cyclodextrins used as receptor phases. …….. 101

4.4 Response curves for surface modified microcantilevers to 2,3-DHN…… 105

4.5 Response curve of a 400nm deep grooved microcantilever to a series of VOCs…… 108

4.6 Responses of a 400nm deep grooved microcantilever coated with MeSi-β-CD to trichloroethylene……...109

4.7 Response of a 400nm deep grooved microcantilever to trichloroethylene after thinning of the microcantilever surface…….. 111

4.8 Response of an ungrooved MC and a V-shaped grooved MC to 8-hydroxyquinoline…….. 112

5.1 Schematic of vacuum pumped matrix assisted pulsed laser evaporation (MAPLE) system…… 118

5.2 IR spectra of bulk SP-2100 and thin film SP-2100 deposited by the MAPLE technique…… 119

5.3 Image of setup for matrix assisted pulsed laser evaporation direct-write (MAPLE DW)…… 121

LIST OF TABLES

Table Page

1.1 Historical landmarks in the development of chemical sensors……... 5

1.2 Major sensor transducer technologies…….. 10

2.1 Hanford DSSF 101-AW stock and diluted simulant composition…….. 66

3.1 Comparison of limits of detection and enhancement factors for Nanonstructured surfaces with HM-β-CD receptor phases……. 89

3.2 Comparison of the LODs achieved for liquid–phase measurements for the analytes 2,3-DHN, 2-7-DHN, tolazoline, and ephedrine on smooth and dealloyed gold surfaces……. 90

ABBREVIATIONS AND SYMBOLS

b^-	beta particle
γ	gamma particle
υ	Poisson's ratio
γ	surface free energy
q_1	incident angle
q_2	refracted angle
q_c	critical angle
q_{max}	maximum launch angle
σ_{app}	apparent surface stress
σ^{eff}	effective differential stress
ε_e	elastic surface strain
μCi	microcurie
μm	micrometer
μM	micromolar
2,3-DHN	2,3-dihydroxynaphthalene
A	area
A_{abs}	absolute activity of source
AC	alternating current
AFM	atomic force microscopy
a_i	activity of the i^{th} species

A_R	activity of resin bound ^{137}Cs
$A_{S,0}$	initial activity of ^{137}Cs in sample solution
B	measurement bandwidth
BAW	bulk acoustic wave
C	constant term
CCD	charge couple device
CD	cyclodextrin
CHEMFET	chemical field-effect transistor
Ci	curie
cm	centimeter
D	diffusion coefficient
D	distribution coefficient
DI	deionized
diss	dissociations
DMBP	dual mechanism bifunctional polymer
DMN	2,7-dimethylnaphthalene
DMSO	dimethoxy
DNAPL	dense non-aqueous phase liquid
DOE	department of energy
DSSF	double-shell slurry feed
e^-	electron
E	potential
E	Young's Modulus

$E^{0'}$	formal potential
EF	enhancement factor
ENFET	enzyme field-effect transistor
F	faraday
F_t	fraction of photons that reach PMT
f	frequency
f_{dir}	fraction emitted in proper direction
f_{ir}	fraction internally reflected toward PMT
$f_{opt/pmt}$	fraction transmitted by optical components
f_r	fundamental resonance frequency
FET	field-effect transisitor
FIB	focused ion beam
g	grams
GC	gas chromatography
h	hour
HM-β-CD	heptakis-6-mercapto-β-cyclodextrin
Hz	hertz
i	faradaic current
IGFET	insulated gate field effect transistor
ISE	ion-selective electrode
ISFET	ion-selective field-effect transistor
kHz	kilohertz
k	cantilever spring constant

K_B	Boltzman's constant
Kev	killo electron volts
l	length
LOD	limit of detection
m	mass
m	meter
m_o	effective suspended mass of MC
mg	milligram
ml	milliliter
mm	millimeter
mM	millimolar
mol	moles
M	molar
MC	microcantilever
meq	milliequivilants
MeSi-β-CD	(2,3-O-dimethyl-6-O-tertbutyl-dimethysiyl)-β-cyclodextrin
Mev	Mega electron volt
MIS	metal-insulator-semiconductor configuration
MW	milliWatt
n	number of electrons transfered
n_1	refractive index of core material
n_2	refractive index of cladding
nm	nanometer

N	newton
NA	numerical aperature
Ox	oxidized species
pg	picogram
ppb	parts per billion
ppm	parts per million
PMMA	polymethylmethacrylate
PMP	1-phenyl-3-mesityl-2-pyrazoline
PMT	photomultiplier tube
POPOP	1,4-bis-[2-(5-phenyloxazolyl)]-benzene
PSD	position sensitive photodetector
PVD	physical vapor deposition
Q	quality factor
QCM	quartz crystal microbalance
R	ideal gas constant
R	radius of curvature
Red	reduced species
RMS	root mean square
RSD	relative standard deviation
s	second
S/N	signal to noise ratio
SAM	self assembled monolayer
SAW	surface acoustic wave

Sig-cts	signal in counts per second
SPME	solid phase micro-extraction
t	thickness
T	absolute temperature
TCE	tetrachloroethylene
V	volt
V	volume
V_D	drain voltage
V_G	gate voltage
V_T	threshold voltage
VOC	volatile organic compound
z_{max}	deflection max

CHAPTER 1

INTRODUCTION TO SENSOR TECHNOLOGIES

1.1 INTRODUCTION

Everyday we make measurements, from simple measurements of ambient temperature to measurements that identify the constituents in complex mixtures. These measurements allow us to understand and to control our lives and the world around us. The methods we use to make these measurements are constantly evolving and being replaced with new methods that offer better, faster, cheaper, and more accurate information. The driving force behind the evolution of these methods is the desire to be able to acquire and apply information in real time so that we may have greater control over our surroundings.

The methods we use to acquire analytical information often involve the use of sensors. A sensor as defined by the Oxford English dictionary is a device that detects or measures a physical property and records, indicates or otherwise responds to it. Sensors can be categorized into two general categories. The first category is physical sensors that measure parameters such as temperature, pressure, electric charge, and light intensity. These sensors are some of the most advanced products of the evolution of the methods we use to acquire information. Some examples of physical sensors that are in common use include devices for temperature monitoring (thermocouples, or thermistors), piezoelectric

pressure monitors, flowmeters, humidity sensors, and light density sensors (photodiodes, charged-couple devices, and photomultipliers). A general definition of a physical sensor is a device that provides an electronic signal through which changes in a particular property within its immediate environment can be monitored[1]. Generally these sensors are nearly ideal in that they are sensitive, selective for the desired parameter, cheap, robust, and have reproducible behavior from batch to batch.

The second category of sensors is chemical and biological sensors (biosensors). It is this second category of sensors that is the subject of this dissertation, however most of these sensor systems contain within them physical sensors to convert the chemical information into an electronic or other analytically useful signal. A basic definition of a chemical sensor or a biosensor is a device which delivers information about the chemical nature of its surrounding environment, that consists of both a physical sensor and a chemically responsive layer[2]. While a chemical sensor or biosensor may contain a physical sensor at its core, its character is generally determined by a chemically selective film, layer, or membrane at the sensing area. The composition of this layer is crucial to the effectiveness of the sensor, as it controls the selectivity, sensitivity, lifetime, and response time of the device.

The differentiation between chemical sensors and biosensors is generally based upon the type of selective layer being used. Chemical sensors utilize polymer films, membranes, or low molecular weight materials as their selective layer, while biosensors use selective layers that consist of biomolecules, such as

enzymes, antibodies, receptors, or whole cells as part of the sensing process. Since all biomolecules can be considered chemicals in their own right, biosensors are essentially a subgroup of chemical sensors and from this point on will be referred to as such.

Chemical sensors are the products of many measurement systems based on many different types of technologies. They are based upon the methods of physical sensors, but also rely on chemistry, physics, electronics, and biology. Thus, chemical sensors represent multidisciplinary products that have emerged from the combined knowledge of these fields of science that are able to recognize specific chemical events and convert this recognition into some form of a useful output.

1.2 HISTORICAL PERSPECTIVE OF CHEMICAL SENSORS

Chemical sensors are relatively new types of measurement devices. Until the mid-1950's, the glass pH electrode could have been thought of as the only portable chemical sensor reliable enough to measure a chemical parameter. This sensor was invented in 1922[3], and had undergone three decades of development and was still limited to measurements in solution or on wet surfaces and had to be recalibrated often. In the 1950s other sensing technologies based on oxidation-reduction reactions at the surface of electrodes were developed which provided detection for metallic ions and some organic compounds[4-6]. The first application of these electrochemical methods to make a true chemical

sensor was for the measurement of the oxygen content of physiological fluids and tissues[7]. For this sensor, Clark encapsulated the electrodes and supporting chemical components with a semipermeable membrane that allowed the analyte to diffuse freely within the sensor without loss of critical components. This idea of a membrane separating the solution from the electrode also led to the first biosensor, a glucose sensor developed by Clark and Lyons[8]. Ion selective electrodes like these were the first transducers used for many different chemical sensors. Since this time the development of new transduction principles, such as piezoelectric devices[9], and microcantilevers[10, 11], and new methods of immobilizing recognition layers has led to the rapid evolution of chemical sensors and biosensors. Table 1.1 shows some of the major landmarks in the development of chemical and biological sensors.

1.3 BASIC COMPONENTS OF CHEMICAL SENSORS

Chemical sensors consist of some common basic components. These components include a recognition layer, a physical transducer, and the electronics and or software used to collect information from the device as shown in Figure 1.1. The recognition layer of a chemical sensor contains the components (polymeric layer, antibody, etc.) used to selectively monitor the chemical constituents within the environment of the sensor. The interaction between the recognition layer and the analyte of interest is detected by the transducer and the change in the transducer that results from the chemical

Table 1.1 Historic landmarks in the development of chemical sensors.

Date	Event	Reference
1922	First glass pH electrode	[3]
1925	First blood pH electrode	[12]
1954	Invention of the oxygen electrode	[7]
	Invention of pCO_2 electrode	[13]
1962	First amperometric biosensor	[8]
1964	Coated piezoelectric quartz sensor	[9]
1969	First potentiometric biosensor	[14]
1975	First binding protein biosensor	[15]
	Invention of pCO_2/pO_2 optode	[16]
1979	Surface acoustic wave sensors for gas	[17]
1980	Fiber optic pH sensor or in vivo blood gases	[18]
1982	Fiber optic based biosensor for glucose	[19]
1983	Fiber optical in-vivo measurements of interstitial fluids	[20]
1986	First tissue-based biosensor	[21]
1994	First microcantilever sensors	[10, 11]
2000	First chelating scintillation fibers	[22]

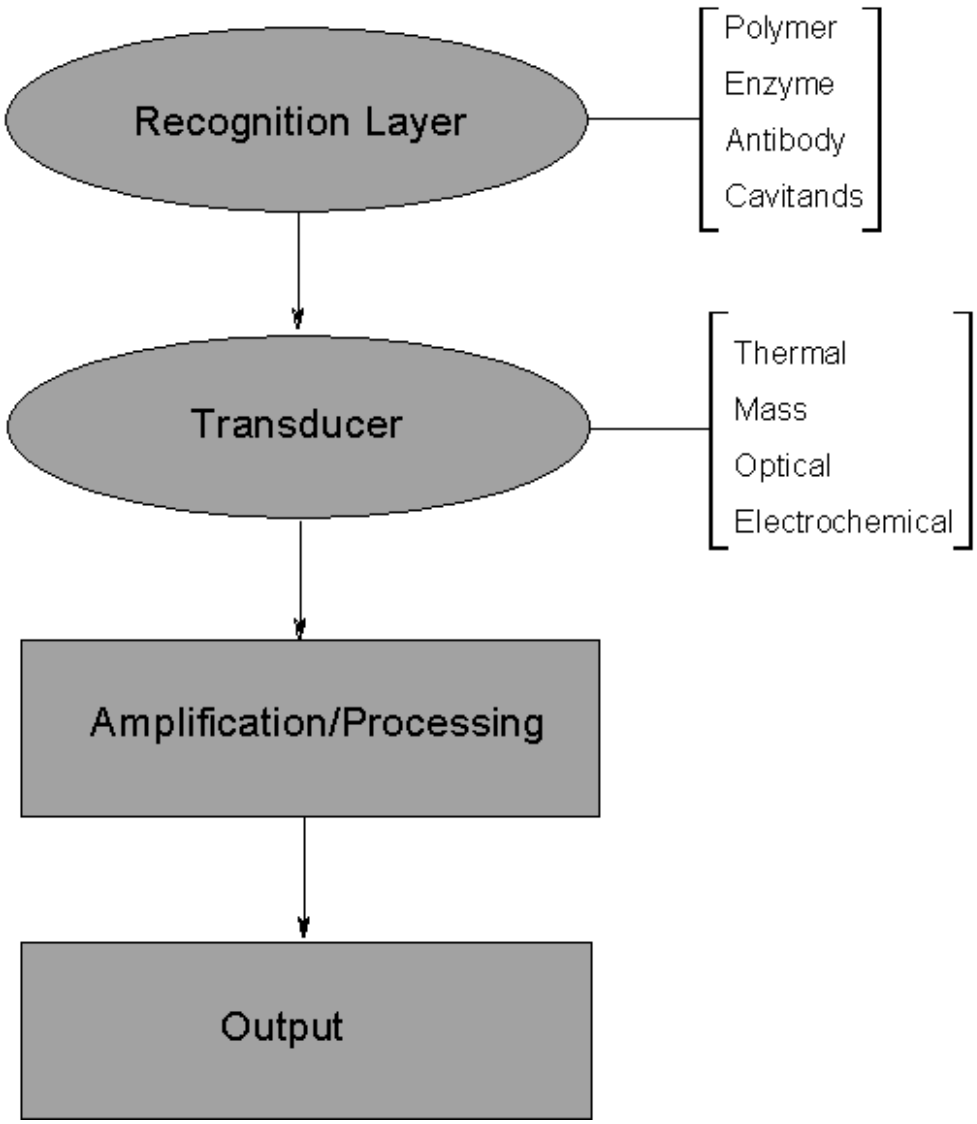

Figure 1.1 Basic components of a chemical sensor.

events is expressed as a signal that may include changes in temperature, mass, light intensity, reflectance, voltage, or impedance. The electronics and software then detect, amplify, and process this signal.

1.3.1 Recognition Layers

As mentioned earlier the key difference between a physical sensor and a chemical sensor is the use of a recognition layer to provide selectivity for the analyte(s) of interest. The selection of the recognition layer is a key element in the design of any chemical sensor. The chemical and biochemical reagents that can be used as recognition layers are nearly unlimited. The recognition layer should ideally be specific for the analyte of interest, but is often just selective for the analyte of interest over other species. Recognition layers used in chemical sensors can be divided into three major subdivisions, ionic recognition, molecular recognition, and biological recognition. Ionic recognition can be done through the use of selective membranes, as with ion selective electrodes (ISEs). Ion exchanging polymers have also been used to detection ions with electrochemical transducers. Molecular recognition can be done through several means, such as chelation and complexation with the analyte, molecular size discrimination, and spectroscopic methods. Biological recognition elements include biologically active elements to employ selectivity such as enzymes, antibodies, nucleic acids, and receptors. The distinctions between these subdivisions can sometimes blur. For example, coulombic forces can be involved in all three areas of recognition.

1.3.2 Transducers

There are many transduction principles that can be applied to chemical sensors. The principal transduction methods can be broken down into four basic types; thermal, electrochemical, optical, and mass transducers[2]. Thermal transducers are devices that are able to convert heat changes into a usable electrical form, usually a resistance change. Thermal transducers include devices such as the thermistor, pellistor and thermal conductivity detectors.

Electrochemical transducers convert chemical signals developed in or at the surface of the recognition layer into potential, current, and conductance values. Electrochemical transducers are broken down into three subdivisions based upon the type of signal produced. Potentiometric transducers measure the potential of a cell at zero current. Voltammetric and amperometric transducers apply a potential to the cell and measure the current, which is related to the analyte concentration. Voltammetric measurements monitor the current through a potential sweep, while amperometric measurements monitor the current in response to a potential step. The third type of electrochemical transducer is conductometric. This method relies on the change in the composition of a solution after a reaction has taken place. The change in solution composition is generally associated with an electrical conductance change of the solution, which is measured.

Optical transducers typically consist of the many spectroscopic techniques developed for chemical analysis, such as absorption, fluorescence, and

scattering techniques. Often optical waveguides are used to transport the light used for these techniques to and from the sensing area to the detector.

Mass transducers generally operate by the use of the piezoelectric effect, where the frequency of an oscillating crystal shifts due to the absorption of material onto its surface[23]. The two most common mass transducers are the quartz crystal microbalance (QCM) and the surface acoustic wave (SAW) device. Table 1.2 shows a list of the transducer technologies describing the output of each and giving specific examples of developed chemical sensors.

1.4 TYPES OF CHEMICAL SENSORS

Chemical sensors are generally subdivided into groups based on the type of transducers that they use. The following sections will look at the fundamentals and examples from these four groups of sensors; thermal, electrochemical, optical, and mass sensors.

1.4.1 Thermal Sensors

A general property of any chemical reaction is the production or removal of heat from the environment. The amount of heat produced or removed is related to the amount of the reactants and thus the measurement of the temperature change produced by a reaction can be related to the amount of a particular component of the reaction taking place. This makes heat an ideal physical parameter to use in sensing systems. There are three major types of

Table 1.2 Major sensor transducer technologies.

Transducer	Output	Examples
Thermal		
Thermistors	Temperature	Enzyme Reactors
Electrochemical		
Amperometric	Applied Current	Polymer Electrodes
Potentiometric	Voltage	Enzyme Electrodes, Field Effect Transistors (FETs)
Conductometric	Impedance	Conductimeters
Optical		
Absorption	Light Intensity or Color	UV-Vis Absorption
Fluorescence Activation	Fluorescence	Scintillation Fibers
Mass		
Piezoelectric Crystals	Frequency Shift	QCM and SAW devices

thermal sensors. The first measures the heat involved in a reaction on the surface of a temperature probe such as a thermistor. The second class of thermal sensors is referred to as catalytic sensors and is used to detect flammable gases. The final class of thermal sensors measures changes in the thermal conductivity of the atmosphere in which it is located when other gases are introduced.

Thermistors

A thermistor is a sensitive device for measuring temperature changes. Its operation is based on changes in the electrical resistance of specific sintered metal oxides (such as BaO, CaO, or transition metal oxides of Co, Ni, and Mn) with temperature. The electrical resistances of these oxides decreases by 4-7% per degree rise in the temperature with an accuracy of ±0.005°C[24, 25]. Typically these devices are constructed as an oxide bead covered with a protective glass coating as shown in Figure 1.2A. Changes in the resistance, and thus the temperature of the device are measured using a Wheatstone bridge circuit. Selectivity is achieved by carrying out a reaction near, or at the surface of the thermistor, which involves only the analyte of interest. Thermistors have been used to measure the small amounts of heat evolved during an enzymatic reaction through use of a microcalorimeter setup shown in Figure 1.2B. In this design an analyte solution flows through a bed of immobilized enzyme and the temperature of the effluent from the enzyme bed is measured and compared to the temperature of a reference thermistor. The reference thermistor measures

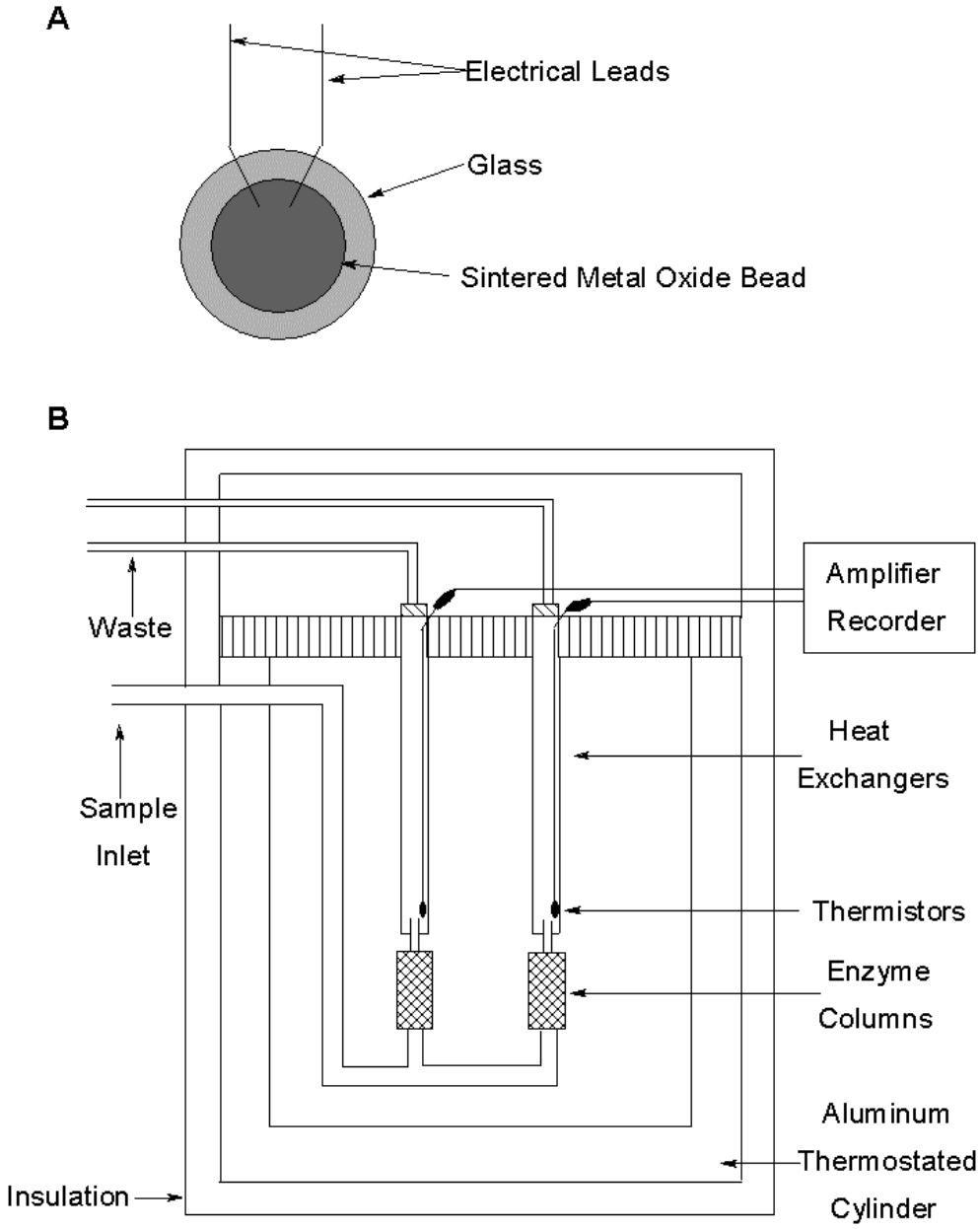

Figure 1.2 A thermistor sensor (A) Typical metal oxide thermistor. (B) Microcalorimeter setup using thermistors to measure heat evolved from an enzymatic reaction[25].

the temperature of the analyte solution after it flows through an identical bed without the immobilized enzyme[26-30]. Miniaturized thermistor based biosensors have also been developed and used[31-34].

Catalytic Gas Sensors

Catalytic gas sensors are a common group of sensors used to detect flammable gases. These sensors operate by measuring the quantity of heat produced during the controlled, catalyzed combustion of a flammable gas in air. The combustion of a flammable gas is generally a very exothermic reaction, making this a very sensitive method. A catalytic gas sensor requires a heater to keep the sensor at a temperature high enough to combust the gas, a catalyst to assist the combustion process, and a device to measure the heat evolved during the combustion. The simplest catalytic gas sensor (for hydrocarbons) can be created with just a platinum wire. The platinum wire is heated by passing a current through it to achieve the combustion temperature, and the combustion of the gas is catalyzed at the surface of the wire. The heat evolved then increases the temperature of the wire and changes it electrical resistance, which is measured. Often a feed-back mode is used to keep the temperature of the wire constant by changing the current applied to it, in this case the current change is measured and related to the temperature change caused by the combustion of this quantity of gas.

More commonly a device known as a pellistor is used as a catalytic sensor. This device retains the platinum wire for heating and temperature

transducer, but uses a more efficient catalyst, typically palladium, for the combustion process that allows lower temperatures to be used[35, 36]. A diagram of a pellistor is shown in Figure 1.3. A particular problem of catalytic sensors is fouling of the catalyst by organosulfur or organophosporous compounds. This can be resolved by making the beads from a porous alumina in which the catalyst is mixed[37]. As with the thermistors, pellistors are usually operated in pairs, one containing the catalyst, and one without it acting as a reference.

Thermal Conductivity Sensors

Unlike the other two types of thermal sensors discussed, this sensor does not involve a chemical reaction taking place at the surface of the sensor. Instead, this sensor uses the differences in the thermal conductivity of different gases. In this sensor a filament is heated to around 250°C. The heat loss from the filament to the surroundings is dependent on the thermal conductivity of the surrounding gas. The thermal conductivities of gases vary dramatically and the temperature of the filament changes with respect to the nature of the surrounding gas and its concentration. The change in the temperature of the filament is detected as a change in the electrical resistance of the wire, just as with the other thermal sensors[38]. Thermal conductivity detectors were one of the first detectors used with gas chromatography (GC) and a typical design is shown in Figure 1.4.

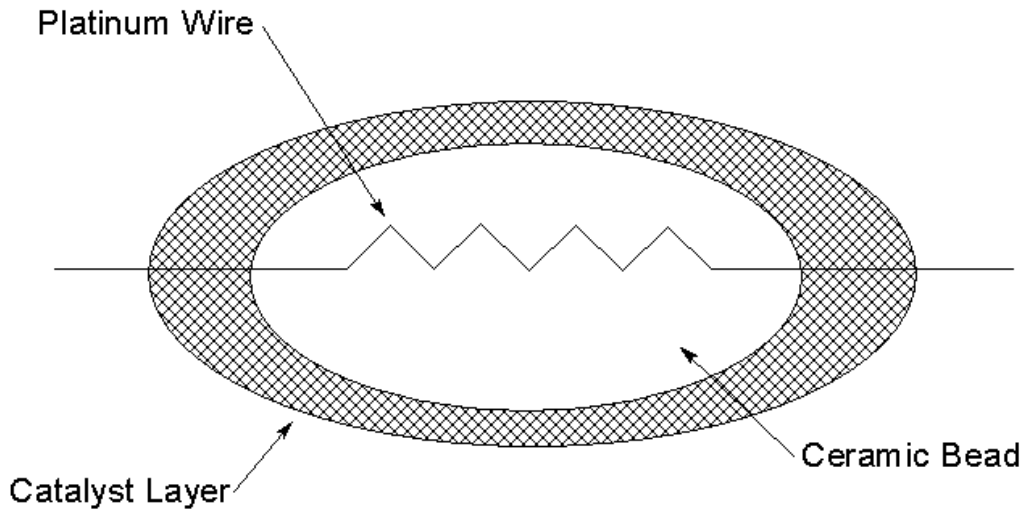

Figure 1.3 A typical pellistor device.

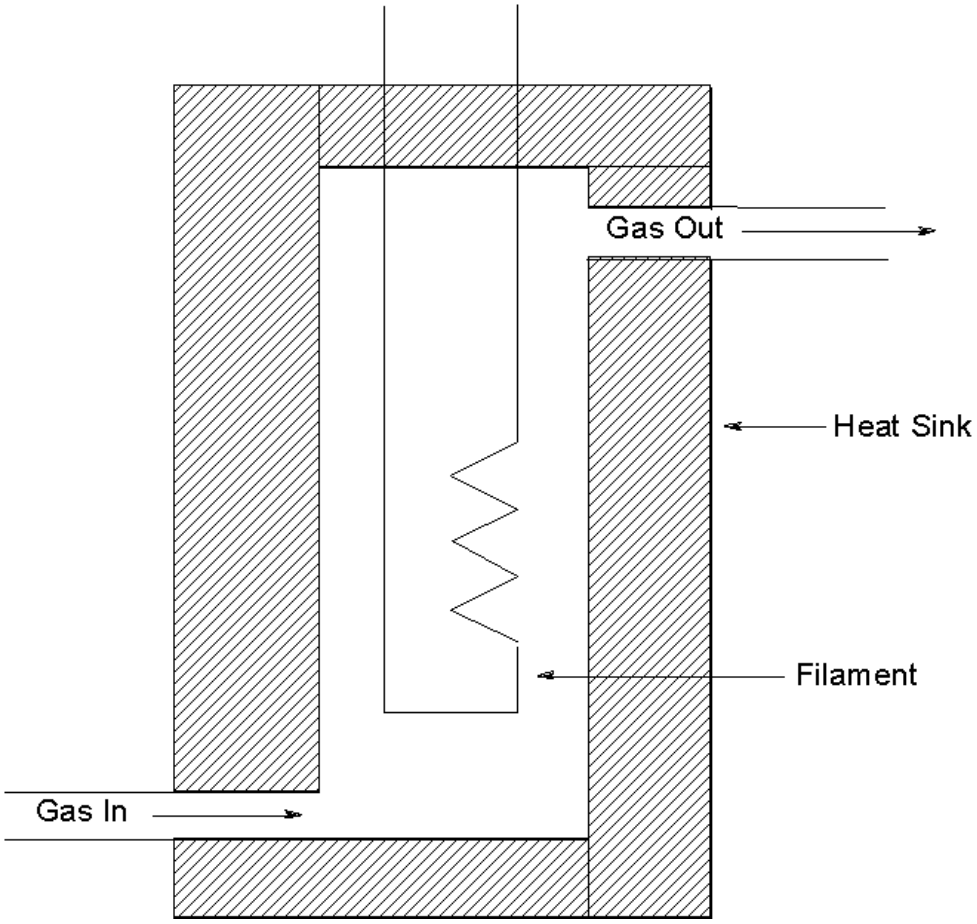

Figure 1.4 A thermal conductivity detector

1.4.2 Electrochemical Sensors

Electrochemical sensors combine the specificity of a chemical or biological recognition layer with an electrochemical transducer, which converts the recognition process into an electrical signal. The electrical signal is related to the recognition process and is proportional to the analyte concentration. Electrochemical sensors fall into one of three categories depending on the nature of the electrical signal produced. These categories are amperometric, potentiometric, and conductometric sensors.

Amperometric Sensors

Amperometric sensors are based upon the detection of an electroactive species involved in the recognition process. The transduction process works by controlling the potential of the working electrode at a fixed value, relative to the reference electrode, and monitoring the current as a function of time. The applied potential serves to drive the electron transfer reaction of the electroactive species and the resulting current is a direct measure of the rate of the electron transfer reaction. This rate reflects the rate of the recognition process and is thus proportional to the concentration of the target analyte[39, 40]. Consider an oxidized species (Ox) and reduced species (Red) of a coupled system shown

$$Ox + ne^{-} \Leftrightarrow Red \qquad E^{0'} \qquad (1.1)$$

where n is the number of electrons transferred. This reaction can be shifted toward the left by applying a potential that is more positive than the formal potential of the reaction ($E^{0'}$) to the working electrode of the system under

standard state conditions. The resulting current from the transfer of electrons at the working electrode can be related to the concentration of the reduced species in the sample by the equation

$$i = nFAD\frac{dC}{dx}\bigg|_{x=0} \qquad (1.2)$$

where i is the Faradaic current, n is the number of electrons transferred, F is the charge corresponding to one mole of electrons, A is the electrode area, D is the diffusion coefficient, which is a characteristic of the analyte, and the derivative term represents the concentration profile at the electrode surface. Similar to amperometric sensors are voltammetric sensors. These sensors also measure the current as a function of the applied potential, however these methods used a potential sweep, rather than a potential step, and a peak is observed in the current near the formal potential of the reaction. The magnitude of the peak is related to the concentration of the analyte[39-41].

Amperometric sensors show some selectivity since the reduction (oxidation) potential is characteristic of the species being analyzed. This selectivity is fairly limited though unless modified electrodes, that incorporate other means of selectivity are used[42]. One of the simplest modified electrodes to prepare is a modified carbon paste electrode. Carbon paste electrodes are prepared by mixing graphite paste with Nujol to form a paste that is placed in an electrode holder as shown in Figure 1.5. These electrodes can be modified by simply adding a selective component, such as a complexing agent, or an electroactive species such as ferrocene in with the paste. Other electrodes can

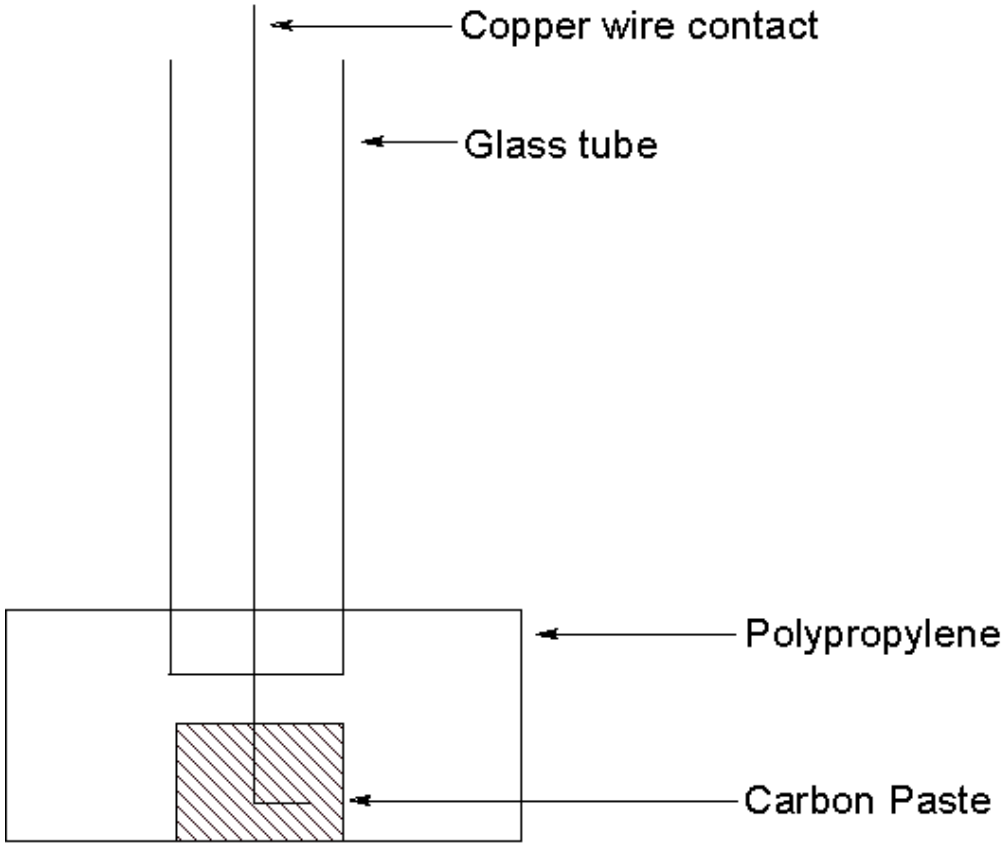

Figure 1.5 Schematic of a carbon paste electrode.

be coated with polymer films to proved selectivity. The polymers used are generally of three types, conducting, ion-exhange, or redox polymers[41].

Potentiometric Sensors

Potentiometric sensors convert the chemical recognition process into a potential signal, which is proportional to the concentration (activity) of the species generated or consumed during the recognition process. This potential is measured under conditions where the current is nearly zero. These sensors are attractive because of their selectivity, simplicity, and low cost. However they are generally less sensitive and slower responding than amperometric sensors[41].

Most potentiometric sensors rely on the use of ion selective electrodes (ISEs) for obtaining an analytical signal. ISEs are generally membrane based devices, consisting of a permselective ion conducting material, which separates the sample solution from the inside of the electrode as shown in figure 1.6. Inside the electrode is an electrolyte solution that contains the ion of interest at a constant activity. The membrane is designed to produce a potential difference that is due to the analyte of interest. Most membranes contain a reagent that selectively binds the target analyte and the interaction between this reagent and the analyte produces a charge separation at the surface of the membrane that is measure as a potential against the reference electrode. When there is a difference in the activity of the analyte of interest in the sample and the activity of the analyte in the electrolyte solution a membrane potential arises. Since the potential of the reference electrode is fixed, the cell potential that is measured

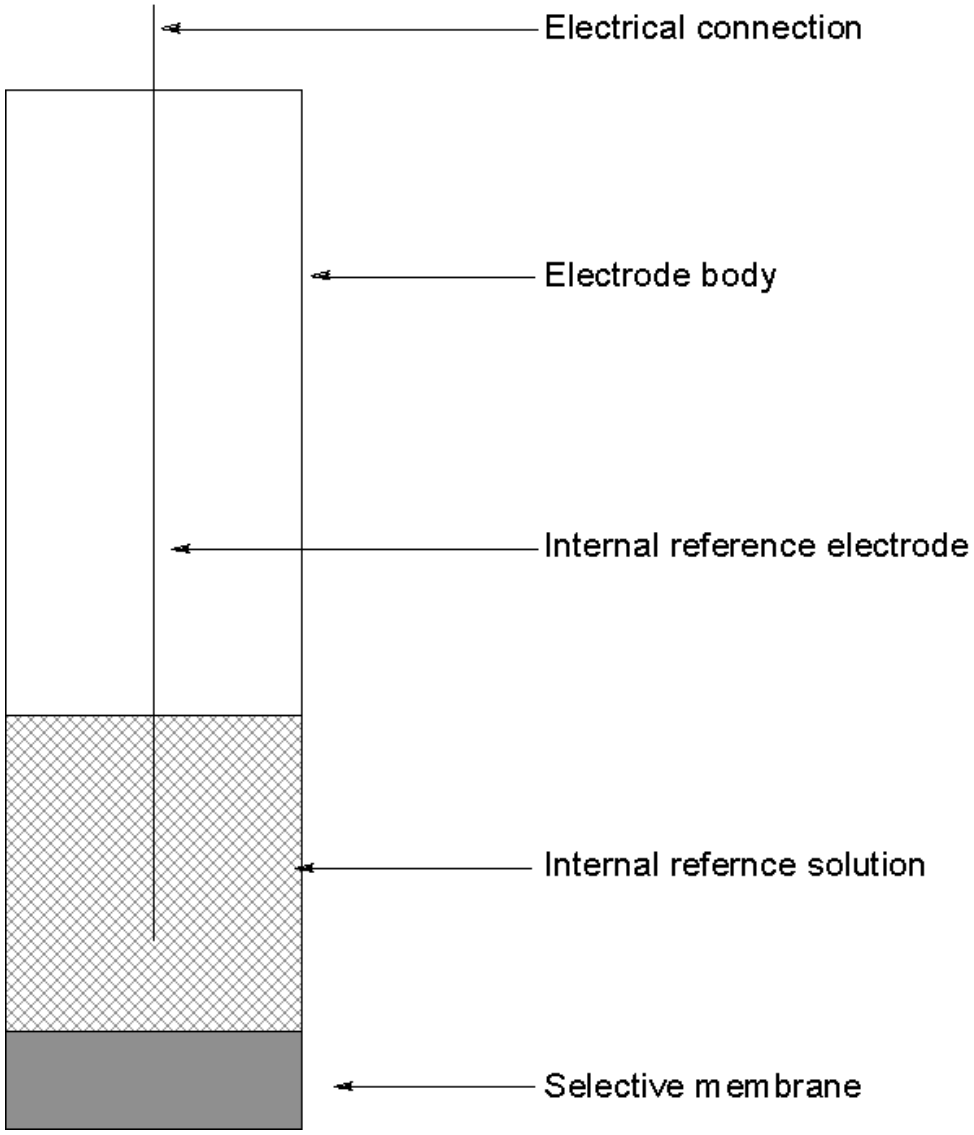

Figure 1.6 Ion-selective electrode geometry for a bench or dip-type electrode.

can be related to the activity of the target analyte. ISEs follow a Nernstian behavior and the potential, E, can be related to the activity of the analyte, a_i, by the equation:

$$E = C + \left(\frac{2.303RT}{nF} \right) \log a_i \qquad (1.3)$$

where C is a constant term that contains the interface potentials in the cell, R is the gas constant, T the temperature in Kelvin, F the Faraday constant, and n the charge on the analyte of interest. The above equation is true except at low analyte concentrations were coexisting ions interfere and a modified form of the equation that considers the activity of interfering ions must be used. ISEs can be divided into categories based upon the nature of the membrane material. These categories include glass membrane electrodes, liquid membrane electrodes, and solid-state membrane electrodes. The pH sensor, a glass membrane electrode is the oldest and best know ISE[3].

ISEs in collaboration with other selective layers have been used to produce many types of chemical sensors. An example is the monitoring of urea, using an ammonium ISE coated with a gel matrix containing the enzyme urease. When urea enters the gel matrix with the enzyme it is broken down into ammonium and bicarbonate ions. An ammonium ISE then detects the liberated ammonium in the reaction layer. This sensor is able to detect urea concentrations from 50 μM to 200 mM[25].

Another type of potentiometric sensors that has come into use is the field-effect transistor (FET). The basic configuration of a FET is known as the

insulated gate FET (IGFET) and is shown in Figure 1.7. It consists of two n-type silicon layers separated by a p-type silicon layer and an insulating layer consisting of silicon dioxide. One of the n-type silicon layers is used as a source and the other as a drain for electrons. The source region is electrically biased with respect to the drain by an small positive applied potential, V_D. The gate is a metal, insulated from the silicon layers, so that it forms a capacitor, a metal/insulator/semiconductor (MIS) arrangement. The gate region is charged with a potential V_G, which is below the threshold potential, V_T for p-type silicon. Above the threshold potential p-type silicon converts to n-type silicon, and inversion occurs. With the gate potential below the threshold potential the silicon remains in the p-type configuration and there is no drain current. When the gate potential is set above the threshold potential, there is a surface inversion and p-type silicon becomes n-type silicon. Now current is able to pass from the drain to the source, without crossing the p-n junction and is proportional to the electrical resistance of the surface inversion, which is controlled by the gate potential, and the drain potential V_D [25, 43]. To convert this configuration into a chemical sensor the metal of the gate is replaced by a chemical recognition layer in contact with a sample solution as shown in Figure 1.8. These devices are generally known as CHEMFETs, with other names given based upon the type of recognition layers used (i.e ion selective FETs, ISFETs and enzyme FETs, ENFETs).

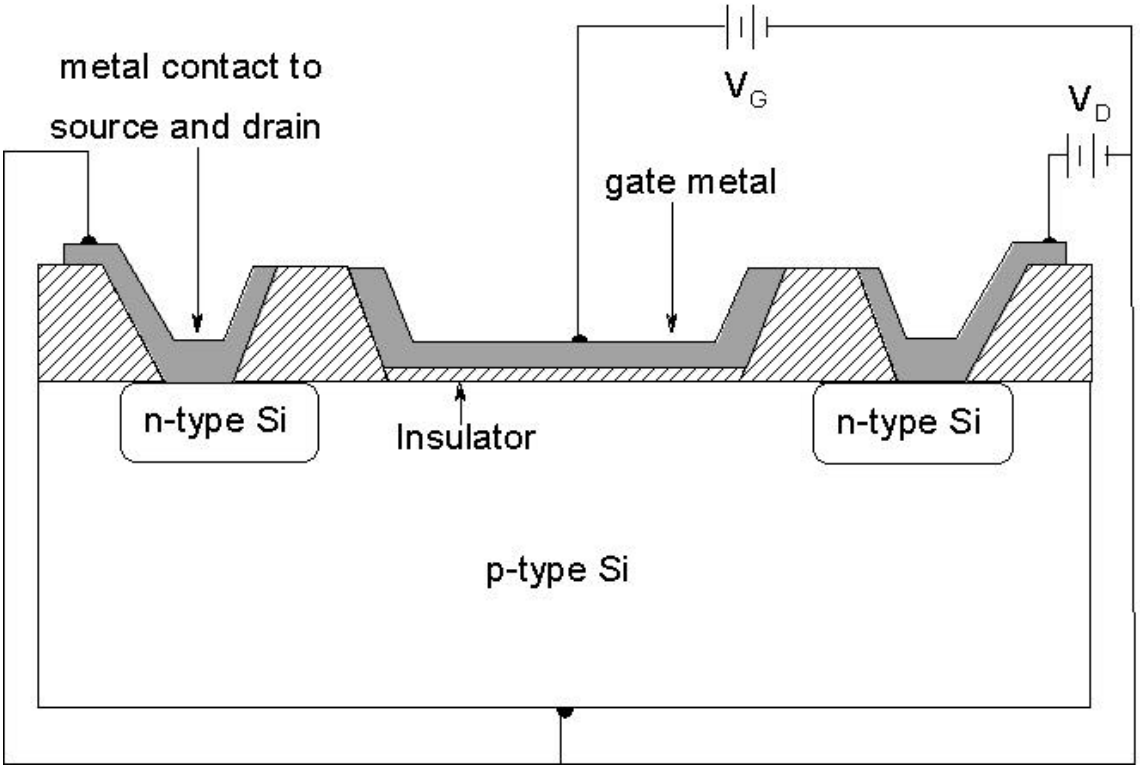

Figure 1.7 Schematic of an insulated gate field-effect transistor (IGFET)[25].

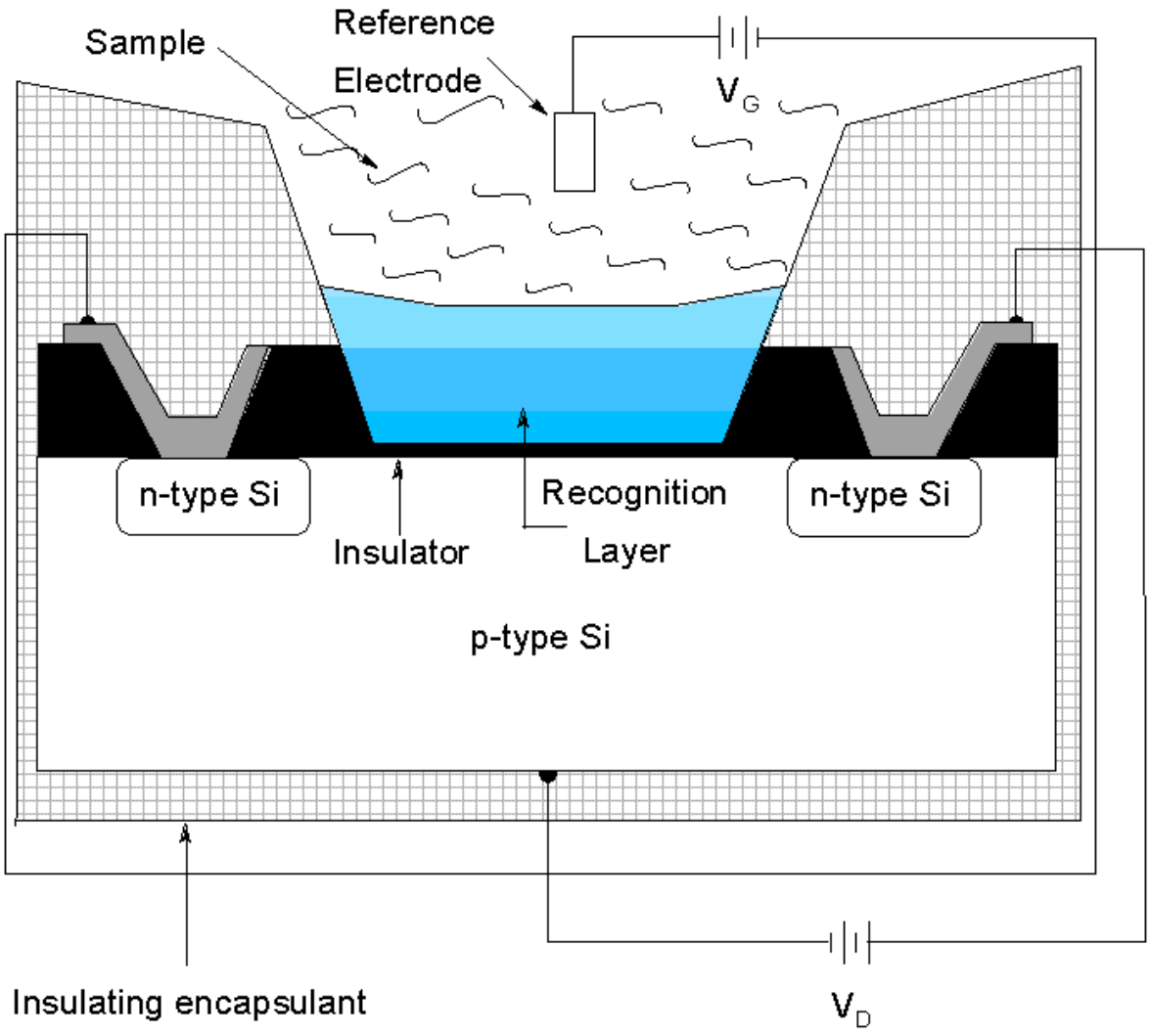

Figure 1.8 Schematic of field-effect transistor with a chemical recognition layer (CHEMFET)[25].

Conductometric Sensors

The third type of electrochemical sensors used, measures the variation of conductance, which is the reciprocal of the sensor resistance. Various types of chemiresistors to measure conductance changes have been described, however these devices generally lack selectivity. The use of arrays of these sensing elements has been the most attractive technique to date. In an array each sensing element can be coated with a different conducting polymer and a unique signature response can be obtained for individual analytes. These signatures can be obtained from mixtures of analytes and have been referred to as electronic noses. With the use of neural network analysis, the evaluation of these devices is possible

1.4.3 Optical Sensors

Optical transduction methods for chemical analysis are well established and sensors based upon these techniques are of great interest. Most optical sensors rely on optical fiber technology to transmit light to and from a sample. The principal components of fiber optic sensors generally consist of a light source, optical fiber(s), a chemical recognition element, and an optical detector. Other elements such as lenses, filters, and spatial filtering devices are usually required to complete the system. Chemical sensing with optical fibers is an attractive technique due to the access to many previously developed optical transduction techniques for chemical analysis, such as fluorescence, absorption, and Raman spectroscopy techniques. The use of fibers, which have very low

light attenuation, also allows for remote in situ monitoring of difficult or hazardous locations, such as groundwater or nuclear tank waste monitoring.

Optical fibers consist of a core, a cladding that surrounds the core, and a jacket that encompasses both these layers. Light is guided through an optical fiber by total internal reflectance at the core-cladding interface as shown in Figure 1.9. Total internal reflection depends on the refractive index of the core material (n_1), the refractive index of the cladding material (n_2), and the angle of incidence of the light wave, q_1 as described by Snell's law

$$n_1 \sin q_1 = n_2 \sin q_2 \qquad (1.4)$$

where q_2 is the angle of the refracted beam to the normal. In the case of an optical fiber the refractive index of the cladding material is lower than the refractive index of the core material ($n_2 < n_1$). At the critical angle for total internal reflection, θ_1 equals θ_c, and the refracted beam θ_2 is equal to 90° to the normal (parallel to the boundary between the core and cladding). For this case Snell's law becomes

$$q_c = \sin^{-1}\left(\frac{n_2}{n_1}\right) \qquad (1.5)$$

and the critical angle can be calculated for any particular interface. At any angle greater than the critical angle, all of the incident light is reflected back into the denser medium, the fiber core in the case of a fiber optic. At angles smaller than the critical angle the light will be refracted into the cladding of the fiber and attenuated before it can escape the fiber[44, 45]. For total internal reflection to actually occur within an optical fiber, there must be no flux of energy into the

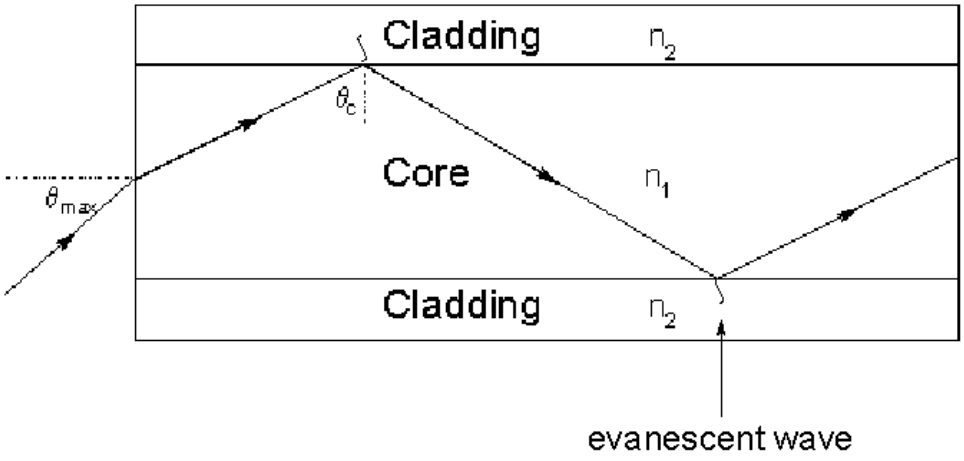

Figure 1.9 Diagram of fiber optic waveguide and conditions to achieve total internal reflection.

lower refractive index material (the cladding). This is not the case with fiber optics as there is a finite decaying electrical field across the interface of the core and cladding that extends into the lower refractive index material. This field is known as the evanescent field. The depth that this field penetrates into the lower refractive index material depends on the wavelength and for visible light is typically between 100 and 200nm[25, 45, 46]. This phenomenon can be used to probe materials near the surface or within the cladding of the optical fiber[47-49].

An important parameter in the design of a fiber optic sensor is the numerical aperture (*NA*) of the fiber to be used. The *NA* is given by

$$NA = n_0 \sin q_{\max} \qquad (1.6)$$

where n_0 is the refractive index of the medium from which the light is entering the fiber, and q_{max} is the maximum launch angle of an incident beam entering the optical fiber. The *NA* describes the light collection efficiencies of a fiber optic sensor, with larger *NA* being preferred[44].

Fiber-optic sensors can be classified into two categories as shown in Figure 1.10[25, 45]. In the first case the fiber acts solely as a lightguide that separates the sensing location from the detector and other monitoring instrumentation. This classification of fiber optic sensors is known as extrinsic sensors (Figure 1.10A). The second classification is known as intrinsic sensors (Figure 1.10B). In these sensors the optical fiber plays an active role as the light transmitted is modulated by chemical interactions at the fiber terminus or along its sides (by employing the evanescent field). Many types of reagents phases

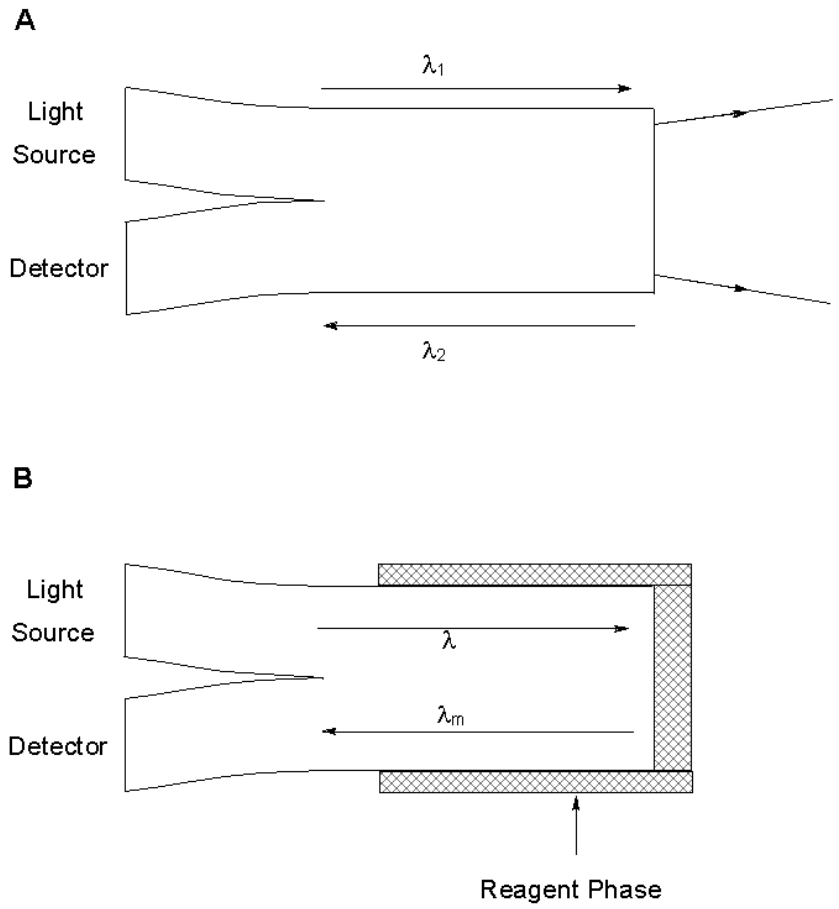

Figure 1.10 Modes of optical fiber use in sensors (A) Extrinsic fiber optic sensors (B) Intrinsic fiber optic sensors.

have been used with fiber optics to create optical sensors, typically the complexation of the analyte with reagents to alter the absorption or to quench or induce fluorescence are often used. Biological agents, such as mono- and polyclonal antibodies have been used with fiber optics for performing competitive binding immunoassays for both biological and chemical analytes[20, 50-52].

A special area of fiber optic sensing that is relevant to our work involves scintillation fibers. Scintillation fibers are used to detect radioactive particles, by converting the energy of the radioactive emission into photons. Similar to a typical fiber optic a scintillation fiber consists of a core that is primarily polystyrene but is doped with an aromatic scintillator that exhibits a good fluorescence quantum yield. When an ionizing particle enters the core of the fiber it loses energy, which excites the electronic energy levels of polystyrene. The polystyrene then relaxes emitting a photon of light[53, 54]. Polystyrene unfortunately has a poor fluorescence yield, which must be enhanced. To enhance the fluorescence yield of the scintillation fiber an aromatic scintillator with a high fluorescence yield is added to the polystyrene. To ensure intermolecular energy transfer between the respective quantum levels of the polystyrene and the scintillator requires that the emission band of polystyrene overlap the absorption bands of the scintillator as shown in Figure 1.11. Another factor that controls the choice of the aromatic scintillator is the emission wavelength. This is important as polystyrene attenuates shorter wavelengths much faster than longer wavelengths, as shown in Figure 1.12. Depending on the emission wavelength of the scintillator, a wavelength shifter

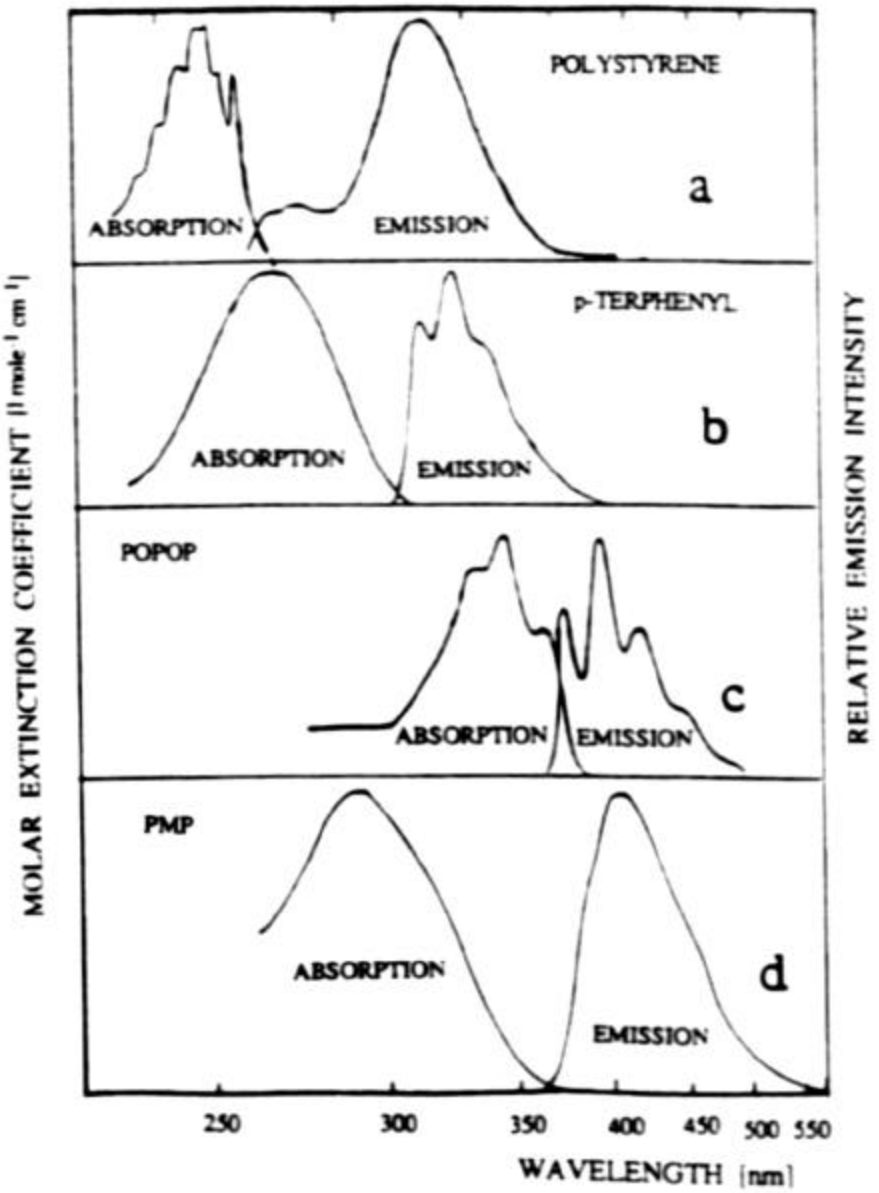

Figure 1.11 Absorption and Emission bands of polystyrene fiber core (a), a p-terphenyl scintillator (b), wavelength shifter 1,4-bis-[2-(5-phenyloxazolyl)]-benzene, POPOP (c), and the scintillator 1-phenyl-3-mesityl-2-pyrazoline, PMP (d)[53].

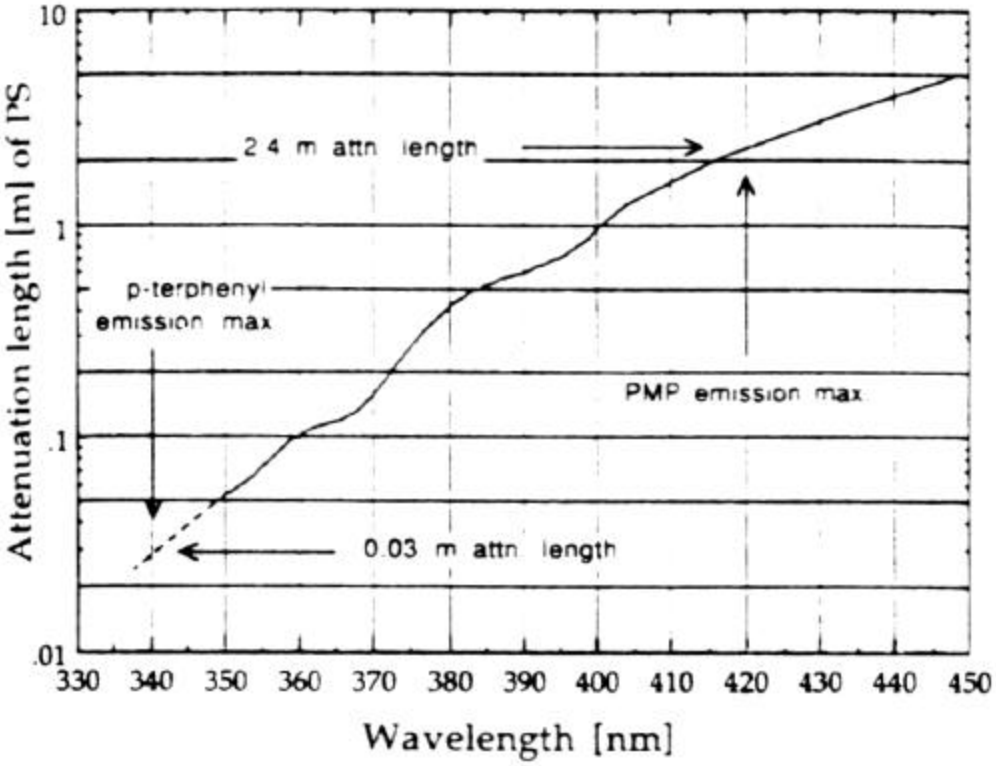

Figure 1.12 Light attenuation of different wavelengths of light through a polystyrene core fiber[53].

may also be added to the polystyrene core to shift the measured photons to longer wavelengths. The wavelength shifter typically absorbs the emission of the aromatic scintillator and then emits light at a longer wavelength that is not as readily absorbed by the polystyrene core[53]. Generally scintillators with large Stokes shifts are preferred to reduce self-absorption of the emission wavelength by the scintillator material. The core is then covered with a coating (typically polymethyl methacrylate, PMMA) with a lower refractive index, than the core to induce total internal reflections. Thus a scintillation fiber combines scintillation properties with the transmission properties of a fiber optic. In contrast to most other fiber optic sensors, scintillation fibers require the use of no light source, as the photons measured are generated within the fiber by the interaction of ionizing particles with the core.

1.4.4 Mass Sensors

Piezoelectric crystals are capable of measuring small mass changes very accurately. By coating these crystals with a chemically selective layer they can be used as chemical sensors. This section will discuss two traditional types of piezoelectric mass sensors, namely bulk acoustic wave (BAW) devices, and surface acoustic wave (SAW) devices. A third type of sensor, based upon the deflections of the microcantilevers used in atomic force microscopy, can be mass sensitive and will also be discussed.

Bulk Acoustic Wave Sensors

When an anisotropic crystal, such as quartz, is mechanically stressed it gives out an electrical signal and conversely when an electrical signal is applied to these crystals they will mechanically deform[23]. With the application of an oscillating electrical potential the crystal will vibrate with a given frequency. The resonance frequency of this vibration is dependent on the crystal and its mass plus any other material coated or absorbed onto it. The absorption of an analyte to the surface of the crystal shifts the resonance frequency, which can be measured with high sensitivity. The relationship between the surface mass change and the change in resonance frequency, Df is defined by the Sauerbrey equation[55]

$$\Delta f = -\frac{1}{r_m k_f} f^2 \frac{\Delta m}{A} \qquad (1.7)$$

where Δm is the mass in grams of the adsorbed material on an area A (cm^2) of the sensing region, f is the overall resonant frequency, r_m is the density of the thin active coating on top of the piezoelectric substrate, and k_f is a frequency constant. For a 5 MHz crystal a resonance frequency shift of 1 Hz, which is easily measured, corresponds to a change in mass of 17 ng/cm^2 [1]. The quartz crystal microbalance (QCM) is the most common type of BAW and a schematic is shown in Figure 1.13 [25, 56, 57].

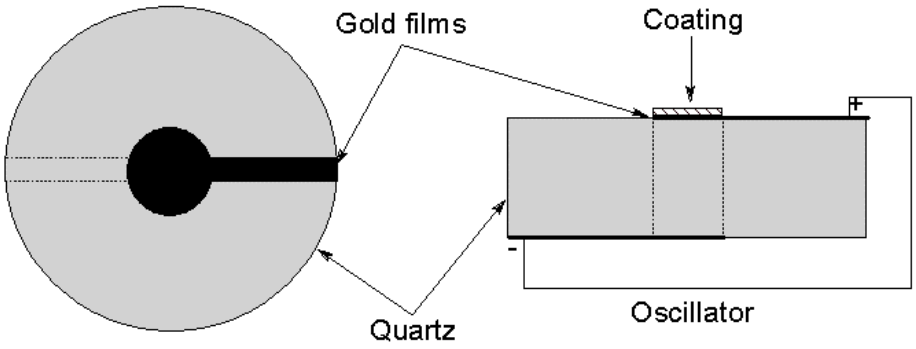

Figure 1.13 Quartz crystal microbalance, an example of a BAW device[1].

Surface Acoustic Wave Sensors

Surface acoustic wave (SAW) devices operate slightly differently from the BAW devices mentioned above. As the name implies, the difference comes from where the resonating waves are generated, the bulk crystal or the crystal surface. In a SAW device a set of interdigitated electrodes, a transmitter and a receiver, are positioned at each end of the crystal. An AC voltage signal is applied to the transmitter set of interdigitated electrodes. The electric field causes the lattice of the piezoelectric material beneath the electrode to distort, causing a surface acoustic wave to propogate toward the other end of the crystal. At the other end another set of interdigitated electrodes, the receiver creates an AC voltage when the surface acoustic wave passes underneath them. Any absorbed material in the path of the wave affects the transmission of the wave, and changes in amplitude, frequency, or phase shift are monitored. A typical SAW device is shown in Figure 1.14[25, 56, 57].

Microcantilever Sensors

Micromachined cantilevers used as probes in atomic force microscopy (AFM) are extremely sensitive to a variety of environmental factors, such as acoustic noise, temperature, humidity, and ambient pressure[58]. Microcantilevers (MCs) are simple mechanical devices. They are small leaf springs with typical dimensions of 0.2-1 μm thick, 20-100 μm wide, and 100-500 μm long, which are attached at one end to a support for handling. A sharp tip on the underside of the leaf spring allows it to be used in AFM for mapping surfaces.

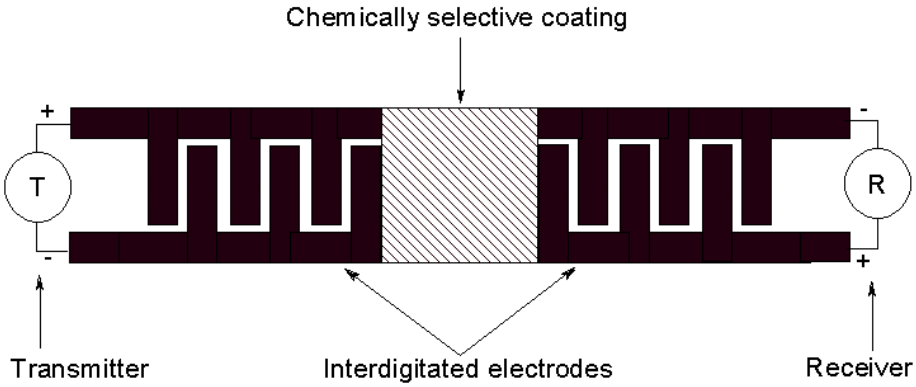

Figure 1.14 Schematic of a typical surface acoustic wave (SAW) device[1].

This sharp tip is not used when a standard AFM MC probe is used as a chemical sensor. MCs are produced using well-established batch processes, involving photolithographic patterning and a combination of surface and bulk micromachining. Figure 1.15 is an image of a one-dimensional array of silicon MCs from a focused ion beam (FIB) mill.

Microcantilever sensors operate by a variety of transduction mechanisms. Depending on the parameter measured, deflection or resonance frequency, the mode of MC operation can be either static, or dynamic. These two modes are each associated with different transduction principles, as shown in Figure 1.16. MCs operating in a dynamic mode are mechanical oscillators, that can be evaluated using simple classical models[10, 59-61].

Generally, the MC oscillations are insignificantly dampened by the medium the MC is contained in, or by chemical coatings on it surface. When an analyte binds to the cantilever surface, the additional mass, Δm, can be related to a shift in the MC resonance frequency, f from its original resonance frequency, f_0 to the new resonance frequency, f_1, by

$$\frac{1}{f_1^2} - \frac{1}{f_0^2} = \frac{\Delta m}{\left(4p^2 K\right)} \qquad (1.8)$$

in which K is the cantilever spring constant. From equation 1.8 it can be seen that high fundamental resonance frequencies are required for typical resonators (SAW or BAW devices) to achieve appreciable mass sensitivity. However MCs with resonance frequencies of 20-200 kHz may have enhanced mass sensitivity when compared with BAW and SAW sensors operating at 5-500 MHz. This

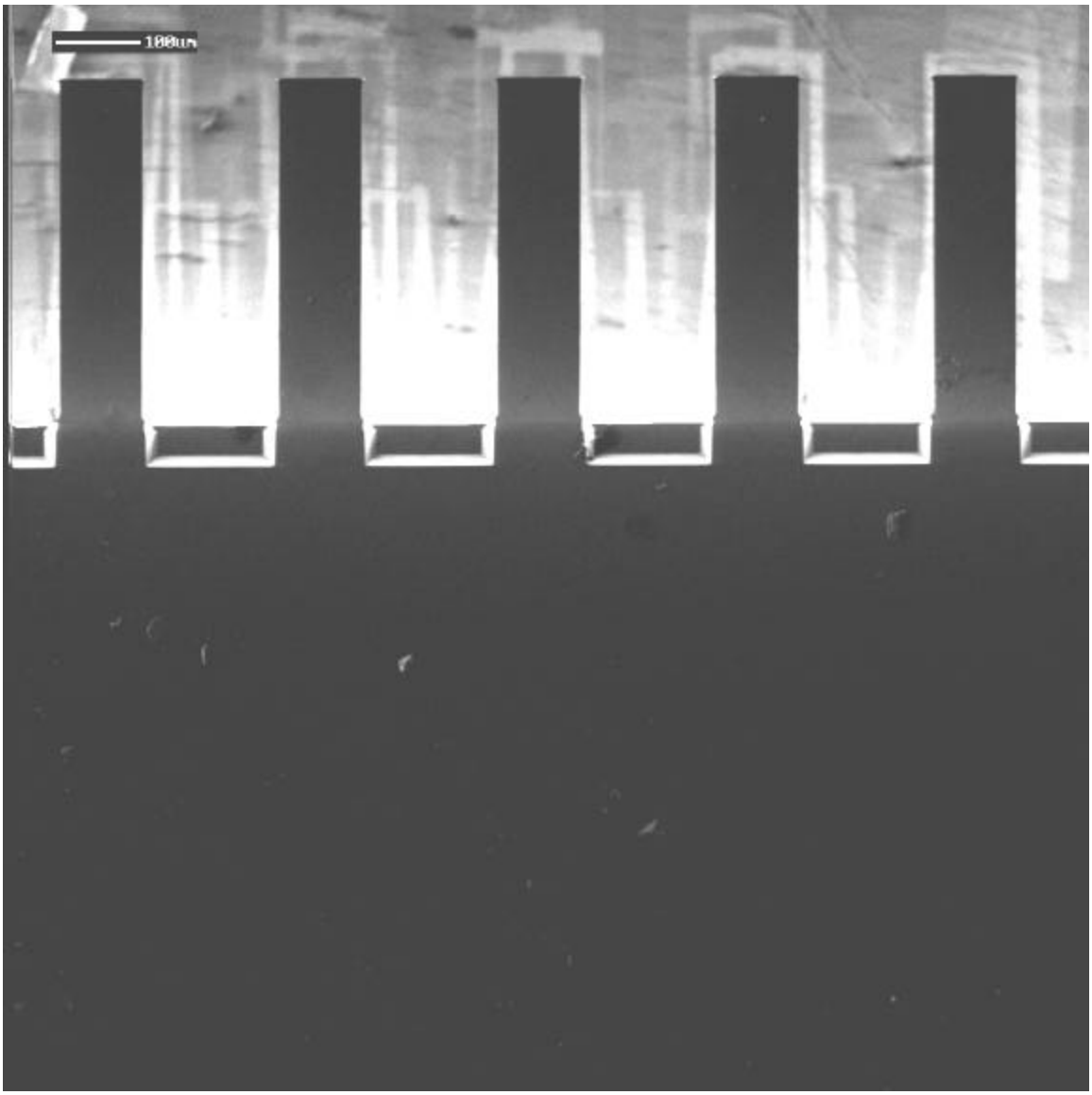

Figure 1.15 Focused Ion Beam image of a one-dimensional array of silicon microcantilevers. Dimensions 100 μm wide, 400 μm long, and 1 μm thick.

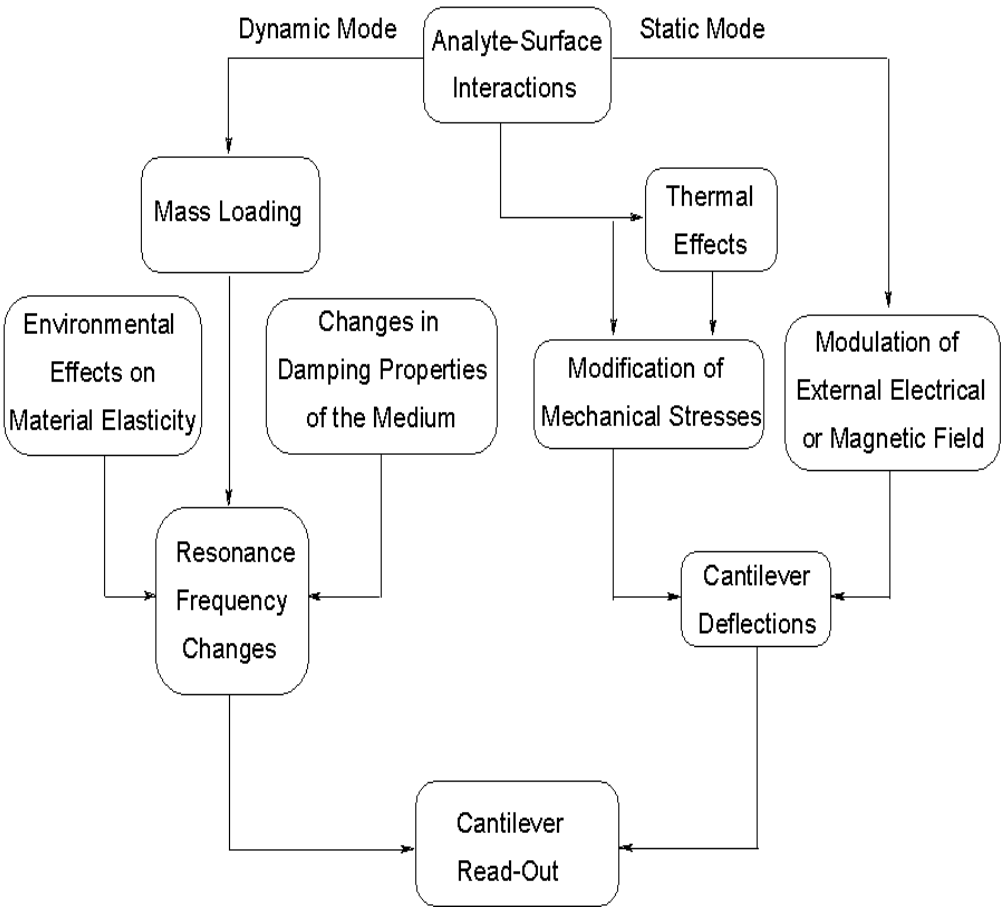

Figure 1.16 Transduction principles that are operative with microcantilever sensors.

sensitivity is due to the relatively low stiffness and minuteness of the suspended mass of a MC structure. In principle, a nanocantilever with an active area of only 1 μm^2 should be capable of detecting the mass associated with a single molecule[62-64]. Nanostructures have been successfully used in studies of very small molecular displacements and molecular level forces[62, 64-66]. The fundamental resonance frequency, f_r,, of a nanocantilever oscillator can be defined using a classical mechanical model[67]

$$f_r = 2p\sqrt{\frac{k}{m_o}} \qquad (1.9)$$

where k is the spring constant and m_o is the effective suspended mass of the cantilever. It is important to recongnize that the resonance frequency f_r may undergo noticeable fluctiations, Δf_r, due to exchange between the mechanical and thermal energy of the cantilever[67].

$$\Delta f_r = \frac{1}{A}\sqrt{\frac{2pK_BTB}{kQ}} \qquad (1.10)$$

where K_B is Boltzmann's constant, T is the absolute temperature, Q is the quality factor of the cantilever oscillator, and B is the measurements bandwidth. Though equation 1.10 predicts increased absolute fluctuations of the resonance frequency, Δf_r, as the resonance frequency, f_r increases, the relative frequency instability $\Delta f_r / f_r$, decreases in the case of higher frequency oscillators

$$\frac{\Delta f_r}{f_r} = \frac{1}{A}\sqrt{\frac{2pK_BTB}{kQf_r}} \qquad (1.11)$$

Combing equations 1.9 and 1.11 the smallest (noise limited) detectable change in the resonator mass can be expressed by

$$\Delta m = \frac{1}{A}\sqrt{\frac{128p^5 kK_B TB}{f_o^5 Q}} \qquad (1.12)$$

As can be concluded from equation 1.12, the major parameters that affect the performance of a mass-sensitive nanomechanical oscillator are stiffness, resonance frequency, amplitude, and quality factor. Assuming a measurement bandwidth of 1 Hz, equation 1.12 predicts single atom mass sensitivity (10^{-23} g) for a nanocantilever with f_r of 10^8 Hz, quality factor of 10^4 and a spring constant of 1 Nm^{-1}.

The static mode of MC responses can be related to mechanical stress generated in the plane of the MC. Thermally induced stresses are typical for metal-coated MCs for which the coefficients of thermal expansion differ for the metal and the base material of the MC. A temperature change in the surrounding medium produces an unequal expansion of the layers in the bimaterial MC, which results in a bending of the structure. This bending translates into femtojoule level sensitivities, and as a result the presence of an analyte may be detected by the heat produced by their adsorption onto the MC, or by the heat produced by a chemical reaction associated with the adsorbate. In this manner MC sensors can also be categorized as thermal sensors.

The adsorption (surface interaction) or absorption (bulk phase interaction with thin films) of an analyte onto a surface induces significant changes in the interfacial stress of the surface. MCs appear suitable for real-time

measurements of surface stress changes in the low milliNewton-per-meter range, which makes them capable of converting changes in the Gibbs free energy created by interactions of an analyte with a binding site on the cantilever surface into a readily measurable mechanical response[68-71]. To use a MC as a chemical sensor one side of the MC is modified so that it has high affinity toward a targeted analyte (active side), while the other side is relatively passive. This allows for a differential surface stress to be developed due to Gibbs free energy changes associated with the adsorption or absorption of analyte onto the active side (equal stress changes on opposing sides would cancel out). The deflection of the MC caused by adsorbate induced surface stress changes can be described by a simple classical relationship derived by Stoney to describe the bending of electroplated metal films on thin plates nearly a century ago[72]. Stoney related changes in the radius of curvature, R, of a plate to the differential surface stress, $\Delta\sigma^{eff}$ by

$$\frac{1}{R} = \frac{6(1-\nu)\Delta s^{eff}}{Et^2} \qquad (1.9)$$

in which, ν is Poisson's ratio, and E is Young's modulus for the substrate, and t is the thickness of the MC. Similarly the deflection of the cantilever tip, z_{max} is releated to the differential surface stress by

$$z_{max} = \frac{3l^2(1-\nu)\Delta s^{eff}}{Et^2} \qquad (1.10)$$

where l is the length of the MC. Equations 1.9 and 1.10 give accurate predictions when adsorbate induced stresses are generated on ideal smooth surfaces or within coatings, that are thin compared to the MC.

MCs systems usually incorporate an optical lever read-out method to measure their responses. In this method a laser beam is reflected from the tip of the MC, and as the MC bends the reflected beam is displaced (Figure 1.17). The displacement of the beam is converted into an electrical signal by projecting the beam onto a position sensitive photodetector (PSD). Deflections (or resonance frequency shifts) in the MC can then be measured and related to an event occurring on its surface.

1.5 STATEMENT OF PROBLEM

A continuing effort in chemical sensor research is aimed at improving both the selectivity and sensitivity of these devices, so that lower limits of detection can be achieved with greater confidence. This body of work focuses on improving both the selectivity and the sensitivity of two different types of chemical sensors described in Chapter 1. Plastic scintillation fibers have been used to detect the decay of radioactive species in solutions, but these sensors lack the selectivity to distinguish particles emitted from different radioactive species. The research presented in Chapter 2 utilizes the ability of plastic scintillation fibers to detect radioactive particles while improving both the selectivity and sensitivity of

this device, through the use of a chemically selective layer. Microcantilever

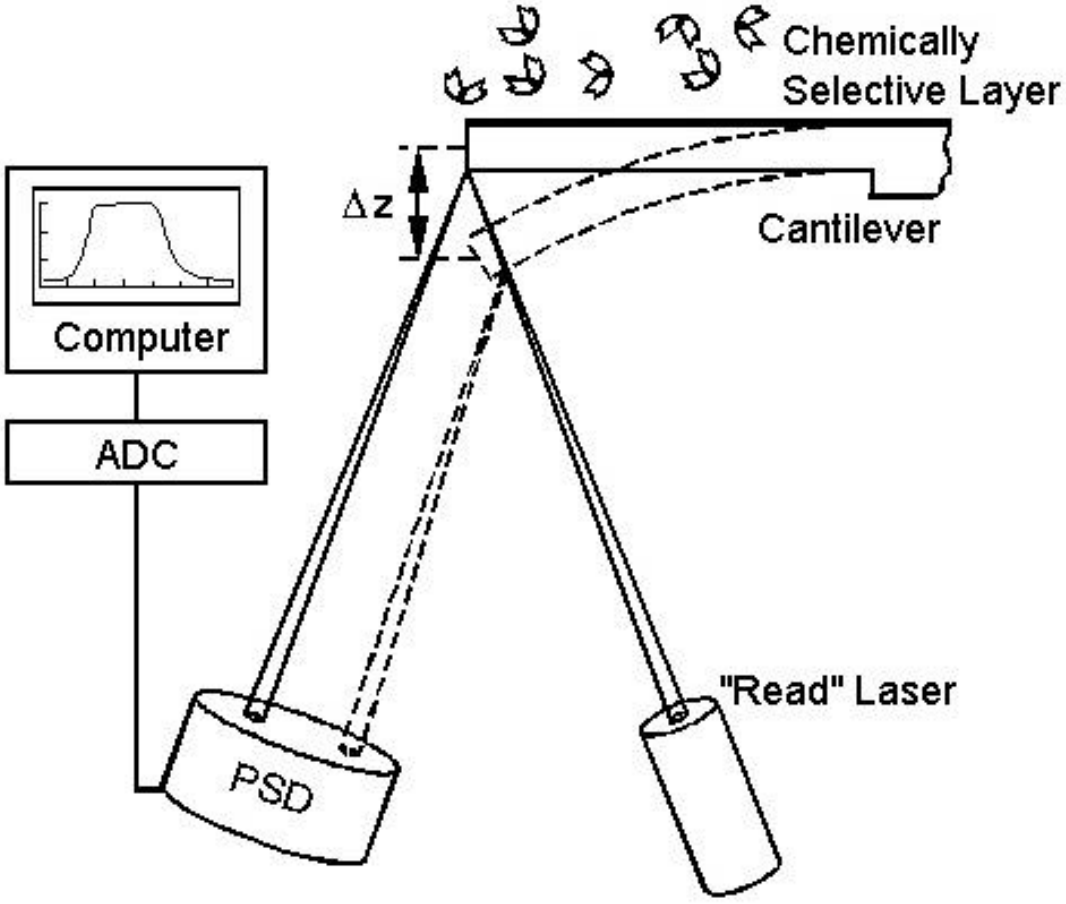

Figure 1.17 Schematic of optical lever read-out arrangement for microcantilever sensing.

sensors are relatively new chemical sensing devices with great potential. Herein methods to improve the sensitivity of these devices through surface modifications are presented.

CHAPTER 2

CHELATING SCINTILLATION FIBERS FOR MEASUREMENTS OF ^{137}Cs

2.1 INTRODUCTION

A major project of the DOE is the safe remediation of high-level radioactive waste that has been stored in underground tanks throughout the United States. There are 271 waste tanks of varying designs, containing more than 93 million gallons of radioactive waste at four sites across the United States[73]. The Hanford Reservation in Washington state contains nearly 2/3 of the high-level waste stored in the United States[74]. Many of these tanks are reaching their expected lifetimes and some are known, or are presumed, to have leaked waste into the surrounding environment[75, 76]. The bulk of the radiation from these waste tanks comes from ^{137}Cs and ^{90}Sr. Respectively, they represent 40% and 25% of the total curie content of these tanks[77]. The tanks were filled with waste from numerous chemical processes and the resultant waste is a complex mixture of various forms (supernatant, salt cake, and sludge)[75]. To properly process this stored waste into stable forms and to remediate the storage sites it is necessary to characterize the contents of the waste within these tanks.

Scintillation counting techniques are among the most useful methods for the detection of a wide assortment of radiation types[54]. The most commonly

used scintillating materials are inorganic alkali halide crystals and organic liquids and plastics. Inorganic scintillators produce better light yields, but exhibit slower response times than organic scintillators. Organic scintillators are generally used for α- and β-particle detection because of their fast response times[54]. The ease with which plastic organic scintillators can be fabricated and shaped makes them extremely useful for scintillation techniques. In β-particle scintillation counters, the kinetic energy from the radiating particle is absorbed by scintillator molecules, which then relax via fluorescence emission of radiation. The resultant photons can be measured by a photomultiplier tube or other phototranducer. Plastic scintillation fibers consist of a core that is primarily polystyrene, doped with an aromatic scintillator that exhibits a good fluorescence quantum yield. The scintillating core is then covered with a PMMA coating that has a lower refractive index than the core to induce total internal reflections, and reduce light losses at fiber surface interfaces[53]. Thus a scintillating fiber combines scintillation properties with the light transmission characteristics of a fiber optic.

Dual mechanism bifunctional polymers (DMBPs) consist of two distinct functional groups on a given supporting network, each of which functions by a different complexing mechanism. One mechanism is typically aspecific and serves to rapidly bring the species of interest into the polymer matrix, making it easily accessible to a highly specific recognition mechanism. Ion exchange is typically the access mechanism to bring metal ions into the polymer and into range of the highly specific recognition site[78, 79]. The recognition site functions to selectively retain the analyte of interest within the polymer. DMBPs

are divided into three classes based upon the recognition mechanism. Class I DMBPs consist of ion exchange/redox resins, Class II consists of ion exchange/coordination resins, and Class III are ion exchange/precipitation resins[79].

The study presented in chapter 2 utilizes commercially available scintillation fibers that have been coated with a Class II DMBP for the detection of ^{137}Cs in aqueous samples and in tank waste simulants. Specifically, the DMBP is composed of phenol-formaldehyde oligomers grafted onto a polystyrene based resin bearing diphosphonate ligands (Figure 2.1). The DMPB has been shown to be selective for Cs (I) in the presence of Na (I) with distribution coefficients greater than 400 ml/g[78]. Further selectivity studies have been performed in this work to evaluate possible interfering species of the DMBP that are common within sample matrices that contain ^{137}Cs. These fibers are similar to solid phase micro-extraction (SPME) fibers, as they are able to combine sampling, extraction, concentration, and sample introduction techniques into a solitary step. Unlike procedures using SPME fibers, which consist of two processes, the partitioning of the analyte between the coating and sample and the desorption of the analyte into an analytical instrument, there is no need of a desorption step for these chelating, scintillation fibers[80]. However, the desorption step can be performed to regenerate the fiber. The instrumental and procedural simplicity of this approach should facilitate field measurements.

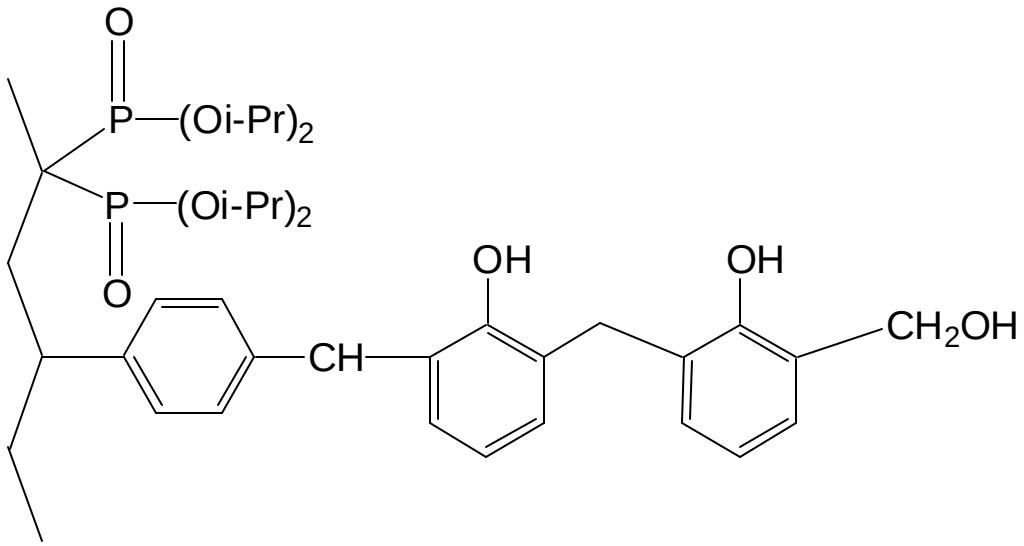

Figure 2.1 Cesium Selective Dual Mechanism Bifunctional Polymer (DMBP).

2.2 EXPERIMENTAL SECTION

2.2.1 Instrumentation

Experiments were performed using an EG&G ORTEC (Oak Ridge, TN) photon counting system. The system consisted of a series bin and power supply (series 401/2), a high voltage power supply (model 456) with an output range of 10 to 3000 V, a photon counter (model 9315), an amplifier discriminator (model 9302) with a gain setting of 20 or 200 for the amplifier and a 0.050 to 1 V threshold range for the discriminator. A RCA IP28 (U.S.A) or Hamamatsu R928 (Iwata-Gun, Japan) photomultiplier tube was used to collect impeding photons in a Pacific PMT housing (model 3377D) cooled with dry ice. Counting times for all experiments was 100 seconds and data presented is typically the average of 10 count cycles.

Scintillating fibers were positioned by the use of a machined Delcron piece that was threaded to fit into the PMT housing. A hole was drilled through the center of the Delcron piece that extended back to contact the window in front of the photocathode. This allowed the fiber to be positioned as close to the photocathode as possible and assured that the same area of the photocathode was impeded with photons from each scintillation fiber used in these studies. In this arrangement, no optics external to the fiber are needed to efficiently couple scintillation photons onto the PMT photocathode.

2.2.2 Cs Selective DMBP

The phenol-formaldehyde grafted polystyrene based resin was prepared by a suspension polymerization of tetraisopropyl 1,1-vinylidenediphosphonate, vinylbenzyl chloride and acrylonitrile in a 1:1.35:2.25 mole ratio[78]. The resin contained 5% divinylbenzene as a crosslinking agent. The benzyl chloride moiety on the resin was then converted to a benzaldehyde moiety by a reaction with excess dimethyl sulfoxide and sodium bicarbonate at reflux for 8 h. The aldehyde site serves as the attachment point for the phenol-formaldehyde chains, which were grafted onto the resins[78]. The resin beads had diameters in the range of 75-150 μm.

To reduce attenuation of β-emission by the beads and to produce a stable resin bed, the beads were ground to a smaller size using a ball mill filled with ceramic beads. A large volume of the resin beads in water was placed in the ball mill and ground for 24 hours. The diameter of the collected resin particles were then measured using a technique known as fineness of grind. This technique uses two calibrated plates to measure the particle diameter. One plate is spotted with the particles and the other is pulled across it smearing the sample across the first plate. The plates are designed so that as they are pulled across each other the gap between them decreases. At the point where the particle size and the gap are equal the particles are dragged across the surface leaving streaked lines on the plate. The size of the particles can then be read from the calibrated plate. Using this technique the particles were determined to have diameters of 3-5 μm. The particles were then dried in an oven.

2.2.3 Materials and Chemicals

The scintillating fibers BCF-12 were obtained from Bicron, (OH). The dimensions of the scintillating fibers were 1 mm diameter x 1.5 m as received from the supplier. They were cut to desired working lengths by hand. Radioactive ^{137}C was donated by Professor Larry Miller of the UTK Nuclear Engineering Department and had an activity of 80 μCi in 20 ml of solution. Chemicals used in preparing the double shell slurry feed (DSSF) Hanford were KOH, NaOH, NaCl from Mallinckrodt (St. Louis, MO); Na_2SO_4, Na_2CO_3, $NaNO_2$, and $Ca(NO_3)_2 \cdot 4H_2O$ from Fisher (Fairlawn, NJ); $Na_2HPO_4 \cdot 7H_2O$, $Al(NO_3)_3 \cdot 9H_2O$, and NaF from Aldrich (Milwaukee, WI); $Ba(NO_3)_2$ from Allied Chemical & Dye Corporation (New York, NY); and $Sr(NO_3)_2$ from J.T. Baker Chemical Company (Phillipsburg, NJ). A sulfonic acid functionalized ion exchange resin, Amberlite IRP-69 was obtained from Aldrich (Milwaukee, WI). The ion exchange resin had a wet mesh size of 100-500 and an exchange capacity of 4.3 meq/g. The resin particles were ground down using a ball mill to match the particle size of the Cs selective DMBP.

2.2.4 Coating of Scintillation Fibers

Plastic scintillation fibers were cut to the desired working length, washed with ethanol to remove any oils and dirt, and then air-dried. Five-minute Epoxy from *ITW*Devcron (Danvers, MA) was diluted to a desired % epoxy solution (1-10% w/w) with acetone. The thickness of the epoxy coatings was measured

using a DekTak 8000 profilometer manufactured by Veeco (Santa Barbara, CA). The clean scintillation fibers were dipped into the epoxy solution and then placed into a bed of particles. After removal from the particle bed the fibers were shaken to remove any loose particles. The epoxy was then allowed to cure overnight. Upon curing of the epoxy the fibers were rinsed in deionized water to remove any loose particles and air-dried. Finally the tips of the fibers were snipped off to eliminate an area of thicker coating that developed as the fibers were pulled from the epoxy solution.

2.3 RESULTS AND DISCUSSION

2.3.1 Signal Considerations

The radioactive decay of ^{137}Cs can proceed by the two processes shown below:

$$^{137}Cs \rightarrow ^{137m}Ba + b^{-}(0.512Mev);\ ^{137m}Ba \rightarrow ^{137}Ba + g \qquad (2.1)$$

$$^{137}Cs \rightarrow ^{137}Ba + b^{-}(1.17Mev) \qquad (2.2)$$

These processes produce βs with maximum energies of 0.512 and 1.17 Mev respectively[81]. The weighted average energy is 0.171 Mev. Using a relationship provided by Glendenin the penetration depth for this average energy is 35 mg/cm^2[82]. In a density of 1000 mg/cm^3 this corresponds to a depth of 350 μm.

The signal in counts/second (Sig-cts) depends on the number of? β-particles that are launched into the fiber/second that have sufficient residual

energy to produce a photon burst which registers above the threshold level set on the amplifier/discriminator. The scintillator material used in these studies is reported to have a photon conversion efficiency of 8 photons/Kev[83]. The fraction of β-generated photons that result in photon pulses at the PMT (F_t) is approximated by

$$F_t = f_{ir} \times f_{opt/pmt} \qquad (2.3)$$

where f_{ir} is the fraction that are internally reflected toward the PMT and $f_{opt/pmt}$ is the product of the fraction transmitted by the optical components in the system (fiber, PMT window) and the quantum efficiency of the PMT; values are estimated to be 0.04 (based on a numerical aperture = 0.58) and 0.05, respectively. This produces a F_t of 0.002. If the discriminator level is set to the equivalent of 2 photons (a value that should adequately reject thermal PMT photocathode pulses) then the residual β-particle energy must be greater than approximately 125 Kev in order to register a count (i.e., energy (Kev) = 2 photons / (8photons/Kev x F_t))

The number of β-particles that satisfy these criteria and produce a detectable signal depends on the absolute activity of the source (A_{abs}) in Ci and the fraction emitted in the proper direction; i.e. a direction that will place the β-particle in the fiber core with an energy exceeding 125 Kev (see Equation 2.4).

$$Sig-cts(cts/s) = A_{abs} \times 3.7e^{10}(diss/s)/Ci \times f_{dir} \qquad (2.4)$$

Figure 2.2A is a geometric depiction of a cross section of the fiber showing the core (1,000 μm dia.), optical cladding (~3 μm), epoxy (~1 μm), Cs-specific

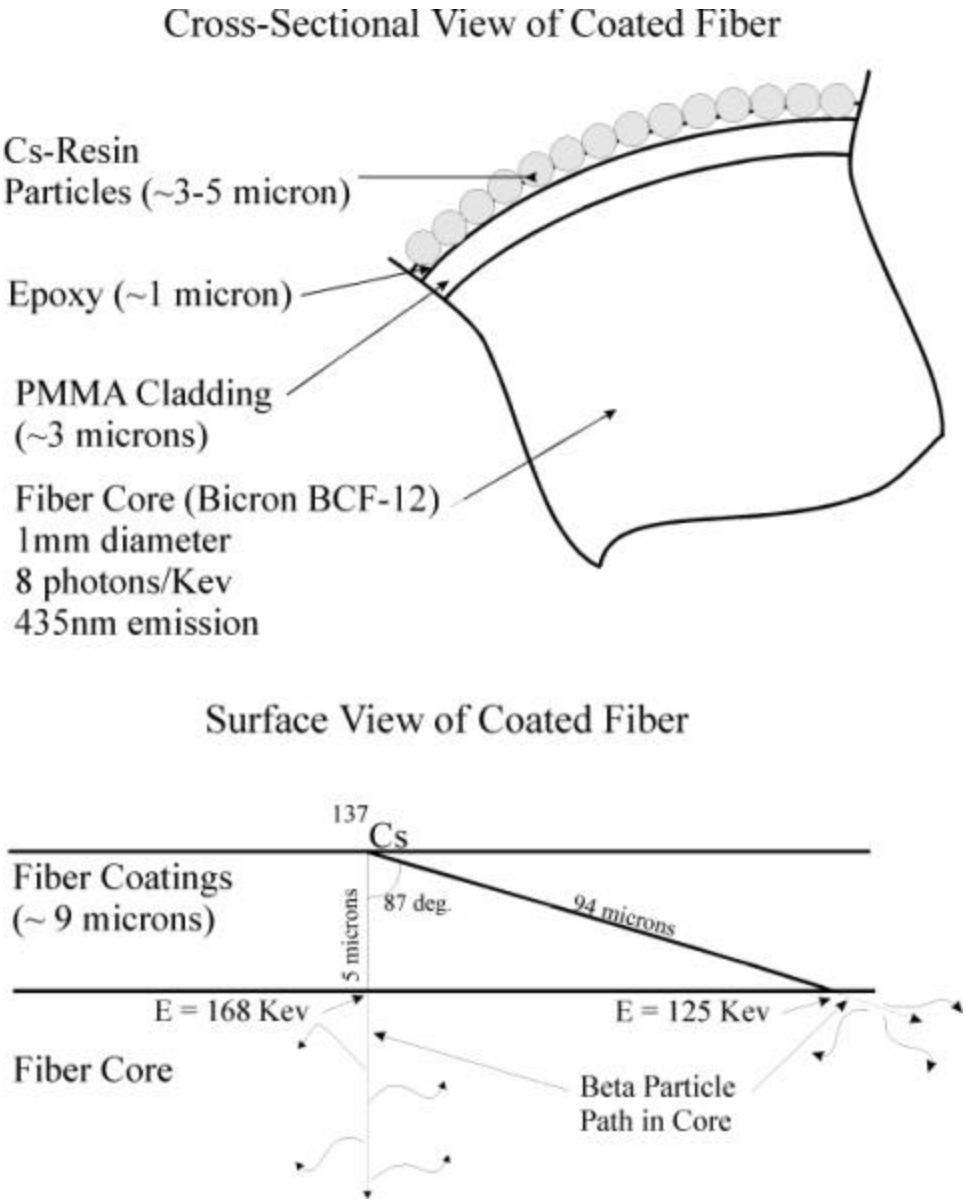

Figure 2.2 Cross sectional views of a coated scintillation fiber (A) and surface view of coated fiber showing factors affecting conversion of β-particle energy to photons in the fiber core (B).

resin particles (~3-5 μm dia.) and surrounding sample solution. Figure 2.2B is a two dimensional graph showing the process of β-emission from a ^{137}Cs located at a distance of 5 μm from the fiber core. β-particles which are emitted with the weighted average energy (171 Kev) and at an angle as depicted that is less than 87° should reach the core with sufficient energy (125 Kev) to be counted. This assumes a linear loss in energy as the emitted β-particle travels through cladding, epoxy, or resin all having a density assumed to be close to 1,000 mg/cm^3. The solid angle of collection is nearly 180° so f_{dir} is assumed to be 0.5.

In most of the measurements the resin coated fiber is allowed to come to equilibrium with a volume of sample. The fiber is removed and signal is registered while the fiber is dry (see Experimental Section). Knowing the mass of resin on the fiber, the activity and volume of the sample solution, and the distribution coefficient (D) one can compute the activity of ^{137}Cs bound to the resin. For example, most measurements were performed using a 0.35 cm^3 sample volume (V) and 3.0×10^{-4} g of resin (M). The mass of resin on the fiber was estimated by calculating the volume of the resin on the fiber and assuming a density of 1 g/cm^3 for the resin particles. The resin volume was calculated by determining the difference in volume between an uncoated fiber and a fiber coated with 5μm resin particles. The value of D is approximately 490 cm^3/g (see below). Using the following relationship

$$\frac{DM}{V} = \frac{A_R}{A_{S,0} - A_R} \qquad (2.5)$$

where A_R is the activity of resin bound ^{137}Cs (used as A_{abs} Eq. 2.4) and $A_{S,0}$ is the initial activity of ^{137}Cs in the sample solution before uptake by the resin. Using Equations 2.4 and 2.5, a count rate of 7 cts/s is calculated for the most dilute ^{137}Cs solution used in these studies (1.4 nCi in 350 μL). The observed count rate was approximately 5 cts/s for this solution, which is reasonably comparable considering the assumptions made in this theoretical treatment.

The photon counting system used in this work was not ideally suited to these experiments. In particular, while the discriminator level was readily adjusted within its limits, it was not possible to read out the actual discriminator setting. Thus optimization studies could only be performed crudely. In these studies it was observed that signal to noise levels were best when there was an appreciable background (~10^2 counts per 100 second count period). Presumably this is a result of the wide range of β-particle energies from ^{137}Cs emission. Although different discriminator levels were employed in these studies, a single setting is used whenever comparisons are made (e.g., in obtaining the calibration plots presented below). Another limitation of the system is the crude mode of cooling the PMT. Temperatures for the PMT probably varied slightly over long experiments or from day to day. The PMT also needed to be changed during the course of the studies due to failure of the one initially employed. It should be mentioned that the scintillation fibers are very well suited to coinicidence counting methods using the outputs from opposite ends of the fiber and the proper instrumentation. By using such instrumentation and longer fibers with greater accessible resins amounts (M in Equation 2.5), limits of detection (LOD) lower

than reported herein should be possible.

2.3.2 Coating Thickness Studies

The thickness of the coating applied to the scintillation fibers is of concern to prevent attenuation of β particles from the radioactive decay of ^{137}Cs. Attenuation of β particles before they reach the core of the scintillating fiber would increase the LOD achievable with the fibers. To study the effect of coating thickness upon signal counts, coated fibers were produced using varying percent epoxy solutions. A plot of counts above background versus the percent epoxy used for each fiber is shown in Figure 2.3. From this plot it can be seen that there is a steep drop in signal counts, when as little as a 1% epoxy solution is applied to the fibers. This suggests that as small a percentage of epoxy as possible should be used to prevent signal attenuation. Less occlusion of the resin is also expected for thin film epoxy coatings. Unfortunately, coatings made from epoxy solutions below 1% were not physically stable. This lack of stability caused irreproducibility between measurements when the same fibers were regenerated by an acid rinse and reused. The signal loss from fibers coated with epoxy solutions above 1% is relatively constant. The reason for this is not clear. Coatings that employed a percent epoxy solution of about 3% were also seen to be stable, allowing better reproducibility between measurements, made with the same fibers. Profilometry measurements were used to determine the thickness of the epoxy coatings. Fibers were dipped in an epoxy solution so that there were two sections of the fiber, coated and uncoated. The fibers were coated with

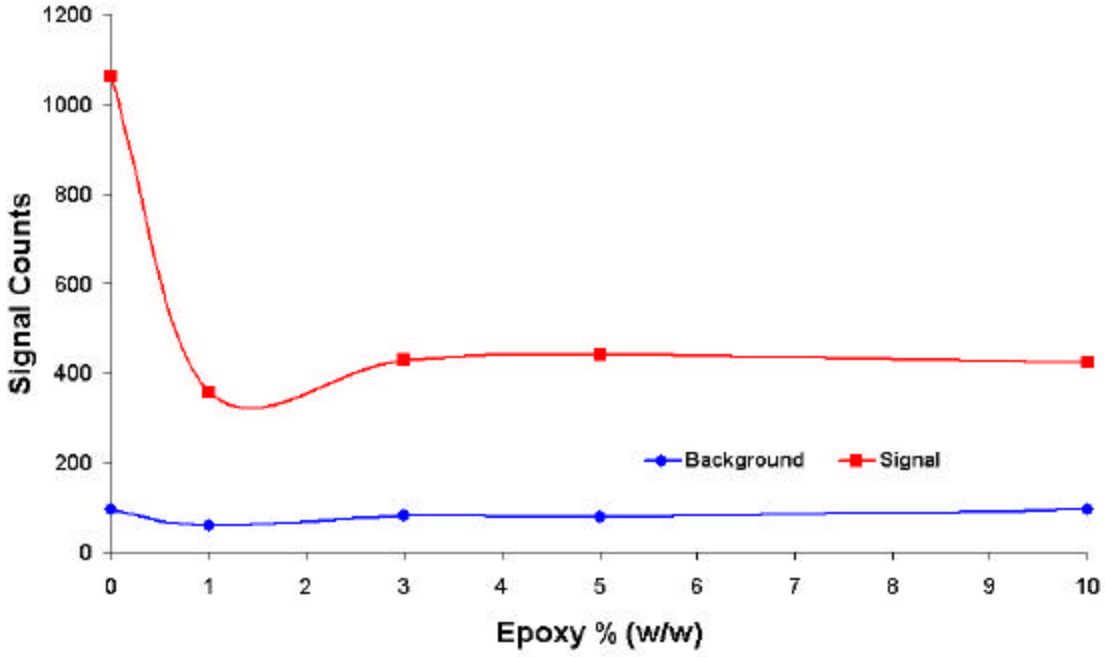

Figure 2.3 Signal and background versus percent epoxy and particles coating the fiber.

3% and 10% epoxy solutions. Measurements of these two coatings showed virtually no difference in thickness, with each fiber exhibiting a step height of ~1 μm from an uncoated section of fiber to the coated section. This is consistent with the signal data plot in Figure 2.3.

2.3.3 Reproducibility

The reproducibility of the chelating, scintillating fibers was studied by coating seven fibers with the DMBP using a 3% epoxy solution. Each of these fibers was then used to measure the signal from a 400 nCi/ml solution of ^{137}Cs. The %RSD for the seven fibers was 11.0%. This RSD represents not only the reproducibility in the coating of the fibers, but also positioning of the fiber within the PMT housing. This relatively low RSD value indicates that the fiber coating procedure used produces consistent resin coatings. However, it is possible to regenerate fibers. The fibers are regenerated by rinsing in 1M HCl for 10 minutes to remove ^{137}Cs from the DMBP. The fibers are then rinsed with water for 10 minutes and dried. To assure that ^{137}Cs was removed, the signal from a regenerated fiber is compared to the signal from an unused fiber. If the background signal measured with the regenerated fiber is within a standard deviation of the background measured with an unused fiber then the regeneration is considered complete; if not, the rinsing procedure is repeated. In some cases, particularly with repetitive regeneration, it was visually observable that this process resulted in the loss of resin from the fiber. It is believed that the loss of the resin is caused by degradation of the epoxy used to secure the resin

to the fiber surface during rinsing with HCl.

The loss of resin from the fiber makes it difficult to use one fiber for a set of experiments and still achieve a linear response. We did not conduct studies to find more reliable rinsing procedures. While it is desirable to be able to regenerate the fibers to reduce experimental costs and deviations between fibers, the inability to do so reliably is not detrimental to their use because the fibers are inexpensive to produce and it has been shown that the reproducibility from fiber to fiber is sufficient for many applications. For these reasons most experiments reported herein were performed using new fibers for each sample solution.

2.3.4 Fiber Uptake Kinetics; With and Without Potential Interferences

The rate of uptake of ^{137}Cs into the polymer matrix was studied to determine an appropriate equilibration time for the fibers in solution. A factor of the rate of uptake of ^{137}Cs into the polymer is the ion exchange process. This process may be limited by the concentrations of interfering cations in the sample matrix. With increased concentrations of interfering cations, ion exchange with the target ion may be reduced through competition for ion exchange sites. Although such effect should be mitigated by the fact that in most experiments the capacity of the coated resin far exceeded the metal ion content of the sample (exclusive of Na (I)). Figure 2.4 shows the counts measured in 350 µl of a 400 nCi/ml solution of ^{137}Cs versus time. The measurements were made in a realistic matrix with an alkaline pH and a large (~10^7 fold) excess of Na (I). As the figure

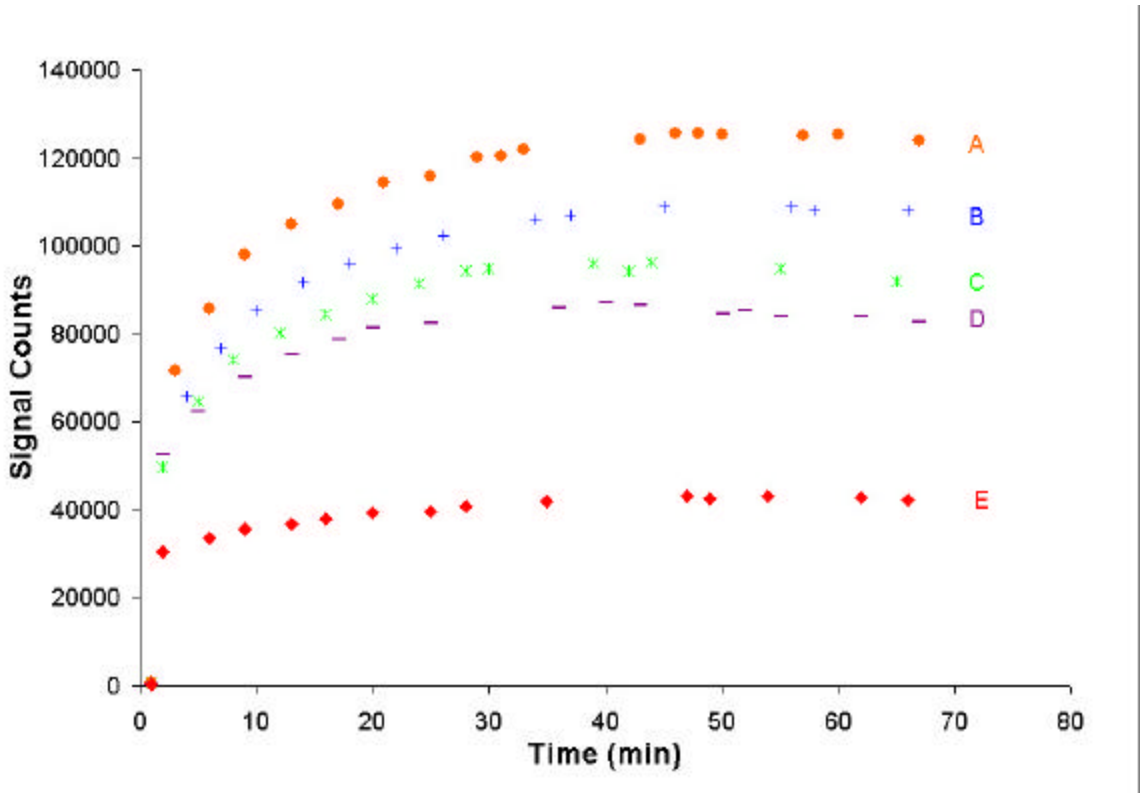

Figure 2.4 Signal counts versus equilibration time (min.) within several sample matrices that contain interfering metal ions. A) 10^{-5} M Al (III) in 1M NaOH. B) 10^{-5} M Sr (II) in 1M NaOH. C) 1M NaOH. D) 10^{-5} M Cs (I) in 1M NaOH. E) 5-fold diluted tank waste simulant.

shows, a plateau in signal is reached after 35 minutes of exposure. Similar plots were constructed for solutions containing 20, 40, 80, and 200 nCi/ml ^{137}Cs. Each of these plots showed that a plateau was reached by 35 minutes of exposure to the respective solutions. From this study an equilibration time of 35 minutes was set for all subsequent measurements.

Figure 2.4 also shows the uptake process in the presence of potential interferences including uptake in a 5X diluted mock DSSF Hanford waste. The composition of the Hanford simulant and a 5-fold dilution used in these studies are shown in Table 2.1. The simulated Hanford tank waste sample was made by the procedure described by Carlson of Pacific Northwest Laboratories[84]. The chosen simulant approximates a DSSF supernate from Hanford Tank 241-AW-101 with the exception that the total sodium concentration is lower than the actual tank waste (7 M rather than 10 M). The initial rate of uptake of ^{137}Cs is not significantly altered in the presence of these other metals (see initial slopes in the figure). However, the equilibrium signals (in the 30-60 minute range) are different in some instances. Given its extreme complexity it is not surprising that equilibrium signal levels in the Hanford matrix are significantly lowered. In a matrix such as this the possibility of complicated secondary equilibria exists.

Secondary equilibria would effectively alter (in many cases decrease) the concentration of free metal ions in the sample. Since we are far from exceeding the capacity of the resin, the equilibrium signal in the presence of 10^{-5} M Cs (non radioactive) should not be altered. The slight decrease relative to the 1.0 M NaOH matrix (without other metal ions) may simply reflect the reproducibility in

Table 2.1 Hanford DSSF 101-AW stock and diluted simulant composition.

Species	Stock 101-AW Simulant, M	Diluted 101-AW Simulant, M
Na	7.00×10^{0}	1.4×10^{0}
Al	6.95×10^{-1}	1.39×10^{-1}
Ba	8.28×10^{-7}	1.66×10^{-7}
Ca	3.62×10^{-4}	7.24×10^{-5}
K	6.65×10^{-1}	1.33×10^{-1}
Sr	1.00×10^{-7}	2.00×10^{-8}
SO_4	1.52×10^{-2}	3.04×10^{-3}
OH	5.82×10^{0}	1.16×10^{0}
OH (free)	3.04×10^{0}	6.08×10^{-1}
Theoretical pH	1.51×10^{1}	
Cl	9.10×10^{-2}	1.82×10^{-2}
CO_3	1.96×10^{-1}	3.92×10^{-2}
F	6.07×10^{-2}	1.21×10^{-2}
NO_2	1.23×10^{0}	2.46×10^{-1}
NO_3	2.09×10^{0}	4.18×10^{-1}
PO_4	2.45×10^{-2}	4.90×10^{-3}

preparing the fibers. The presence of 10^{-5} M of other metal ions showed an increase in the measured signal for all metals evaluated. Part of this increase may be attributed to the reproducibility in preparing the fibers. However these metals appear to be enhancing the steady-state equilibrium of Cs with the resin. This signal enhancement is believed to be due to an increase in the uptake of ^{137}Cs, since β emission should not be affected. The reason for this enhancement in ion exchange equilibria can be linked to several effects including ion-pair formation, salting-out, and repulsion due to like charges[85]. It has been reported that as ionic strength of the sample matrices increases, so does sorption of electrolytes onto the ion exchanger[86]. Increased sorption of ^{137}Cs into the resin used in our studies would lead to an increase in observed signal. Hydrolysis of cations can alter the concentrations of free metal ions in solution, as well as the pH of unbuffered solutions[86]. The presence of higher valence cations in solution can create exchange sites in the resin that contain higher valence ions than the analyte ion which may effect the uptake of the desired ion.

It also has been reported that there is often a measurable difference in selectivity factors determined by single species experiments and those determined by competitive studies[87-89]. Thus selectivity enhancement observed in the presence of other cations is not unprecedented. The mechanisms that lead to these enhancements however are not well understood, nor well documented in literature. If the general composition of the major components of the waste tank sample are known (often the case), then calibration should be possible. In some real situations, calibration by a standard

addition method may be desirable because it allows the analyte to be measured within the true sample matrix.

2.3.5 Calibration Plots; With and Without Potential Intereferences

A series of calibration plots were made to compare the signal achieved with an uncoated and a resin coated scintillation fibers. These calibration curves are shown in Figure 2.5. The ^{137}Cs samples were made up in 1M NaOH with activities from 4 to 3200 nCi/ml ($3.4x10^{-10}$ to $2.7x10^{-7}$ M ^{137}Cs). Three different curves are represented, coated fibers in, and out (dry condition) of the ^{137}Cs containing solution, and an uncoated fiber in the ^{137}Cs solution. The slopes of the three curves show that the sensitivity of the coated fibers in, or out of solution is much greater than an uncoated scintillation fiber in solution. The decrease in the counts between the calibration curves of the coated scintillation fibers measured dry and in solution verifies that the epoxy-polymer coating does not lead to excessive attenuation of the β particles. The fiber appears to be able to measure β particles both in the resin and in the surrounding solution. Sensitivity (slope) and regression data for the plots appear in the figure. The LOD achievable with the uncoated fibers was 13.10 nCi/ml ($1.11x10^{-9}$ M ^{137}Cs) while the coated fibers measured in solution and in the dry state were 1.83 and 3.65 nCi/ml ($1.54x10^{-10}$ and $3.08x10^{-10}$ M ^{137}Cs), respectively. These LOD values are based on a S/N of 2 with the noise value determined by the rms of the measured background signal.

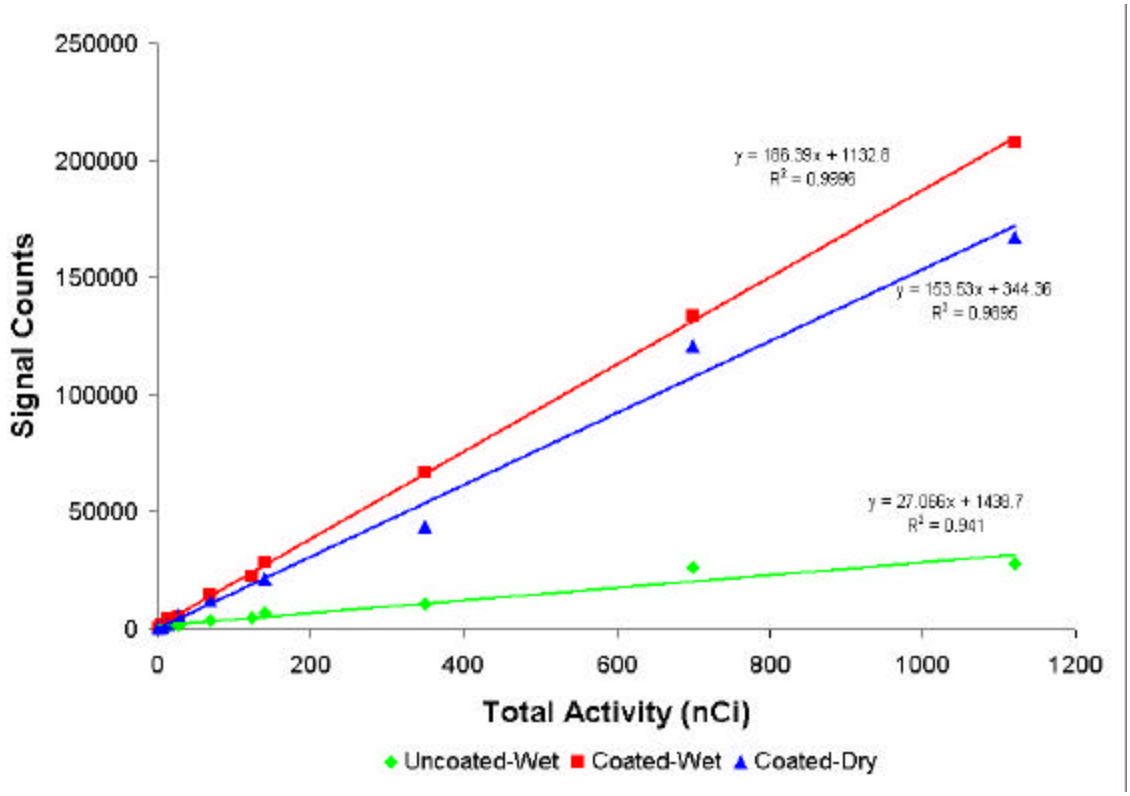

Figure 2.5 Signal counts versus activity (nCi/ml) for fibers measuring ^{137}Cs in solutions of 1M NaOH. A) Coated fibers measured in solution. B) Coated fibers measured out of solution. C) Uncoated fibers measured in solution.

The DMBP used in these studies has been shown to selectively bind Cs (I) in the presence of Na (I), but no other selectivity studies had been performed[78]. A calibration plot for ^{137}Cs in the presence of 10^{-5} M each of Cs (I), Rb (I), and Al (III) is shown in Figure 2.6. Although the number of counts has decreased dramatically from the calibration plot produced in 1.0 M NaOH, the plot does remain linear with a sensitivity which approximately 4-fold lower that in Figure 2.5. In the presence of these interfering metal ions the LOD is $6.3x10^{-10}$ M. Samples of ^{137}Cs with concentrations from 5.3 nCi/ml to 3200 nCi/ml were also made so that they were in a 5-fold dilution of the stock DSSF simulant (composition is shown in Table 2.1). These solutions were measured as before and the calibration curve is also shown in Figure 2.6. The calibration curve was linear, with a sensitivity that was again approximately 4-fold less than in Figure 2.5. The LOD achievable in the simulated tank waste is $7.1 x10^{-10}$ M.

The distribution coefficient (D) was calculated using data collected from uncoated fibers. By subtracting the counts from uncoated fibers measured in the original solution from the counts of an uncoated fiber measured in the same solution after uptake of ^{137}Cs by a coated fiber, the concentration of Cs in the resin can be determined. Then using the estimated mass of resin on a coated fiber (300 μg) we can calculate the distribution coefficient by equation 2.6.

$$D = \frac{(\text{mmole Cs in resin/mass resin})}{(\text{mmole Cs in soln./soln . volume})} \qquad (2.6)$$

For solutions of 3200, 2000, 1000, and 400 nCi/ml the distribution coefficients were calculated to be 493, 490, 430, and 551 ml/g, respectively. This gives an

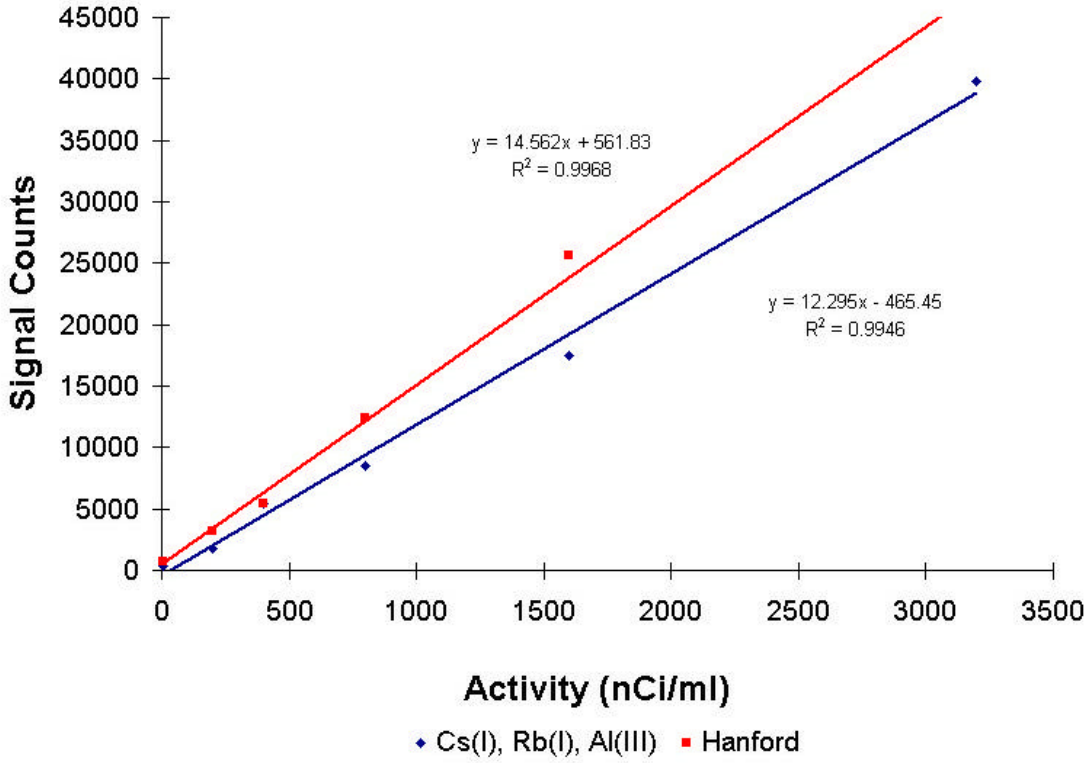

Figure 2.6 Signal counts versus activity (nCi/ml) for fibers measuring ^{137}Cs in the presence of 10^{-5} M each of Cs (I), Rb (I), and Al (III) (A) and in the presence of Hanford tank waste simulant (B).

average of 490 ± 50 ml/g, which is consistent with the reported value being greater than 400 ml/g.[78] Using this value of D the mass of ^{137}Cs on the fiber (dry state) is approximately 6 pg at the LOD.

2.3.6 Non-Specific Resin Studies

The selectivity of the DMBP resins was compared with that of an ion exchange resin (Amberlite IRP-69). The ion exchange resin particles were ground down to match the particle size of the DMBP using a ball mill. The fibers were coated with the ion exchange resin in the same manner as with the DMBP. Fibers were first used to measure the signal from 1600 nCi/ml solutions in 1 M NaOH and containing no interferences, and then the signal from a 1600 nCi/ml solution in a 5-fold diluted tank waste simulant. Signal level for the ion exchange fiber were comparable to resin fibers. However, the former retained only 2% of the original signal observed in the 1M NaOH matrix, when measured in the tank waste simulant. The signal retention was a factor of 7 greater for the DMBP resin, under the same conditions, demonstrating the enhanced selectivity of the DMBP over a strong cation exchange resin.

2.4 CONCLUSIONS

This study has demonstrated chelating scintillation fibers for use in quantifying activities of radioactive metals in alkaline, aqueous samples, and in simulated tank waste. The use of these fibers allows for simplified sampling,

extraction, concentration, and introduction into an analytical instrument. Reducing these typically separate steps into one step is advantageous to reducing sample handling by workers, which in turn reduces worker exposure to radiation sources. The coating of the scintillation fibers with a Cs selective DMBP has shown to substantially improve the sensitivity over uncoated scintillation fibers. Calibration curves are necessary to accurately quantitate the activity of ^{137}Cs within a sample matrix. General matrix conditions are known for most waste tanks making calibration of the fibers possible. The DMBP showed good selectivity for Cs (I) over other metals. With the use of other highly selective coating materials, fibers could be created to quantitatively monitor an array of analytes. For example, a DMBP resin in the diphosphonic acid rather than diphosphonate form has been shown to extract both Cs (I) and Sr (II) from alkaline solutions[90].

CHAPTER 3

ENHANCED CHEMI-MECHANICAL TRANSDUCTION AT DISORDERED NANOSTRUCTURED INTERFACES

3.1 INTRODUCTION

Microfabricated cantilevers that have been commonly used in scanning probe microscopies have become increasingly popular as transducers in chemical and biological sensors [69, 91-96]. This growing fundamental and practical interest in cantilever-based sensors can be explained primarily by two factors. First, a microcantilever transducer directly converts changes in the Gibbs surface free energy created by surface-analyte intermolecular interactions into measurable mechanical responses. Second, the sensitivity of these cantilevers to small quantities of analytes is superior to that of many other transducers. Using gold-coated cantilevers bearing proper molecular receptors, ultra-low (ppb) concentrations of toxic gases in air [92, 94] and metal cations in water have been detected[95]. Other practical applications of cantilever-based sensors can be gained from differential [69] or more sophisticated algorithms [94] applied to responses from cantilevers arranged in arrays. The measurement of changes in surface stress less than 10^{-4} N m^{-1} is possible when appropriate cantilever designs are combined with sensitive deflection measurements[97, 98]. Cantilever deflection is caused by a differential surface stress [72] and, consequently, unequal interaction of the analyte with opposite sides of the cantilever is

therefore important. Modification of only one side of silicon or silicon nitride microcantilevers with smooth polymer coatings or monolayers of reactive receptors is commonly employed [69, 93-96, 99, 100]. Our approach, however, consists of creating cantilevers having sides that are both chemically and structurally different. It is believed that the creation of nano-sized metal clusters on one side of a cantilever will be especially advantageous in designing chemi-mechanical transducers with large intrinsic enhancements in analyte induced deflection. Colloidal and optical properties of metal clusters organized into two- and three-dimensional (2- and 3-D) structures with submicrometer features have been extensively explored [101-105]. Importantly, similar procedures of receptor immobilization can be applied to smooth and nano-structured gold surfaces [101, 103, 104]. It is also important to note that cantilever deflection is governed by the same intermolecular and surface forces as those acting in colloids and porous media [106, 107] or in small gaps between macroscopic surfaces [106, 108, 109]. Theoretical evaluations as well as direct measurements of mechanical stresses provide some evidence [106, 107] that integral stress in surface-confined colloids may exceed the `true' surface stress of smooth solids by several orders of magnitude.

3.2 EXPERIMENTAL SECTION

3.2.1 Materials and Chemicals

Triangular, open structure, silicon nitride cantilevers (length 350 μm, thickness 600 nm) were obtained from Park Scientific [99, 100]. The silver and chromium metals deposited on the cantilevers were obtained from Alfa Aesar and Kurt J. Lesker Company, respectively, and used as received. The following chemicals were all purchased from Sigma or Aldrich and used as received: the test hydrocarbon analytes, 2,7-dimethylnaphthalene (DMN), 2,3-dihydroxynaphthalene (2,3-DHN), 2,7-dihydroxynaphthalene (2,7-DHN), tolazoline, ephedrine and tetrachloroethylene (TCE), and 20 nm gold particles. All other reagents used in these studies were purchased from either Sigma or Fisher Scientific and used as received. All water used to prepare solutions was obtained from a Barnstead E-Pure water filtration system. Ultra high purity nitrogen was used as the carrier gas in all gas phase experiments. Buffer solutions for liquid phase measurements consisted of monobasic and dibasic sodium phosphate dissolved in ultrapure water. The ratio of the two components was fixed to yield a buffer of pH 7. All liquid phase analyte solutions were prepared in this buffer that is also called the background solution. Heptakis-6-mercapto-β-cyclodextrin (HM-β-CD) was prepared using the method of Rojas, Koniger, and Stoddart. [110] by the scheme shown in Figure 3.1.

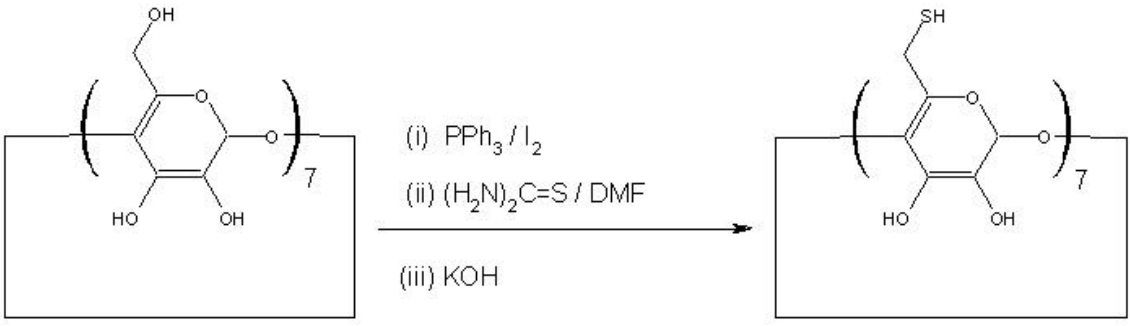

β-CD (HM-β-CD)

Figure 3.1 Preparation of scheme of heptakis-6-mercapto-β-cyclodextrin (HM-β-CD)

3.2.2 Instrumentation

Cantilever deflection measurements were made by reflecting a 5 mW diode laser (Coherent) operating at 632 nm off the cantilever tip and onto a position sensitive detector (built in-house). The output signal was processed using a lock-in amplifier (Stanford Research Systems). An 1-ml flow cell housing a cantilever holder was used for vapor-phase measurements. TCE and DMN vapors were delivered into the cell via a syringe pump through a T-joint and a 4-way valve, which enabled switching between pure nitrogen and diluted analyte. The degree of analyte dilution was defined by the syringe pump flow rate divided over a total flow rate. The latter was measured at the cell outlet using a mass flow meter tube. The entire instrumental apparatus was located on a vibration isolation table in a thermally controlled environment.

For liquid measurements the MC was mounted in a 100-µl flow cell from where it could be exposed to various solutions. The solutions were delivered to the flow cell via a 10ml syringe connected to a 2-way valve. This valve was connected in series to a second 2-way valve that was connected to a 50ml syringe. Figure 3.2 is a picture of the gravity fed liquid flow cell. Typically the 50 mL syringe was filled with a 25mM phosphate buffer at pH 7, and the 10ml syringe filled with the same buffered solution containing a specific concentration of an analyte. The pH of the solutions was measured using an Orion SA 520 pH meter (Thermo Orion, Beverly, MA).

Electrochemical measurements were carried out using a conventional three-electrode cell. The geometrical area of the samples exposed to the

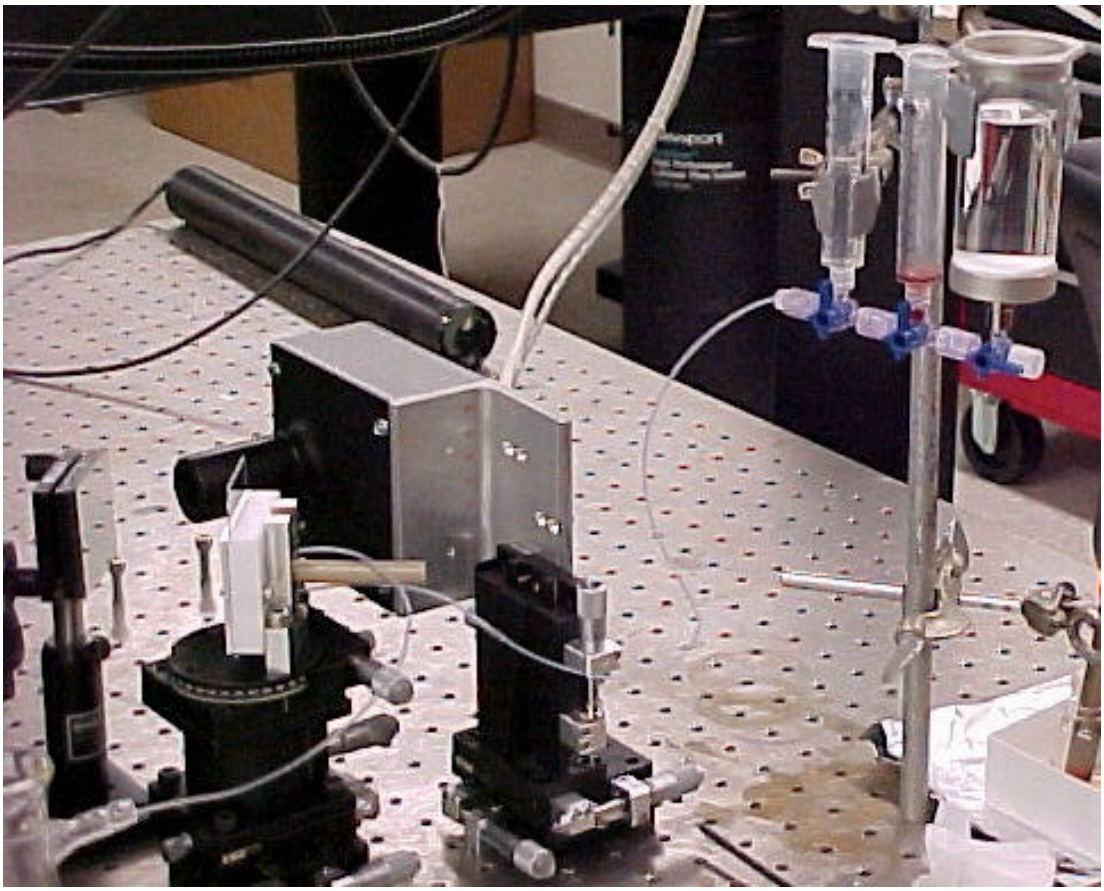

Figure 3.2 Image of gravity fed liquid flow cell used in microcantilever setup.

electrolyte was in the range of 0.5-2 cm^2. An Ag/AgCl saturated KCl electrode and a coiled Pt wire were used as reference and auxiliary electrodes, respectively. The data acquisition and voltage control was performed using a CH Instruments 650 A Electrochemical Workstation (CHI version 2.05). Electrolyte solutions for defining the effective surface areas and thiol coverage were 1.0 M H_2SO_4 and 0.5 M KOH, respectively.

3.2.3 Preparation of Cantilever Surfaces

Two different technological strategies were used in order to create gold nano-structures on one side of the cantilevers. The first strategy (Process 1 in Figure 3.3) involves the deposition of a 40 nm layer of smooth gold followed by electrostatic binding [102] of monodisperse gold nanospheres (with a mean diameter of 20 nm) onto a 4-aminobenzenethiol-modified gold surface. This procedure was performed by coating the cantilevers with the gold layer, 2-3 h immersion in a 1 mg ml^{-1} 4-aminobenzenethiol in methanol solution, and rinsing with copious amounts of methanol then water. The cantilever was then placed in the solution of gold nanospheres for 1-2 days. The cantilever was then removed from the solution and gently washed with water. The second strategy (Process 2 in Figure 3.3) uses chemical dealloying of co-evaporated granular Au:Ag films. This procedure is a thin film adaptation [111] of the method reported by Li and Sieradzki [112] that involves the preferential oxidation of the silver in the alloy. 20-100 nm thick co-evaporated Au:Ag films were used in our studies. The vapor deposition of metals onto the cantilever surface was accomplished using a vapor

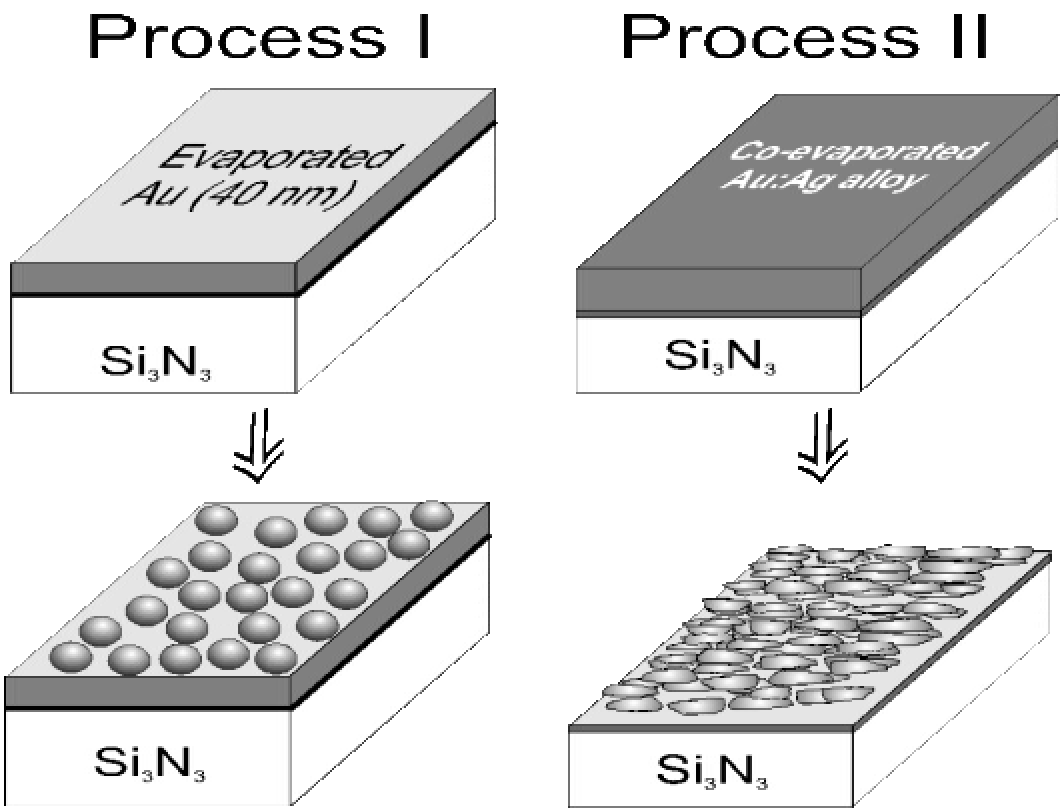

Figure 3.3 Schematic illustration of the techniques used in this study to prepare gold nanostructures. Process I and II depict assembly of 20 nm gold nanospheres on a smooth gold surface and formation of the dealloyed gold surface, respectively. The features in the illustration are not drawn to scale.

deposition chamber. The evaporation of a 15 nm gold layer on a 4 nm chromium adhesion layer was followed by co-evaporation of gold and silver until a composite Au:Ag film of the desirable thickness was formed. The deposition rate was 0.04-0.08 nm s^{-1} and, during co-evaporation, the mass deposition rates were the same for both silver and gold. Both the deposition rates and resulting coating thickness were monitored using a quartz crystal microbalance. The silver was then etched out of the films by placing the cantilever in an aqueous solution of 0.2 w/v % $HAuCl_4$ for 2-3 min.

Chemical modification of the surfaces took place after the surfaces were structurally modified. The surfaces were modified using HM-β-CD in order to form a self-assembled monolayer on the surface. A 1.00 mM solution of the cyclodextrin was prepared in 60/40 DMSO/H_2O and deaerated in a vacuum chamber for 30 min. The cantilever surfaces were cleaned using a 40 s immersion in piranha solution (75% H_2SO_4, 25% H_2O_2) to remove any contaminants. The cantilevers were then immersed in the cyclodextrin solution for 18-20 h Upon removal from the cyclodextrin solution, the cantilevers were rinsed with copious amounts of the DMSO/H_2O solvent.

3.3 RESULTS AND DISCUSSION

Figure 3.4 shows the atomic force microscopy (AFM) micrographs of the nanostructured surfaces. Although AFM is unable to probe very deep crevices, it clearly confirmed a high density of 20 nm gold spheres (Figure 3.4A) assembled

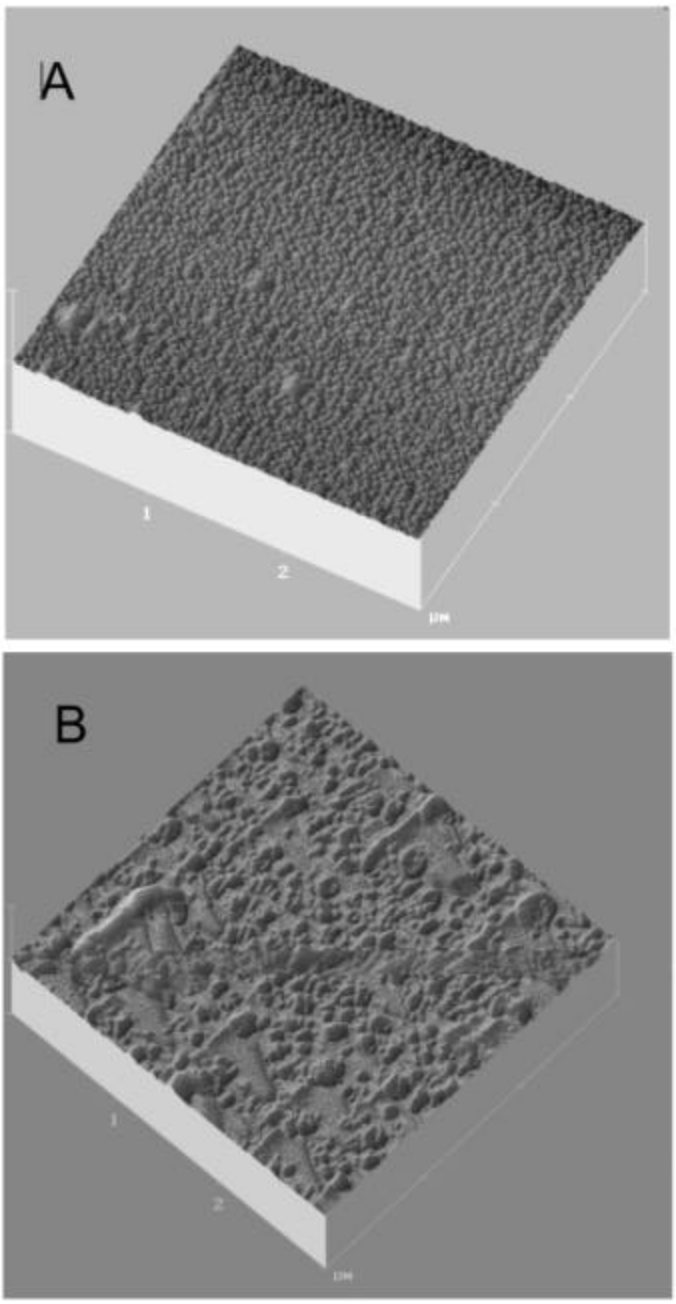

Figure 3.4 AFM images of gold nanospheres assembly (A) and 20nm thick dealloyed gold coating (B). Both scan areas are 3 x 3 μm.

on aminobenzenethiol-modified gold surfaces and larger irregular gold clusters formed as result of dealloying Au:Ag films (Figure 3.4B). To complement the topographic information provided by AFM, scanning electron micrographs of dealloyed surfaces were also obtained [113]. An apparent feature of the nanostructured samples from these micrographs is their increased surface area. More importantly, some of the narrower gaps between gold particles are of the size favorable for involvement of short-range van der Waals, solvation, and steric forces [106]. These quasi 3-D nano-structures may be interpreted as surface confined colloids rather than porous solids. For the dealloyed gold samples, crevices that are narrow may permit strong short-range repulsive or attractive forces upon adsorption of guest molecules are apparent. The total surface area of such crevices increases with increasing thickness of the dealloyed layer. Both the size and the density of the surface confined gold particles increase in the following order: (i) assembly of 20 nm Au-nanospheres, (ii) 20 nm thick dealloyed gold, (iii) 50 nm thick dealloyed gold (not shown in the figures) and (iv) 75 nm thick dealloyed gold. Based on the AFM data, the roughness (RMS value) of the samples in this series was, respectively, 8, 13, 35 and 45 nm.

Gas-phase measurements were conducted on cantilevers with three types of gold surfaces: smooth, gold nanosphere-modified, and dealloyed. Liquid-phase measurements were conducted on cantilevers with two types of gold surfaces: smooth and dealloyed. In most cases the gold surfaces were covalently modified with HM-β-CD. Molecular recognition properties of β-cyclodextrin and analogous compounds have been confirmed gravimetrically

[114], optically [111] electrochemically [115] and using capillary electrophoresis [116].

Figure 3.5 shows the gas-phase responses of the cantilever to DMN in terms of deflection of the cantilever tip. Deflection is also converted to effective differential stress, $\Delta\sigma^{eff}$, using the Stoney's Equation (1.10) as shown in the figure. The response of the cantilever with smooth gold to 83 ppb of DMN (curve 3.5a) was approximately the same as that for cantilevers with Au-nanosphere assembly (curve 3.4c) or with 20 nm dealloyed gold (curve 3.5b) exposed to 10 times less concentrated analyte (i.e. 8.3 ppb DMN). Therefore, a 10-fold increase of adsorbate-induced differential stresses generated on cyclodextrin-modified cantilevers is readily achievable by structuring the gold side of the cantilever. There is even a further deflection enhancement (curves 3.5d and 3.5e) when the thickness of the nanostructures increased. Figure 3.5, curve e also shows a linear decrease in response as the concentration of DMN is decreased. A typical correlation coefficient for calibration plots obtained with the nanostructured surfaces is 0.997. An increased dynamic range due to the increased sensitivity is observed.

Figure 3.6 provides a comparison of the response factors (nm of deflection per ppm) for the two gas-phase test analytes for smooth and nanostructured MCs with immobilized receptor phases. Nanostructuring influences the observed selectivity as the best response for DMN was observed with the 50 nm dealloyed cantilever while the thicker 75 nm dealloyed cantilever provided the largest response to TCE. Note also that a simple monolayer of mercapto-ethane

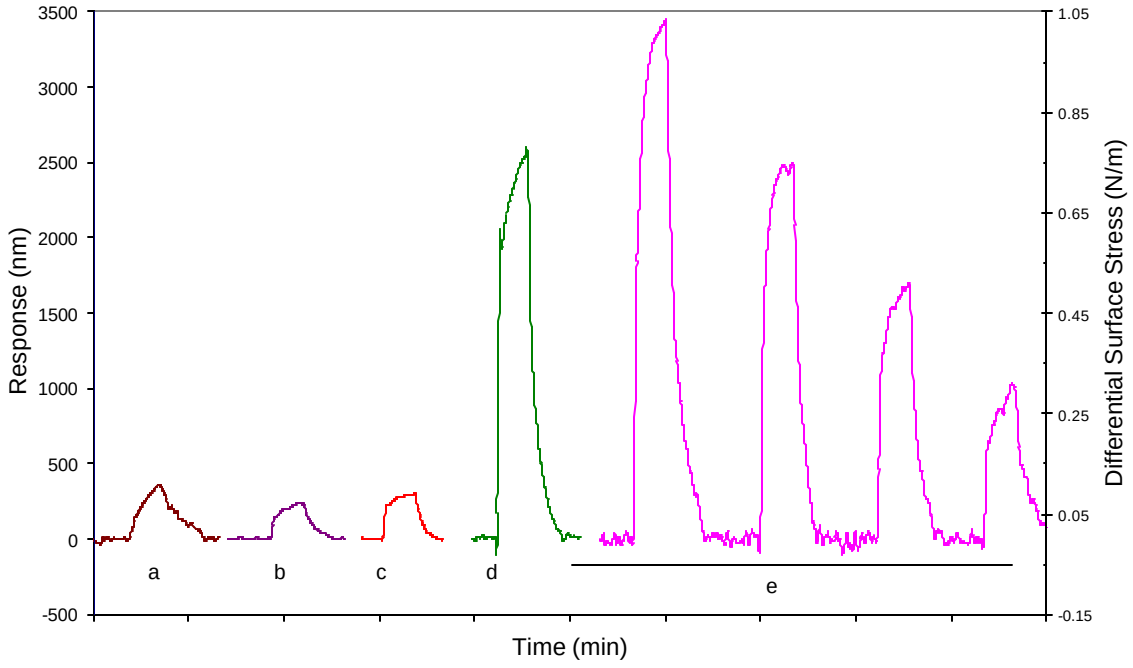

Figure 3.5 Enhanced responses of β-cyclodextrin modified cantilevers to DMN as a result of nanostructuring the gold-coated side. The responses are 83.0 ppb DMN on smooth gold (a); 8.3 ppb DMN on 20 nm dealloyed gold coating (b); 8.3 ppb DMN on 20 nm gold nanosphere assembly (c); 8.3 ppb DMN on 75 nm dealloyed gold coating (d); 8.3, 5.5, 2.8, and 1.4 ppb DMN on 50 nm dealloyed gold coating (e).

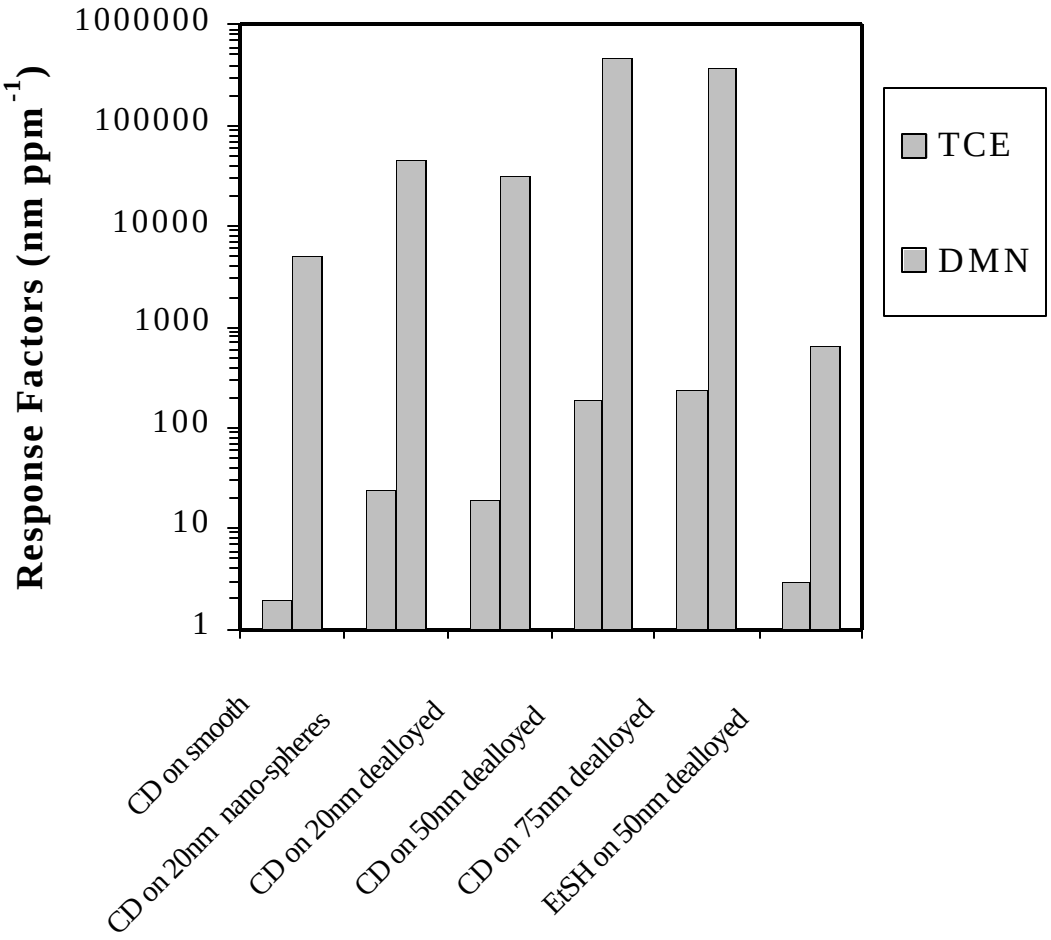

Figure 3.6 Comparison of the sensitivities of receptor coated microcantilevers for the two test analytes. In one case the immobilized phase was mercapto-ethane and in the other cases the HM-β-CD.

provides responses to these analytes. However, the sensitivity is considerably less than with the equivalent nanostructured cantilever with cyclodextrin receptor. Selectivity as indicated by relative chemi-mechanical responses to the two analytes is also considerably larger for the cavitand receptor (2500 versus 200 for mercapto-ethane cantilever).

Enhancement factors (response factor for nanostructured cantilever/response factor for smooth gold cantilever) and limits of detection (LODs, based on a signal three times the baseline noise of 20 nm deflection) were determined from calibration plots for serial dilutions of DMN and TCE. These values appear in Table 3.1. In the best cases, the enhancement factors were about two orders of magnitude and the LODs are in mid-part-per-billion range for TCE and very impressive mid-part-per-trillion range for DMN. A comparison of the LODs achieved for liquid–phase measurements for the analytes, 2,3-DHN, 2,7-DHN, tolazoline, and ephedrine on smooth and dealloyed gold surfaces is shown in Table 3.2. Independent experiments were performed to verify that the observed increased response with nanostructuring exceeds the increased available receptor phase on the dealloyed surface. Our surface plasmon resonance experiments revealed that the HM-β-CD bound to smooth gold surfaces with a density slightly exceeding a monolayer. Inspection of the gold(III) oxide reduction wave in cyclic voltammograms of smooth and 50 nm dealloyed gold surfaces indicated a 13-fold increase in surface area with nanostructuring. Using the voltametric method reported by Porter and coworkers for the oxidative desorption of alkylthiols from gold surfaces [117], we obtained

Table 3.1 Comparison of limits of detection, LOD, and enhancement factors, EF, (relative to smooth gold cantilevers) for Nanostructured surfaces with HM-β-CD receptor phases.

Compound	Surface	LOD	EF
DMN	gold beads	1.5 ppb	9
	20 nm dealloyed	2.0 ppb	6
	50 nm dealloyed	0.14 ppb	93
	75 nm dealloyed	0.17 ppb	73
TCE	gold beads	2.8 ppm	12
	20 nm dealloyed	3.4 ppm	10
	50 nm dealloyed	0.34 ppm	97
	75 nm dealloyed	0.28 ppm	120

Table 3.2 Comparison of the LODs achieved for liquid–phase measurements for the analytes, 2,3-DHN, 2,7-DHN, tolazoline, and ephedrine on smooth and dealloyed gold surfaces.

Compound	Surface	LOD (ppm)
2,3-DHN	Smooth	288
	50nm dealloyed	4.80
2,7-DHN	Smooth	250
	50nm dealloyed	7.50
Tolazoline	Smooth	300
	50nm dealloyed	17.0
Ephedrine	Smooth	326
	50nm dealloyed	31.3

surfaces coverages of 1.7×10^{-9} and 10×10^{-9} mol (thiol group)/(cm^2 geometric surface area) for the smooth and 50 nm dealloyed surfaces, respectively (note: Porter observed coverages of about 0.9×10^{-9} mol/cm^2 for alkylthiols). Conversion of these numbers to moles of HM-β-CD per surface area would require knowledge of the average number (of the 7 available) thiol groups involved in surface binding. Assuming that this number is the same for both types of surfaces, there is approximately a 6-fold increase in available receptors with nanostructuring of cantilevers. The fact that this number is less than the apparent increase in surface area indicates limited access of the moderately large macrocycle receptor to gold surfaces found in narrow crevices. Similarly, this highlights the contribution of surface stresses associated with short-range steric forces upon analyte binding to receptors in these confined spaces to the observed large cantilever responses. This is additional proof that response enhancements clearly exceed the increase in available receptor phase when comparing conventional to nanostructured microcantilevers.

3.4 CONCLUSIONS

We have shown that the asymmetric nanostructuring of cantilever surfaces can lead to two orders of magnitude enhancements in chemi-mechanical transduction. The magnitude of the effective surface stresses generated at the quasi 3-D interfaces significantly exceeds surface free energies of common solids as well as adhesion energies of coating-substrate pairs

frequently used in chemical sensors. The demonstrated micrometer-scale movements of the nanostructured cantilevers are especially attractive as a platform for passive chemically controlled microfluidic systems powered exclusively by energy of analyte-device molecular interactions. Because the implemented asymmetric nanostructuring only slightly increases the deflection noise of the cantilever in equilibrium, it also provides an approach to sensors with significantly improved limits of detection and dynamic range. Since different types of nanostructures lead to different enhancement factors with respect to different chemicals, nanostructuring of cantilever surfaces can also create new modes of response selectivity. In comparison to several other coatings investigated in our study, dealloyed gold provided the most efficient transduction of chemical stimuli into mechanical responses. The implemented technology of dealloyed gold is highly compatible with conventional microfabrication and, we believe, can be extended to a great variety of other materials. Therefore, cantilever-based transducers with nanostructured surfaces described herein will have a broad impact on the future development of micro- and nano-fabricated chemical sensors, actuators and integrated `lab-on-chip' devices.

CHAPTER 4

ENHANCING CHEMI-MECHANICAL TRANSDUCTION IN MICROCANTILEVER CHEMICAL SENSING BY PATTERNED SURFACE MODIFICATION

4.1 INTRODUCTION

Recent work from several research groups [69, 93, 94, 99, 100, 113, 118-124] confirms that sensors based on MCs have substantial potential for various analytical applications. In order to fully realize this potential, however, further optimization of MC designs and chemical coating selections may be required. A clean smooth solid surface generally exhibits a tensile (positive) surface stress due to the electronic arrangement of the atoms composing the surface. Significant changes in stress on a surface can occur when surface atoms are caused to rearrange due to adsorption by a chemical species[125]. The change in stress can be either compressive or tensile depending upon the nature of the adsorbed species and its interaction with the surface. The surface stress and surface free energy are related by the Shuttleworth equation (Equation 4.1),

$$\sigma = \gamma + \frac{d\gamma}{d\varepsilon_e} \qquad (4.1)$$

where σ is the surface stress, γ is the surface free energy, and ε_e is the elastic surface strain that is defined as dA/A where A is the surface area and dA is the elastic increase in surface area[71, 125, 126]. In principle, the second term can

be comparable to the surface free energy and assume a positive or negative value[71]. However, a general trend is that if the initial surface Gibbs free energy is large, then modulation in surface stress and, hence, MC response can be large. For example, pure gold surfaces in contact with air have large surface free energies, typically exceeding 1 N m^{-1}. Not surprisingly, when MCs coated on one side with gold are exposed to alkylthiols in the gas phase very large total responses are observed as the thiol compounds covalently bond to the gold[91, 92].

In order to impart selectivity to MCs used in analytical sensing, chemically selective receptor phases need to be immobilized on one of the sides of the MC. Ideally, the interaction of the analyte with the receptor phase, while being selective, is reversible and exhibits reasonable kinetics for sensing applications. The use of MCs with reversible receptor phases for measurements in liquids (e.g., aqueous solutions) has not received a great deal of attention. In part, this is because organic receptor phases in water possess surface free energies that are substantially smaller than the gold-gas phase case mentioned above. Therefore, modulation of surface stress is smaller and often within an order of magnitude of the inherent noise of MCs mounted in aqueous environments[113]. This gives rise to low signal-to-noise levels and somewhat limited dynamic range.

In chapter 3 the use of nanostructured MCs in gaseous and aqueous environments to improve the transduction of molecular recognition events into cantilever responses was discussed. The limitations of smooth surface MCs were overcome by creating a highly disordered nanostructured surface on one

side of the MC and further modifying the surface with a self-assembled monolayer (SAM). The nanostucturing process increased the available surface for SAM phases and analyte binding and creates a quasi-3-D structure that is colloidal in nature. Importantly, the short-range forces associated with intermolecular interactions in the tight interstitial spaces of colloidal systems can be very large[106]. The in-plane component of these forces can serve to efficiently convert the chemical energy associated with analyte-receptor binding into mechanical energy manifested as MC static bending. The same disordered nanostructured MC was used to stabilize thin films of a vapor deposited chemically selective phase. It was shown that limits of detection for both modes of operation, SAMs and thin films, could be improved by orders of magnitude over MCs with smooth surfaces[127]. The work presented here in Chapter 4 uses thin films rather than SAMs. With thin films the stress that gives rise to bending of the MC results from swelling or contractions of the bulk phase upon absorption of an analyte. The degree of swelling-induced MC bending upon analyte absorption scales with the film thickness and thus thin films can lead to larger bendings than SAMs. There are also some disadvantages to thin films. Thin films result in prohibitively slower responses than SAMs, and the stress created in a thin film by absorption of an analyte may exceed the energy of the MC surface-film adhesion, resulting in a stress-slip condition. This stress-slip condition, which results in poor transduction of the stress generated in the film by analyte absorption, is problematic with smooth surfaces and weakly interacting film-surface interfaces.

Herein, we report on another approach to improve sensitivity of MCs in liquid-phase measurements using patterned modification of the MC surface. The distinction between this work and the work presented in Chapter 3 is the degree of order of the surface structuring. The structuring in Chapter 3 is a completely disorganized surface, while the structuring presented here is done in an orderly, organized manner. The advantage of an ordered surface over the disordered surface is that it allows mechanical modeling of the structure to become a possibility. The ability to perform mechanical modeling, though not done in this work will provide a better understanding of how these surface modifications enhance the device sensitivity. The surface modifications in our present work have larger features than the nanostructured surfaces reported previously and are created by two different methods. The first method uses a focused ion beam (FIB) to controllably mill away areas of the silicon surface. The second method of modification uses the FIB to dope regions of the silicon surface of the MC with Ga^+ impurities. The silicon MC is then etched in a hot KOH bath. KOH is an anisotropic etchant for silicon and etches the <111> crystal plane of silicon much slower than the <100> or <110> crystal planes, regardless of dopants[128, 129]. The doped areas of the silicon surface of the MC etch at a slower rate than areas that are not doped[130-137] and patterns can be created based on the doping of the surface. In this case alternating areas of doped and undoped silicon were patterned on the MCs, which after etching in KOH left V-shaped grooves across the width of the MC, that depending on the dimensions were truncated at the bottom. The nanoscale channels across the width of MCs were then filled with

an organic receptor phase. As analytes absorb into the receptor phase the stress created in the phase can be more efficiently transferred to the surface creating a greater differential stress and thus more bending.

4.2 EXPERIMENTAL SECTION

The silicon MCs that were used in this study are commercially available, approximately 1.5 μm thick, beam-shaped and coated with a layer of aluminum (MikroMasch, Tallinn, Estonia). Each chip carried two sizes of MCs, 400nm long by 100nm wide, and 200nm long by 50nm wide, the latter size was used for these studies. The aluminum layer was removed from the MCs by immersing them in aqua regia (75% HCl, 25% HNO_3) for 5 minutes. The MCs were then rinsed in deionized (DI) water for 10 minutes, and dried under a gentle stream of nitrogen. The MCs were cleaned in piranha solution (75% H_2SO_4, 25% H_2O_2) and then rinsed in DI water and dried under a gentle nitrogen stream. The surfaces of the MCs were then modified using a FIB (FIB 200, FEI Co., Hillsboro, OR, USA) by milling grooves across the entire width of the MCs to depths of 200 or 400 nm. An example of a milled lever is shown in Figure 4.1. As seen in the figure the grooves are positioned approximately every 800 nm and are roughly 400 nm wide. The grooves covered the 100μm nearest the base of the 200μm long MCs. The entire MC was not milled in order to leave an area to efficiently reflect a readout laser beam.

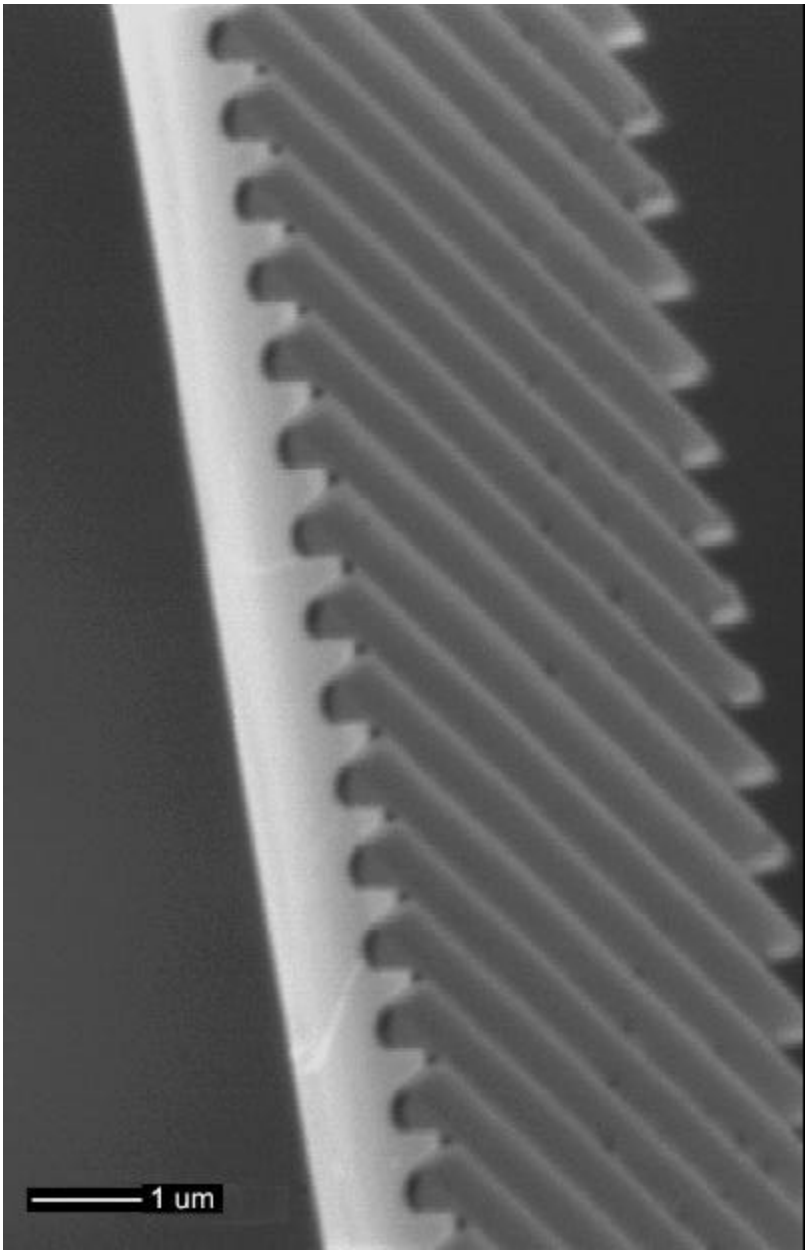

Figure 4.1 Focused ion beam image of grooved microcantilever with 400nm deep grooves.

Pattern files were created for the MCs that were grooved by doping and etching of the silicon surface. These pattern files defined the areas of the regions to be doped and controlled the spacing between the doped areas for the FIB. The defined areas were exposed to a 30kV, 1000 pA Ga^+ beam current for the time required to achieve a doping of 10^{16} ions/cm^2, within each defined area. The MCs were then removed from the FIB without further imaging and etched in a 70°C 60% w/w KOH solution for approximately 5 minutes. After etching the MCs were rinsed in DI water for 20 minutes and then dried. Examination by low current FIB was used to see if the etching was completed or if further etching was required to complete the grooves. Figure 4.2 shows an image of the V-shaped grooves produced by this method.

Once the surface of the MC was modified it was placed into a physical vapor deposition (PVD) chamber (Cooke Vacuum Products, model CVE 301, South Norwalk, CT) to be coated with metallic and organic films. The modified surface of the MC was coated sequentially with a thin film (~5.0nm) of chromium, a thin film of gold (~10 nm), and finally a film (100nm) of (2,3-O-dimethyl-6-O-tertbutyl-dimethylsiyl)-β-cyclodextrin (MeSi-β-CD) synthesized in house[138]. The chemical structure and general appearance of this macrocycle, teacup-shaped, molecular receptor are depicted in Figure 4.3. Film thicknesses were measured using a conventional quartz crystal microbalance (Maxtek, model TM-100R, Sante Fe Springs, CA).

The MC was mounted in a 100-µl flow cell from where it could be exposed

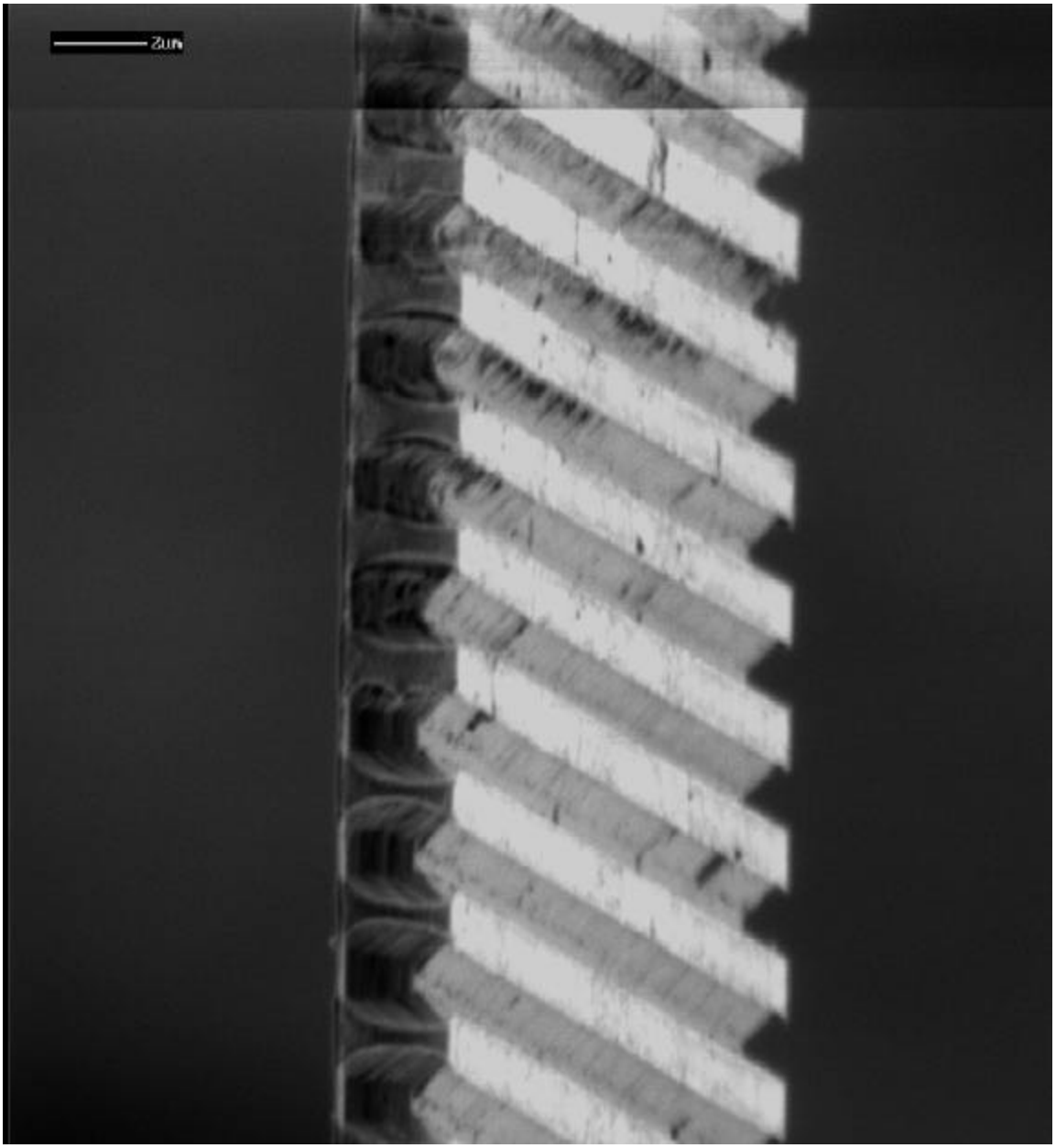

Figure 4.2 V-shaped grooved microcantilever prepared by Ga^+ doping of silicon surface and subsequent anisotropic etching with KOH.

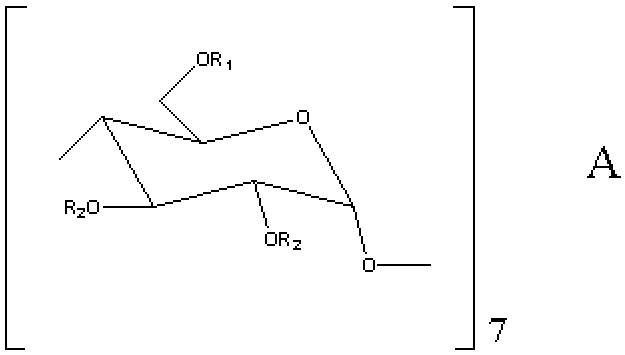

A

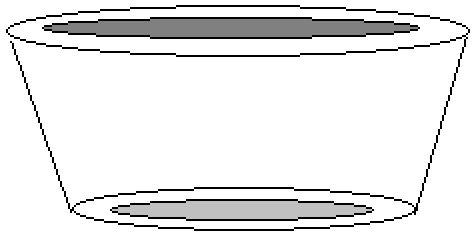

B

Figure 4.3 Monomeric units (A) and general shape (B) of the functionalized cyclodextrins used as receptor phases. R_1 and R_2 are $(CH_3)_3CSi(CH_3)_3$ (tertbutyl-dimethylsilyl) and CH_3, respectively. The dimensions of a typical β-cyclodextrin are 8 angstroms wide and 6 angstroms deep.

to various solutions. The solutions were delivered to the flow cell via a 10ml syringe connected to a 2-way valve. This valve was connected in series to a second 2-way valve that was connected to a 50ml syringe. Typically the 50 mL syringe was filled with a 25mM phosphate buffer at pH 7, and the 10ml syringe filled with the same buffered solution containing a specific concentration of an analyte. The pH of the solutions was measured using an Orion SA 520 pH meter (Thermo Orion, Beverly, MA). The deflection of the MC was measured using an optical beam bending method shown in Figure 1.17[92]. In this method the deflection of the MC is measured by reflecting a 5mW diode laser (Coherent Laser Corp., Auburrn, CA) operating at 635nm off of the MC and onto a position sensitive detector[127]. The output of the detector was recorded using an Agilent 34970A data acquisition/switch unit (Agilent Technologies, Inc. Loveland, CO) and a pentium computer interfaced by a GPIB connection. The flow cell was imaged using a Watec CCD camera (Edmund Industrial Optics, Barrington, NJ) to assist with alignment of the laser beam on the MC tip.

The analytes and buffer components were obtained from Sigma (St. Louis, MO), or Aldrich (Milwaukee, WI) and used as received. All of the buffer solutions consisted of monobasic and dibasic sodium phosphate dissolved in DI water. The ratio of the two components was fixed to produce a buffer at pH 7. All of the analyte solutions were prepared in this buffer solution. The acids and bases used were obtained from Fisher Scientific (Pittsburgh, PA). The metals used during the coating process were obtained from Alfa Aesar (Ward Hill, MA) or the

Kurt J. Lesker Company (Livermore, CA) at a purity of 99.9%. The MeSi-β-CD was synthesized using the method of Takeo et. al[139].

4.3 RESULTS AND DISCUSSION

When a MC is modified with an analyte permeable coating that is much thicker than a monolayer, a dominant mechanism of MC deflection is analyte-induced swelling of the coating. Such swelling processes may be quantified by evaluating the molecular forces acting within the coating and between the coating and the analyte species. The absorption of analytes into a coating can alter dispersion, electrostatic, steric, osmotic, and solvation forces acting within the coating[106]. The absorption of analytes into the coating requires the creation of a vacancy in the bulk coating [140] and this can give rise to swelling that is characterized by an expansion coefficient[141]. The swelling may effectively produce a stress or a pressure change inside the coating, depending on whether it is described as a solid, or a gel, respectively. This pressure change multiplied by the thickness of the coating produces an apparent surface stress change ($\Delta\sigma_{app}$) that can be used in Stoney's equation to estimate deflections of a MC coated with a thin, soft responsive film. In the case of thin film coatings, nanostructured surfaces improve the transduction of this in-plane stress into cantilever bending by reducing the ability of the thin film coating to slip along the MC surface as it swells. It is also important to note that swelling of soft films that are physically confined in the in-plane dimension on a cantilever surface may

occur preferentially in the out-of-plane dimension and will not produce the desired MC bending.

The response of both surface modified and unmodified MCs coated with a film of MeSi-β-CD to a series of analytes were measured to further study the effect of surface morphology on MC chemical response. Cyclodextrin macrocycle sugar cavitands were chosen as chemical coatings based on their molecular recognition capabilities. Interactions between the cyclodextrin and solutes are based upon size, geometry, and physiochemical properties of both the cyclodextrin and solutes and have shown high degrees of selectivity in chemical separations[116, 142-145]. The response of two surface modified MCs to 2,3-dihydroxynaphthalene (2,3-DHN) were compared with the response of an unmodified MC. The depths of the grooves were 200nm for one MC and 400nm for the second. The grooved region of each of these MCs was preferentially coated with 100nm of MeSi-β-CD using a mask, as was an ungrooved MC. The response of these MCs to a series of dilutions of 2,3-DHN over the range 25 to 1000 ppm is shown in Figure 4.4. As can be seen in the figure the 400nm grooved MC gave the greatest response to each concentration of 2,3-DHN, followed by the 200nm grooved MC. The unmodified MC showed no clear measurable response even for the higher concentrations of 2,3-DHN. The magnitude of the response of the 400nm grooved MC was three times greater than that of the 200nm grooved MC. The response of the 400nm and 200nm deep grooved MCs were linear with linear regression (R^2) values of 0.97 and 0.96, respectively. The 2,3-DHN limit of detection for the 400nm deep grooved

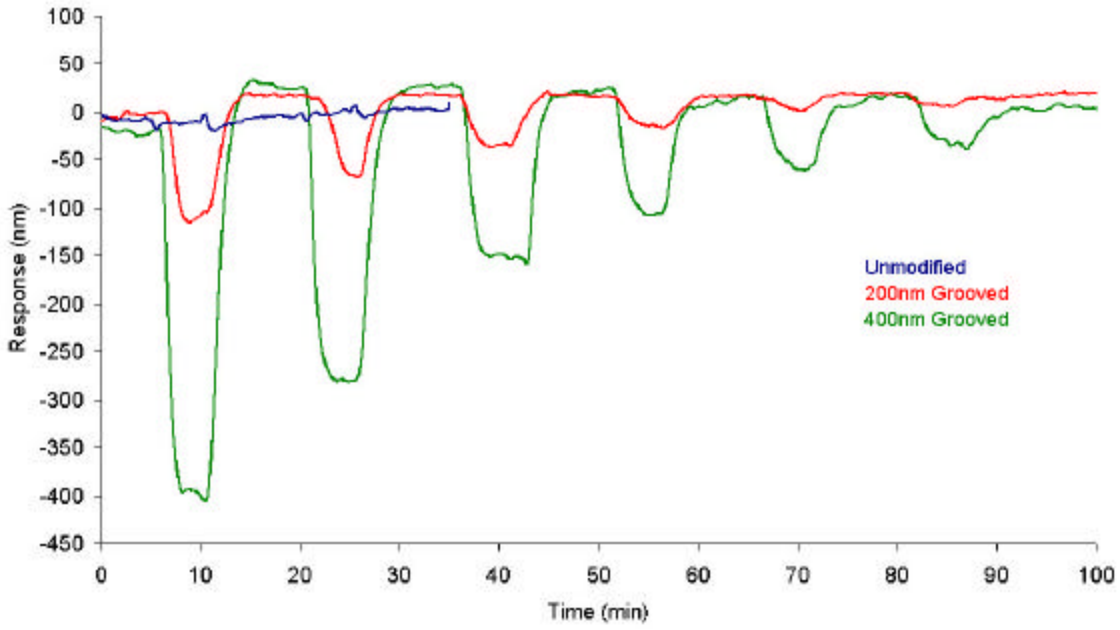

Figure 4.4 Response curves for surface modified microcantilevers to 2,3-DHN. (A) Ungrooved, (B) 200nm deep grooves, (C) 400nm deep grooves.

MC was 36ppm. This demonstrates that the addition of grooves leads to improvement in MC sensitivity. In general, deeper grooves increased the sensitivity over shallower grooves. We believe that the confinement of the receptor phase in the grooves allows the stress generated within the phase by absorption of analyte to be transduced into surface stress of the MC more efficiently. While confinement of the film in grooves may serve to reduce stress induced slippage, there are other response factors involved. The addition of grooves to the MC will also reduce the spring constant, making the cantilever more responsive, but also more noisy. The resonance frequencies of the surface modified MCs were measured and from this relative spring constants were determined from the equation:

$$f \propto \sqrt{\frac{k}{m}} \qquad (4.2)$$

where f is the resonance frequency in Hz, k is the spring constant in N m^{-1}, and m is the mass of the cantilever in kilograms. By measuring the resonance frequency and estimating the mass of each cantilever the spring constant can be estimated. The measured resonance frequencies were 61.4 kHz for the ungrooved MC, 52.0 kHz for the 200nm deep grooved MC, and 39.9 kHz for the 400nm deep grooved MC. The mass of the ungrooved MC was estimated from the volume of the MC and the density of silicon. For the grooved MCs the volume of the grooves was calculated and subtracted from the mass of the ungrooved MC. From this information the spring constants of the ungrooved, 200nm deep grooved, and 400nm deep grooved MCs were found to be in the

ratio of 2.7 to 1.8 to 1.0 respectively. Since *E* and *k* are proportional to each other[146], the expected changes in response due to underlying structural changes should be a factor of 1.8 when comparing the smooth to the 200nm grooved MCs and a factor of 1.5 when comparing the 400nm to the 200nm grooved MCs. The observed changes in responses to 2,3-DHN shown in Figure 4.4 are considerably larger. This suggests that both changes in spring constant and confinement of the responding film within grooves for the milled MCs are contributing to the observed improvement in sensitivity. Finite element analysis of modified microcantilevers could be used to investigate which of these factors is more important in the improvement of the MC sensitivity[147].

A surface modified MC with 400nm deep grooves was exposed to a series of VOCs (trichloroethylene, chloroform, and methylene chloride) each at a concentration of 100ppm. The responses of the modified MC to these analytes are shown in Figure 4.5. The variations in response to these analytes demonstrates that the MeSi-β-CD film gives modest selectivity to the MCs. Figure 4.5 also shows the reproducibility of the MC responses over multiple injections of an analyte. A calibration curve was obtained for the DNAPL trichloroethylene in the concentration range of 1-1000ppm. Above a concentration of 50ppm the responses leveled off indicating saturation. However, below 50ppm the responses (Figure 4.6) were linear and gave a linear regression (R^2) of 0.98. Although this particular MC system was not optimized (see below) it yielded a TCE limit of detection of 980ppb.

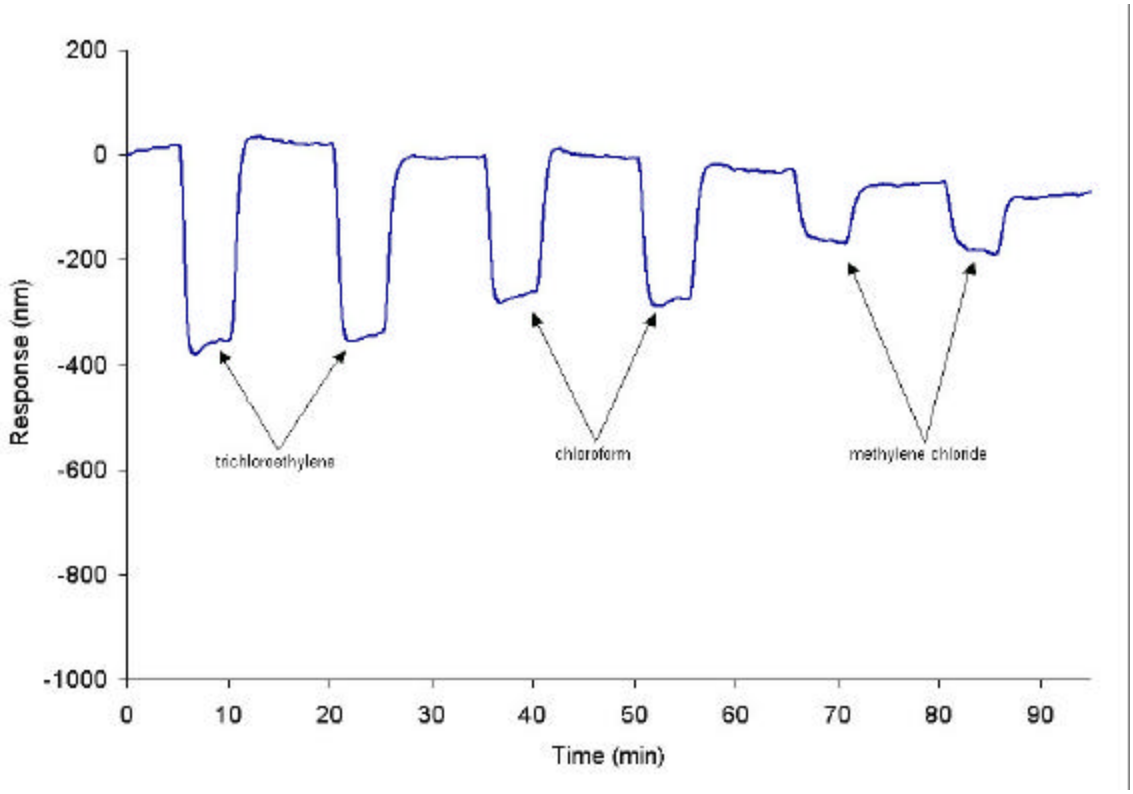

Figure 4.5 Response curve of 400nm deep grooved microcantilever to a series of VOCs.

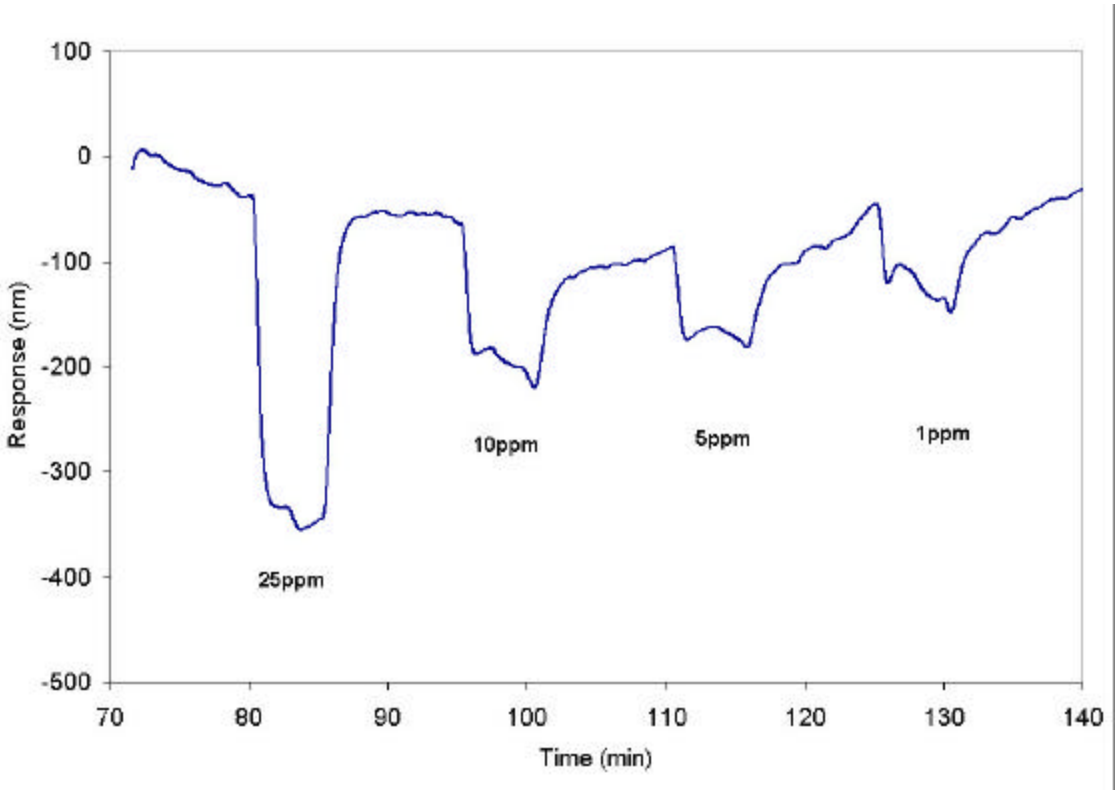

Figure 4.6 Responses of a 400nm deep grooved microcantilever coated with 100nm MeSi-β-CD to Trichloroethylene solutions of different concentrations.

The effect of MC thickness was studied on a 400nm deep grooved MC. Three MCs were thinned by 200, 400, and 600nm, respectively using the FIB. The surface of these MCs were grooved with 400nm deep grooves and then coated with MeSi-β-CD. The responses of each of these MCs to 100ppm trichloroethylene were measured and are shown in Figure 4.7. As the MCs become thinner the responses increase without an apparent decrease in the S/N ratio. Thus, a several fold improvement in limits of detection over what we have found in this work above should be possible with thinning.

The work presented was done entirely with MCs that were grooved by milling with the FIB. However, MCs that were doped and etched have been shown to give similar enhancements as the milled ones. Figure 4.8 shows the response of an ungrooved MC and a V-shaped grooved MC to the analyte 8-hydroxyquinoline. The work with V-shaped grooves has not yet reached maturity, but is believed to have great potential. From strictly a geometric perspective, a V-shaped grooved MC such as the one shown in Figure 4.2 that experiences only a 0.1% in-plane swelling of a thin film in the groove is capable of producing a deflection at the tip of 4 μm per 100 μm of length. This is an enormous deflection that is the result of large internal pressures generated in the thin film rather than a flimsy MC.

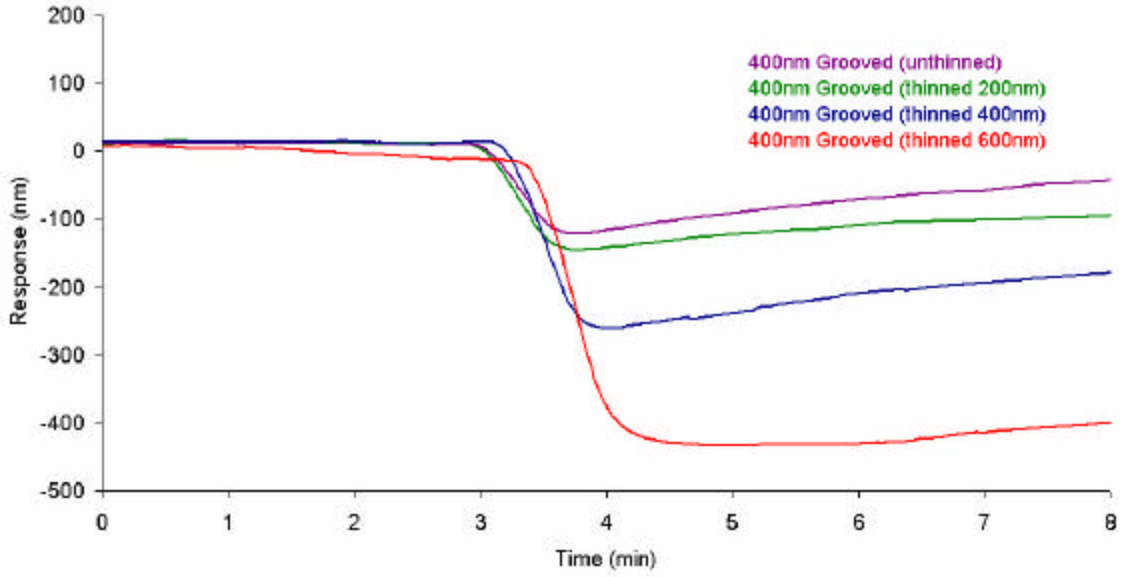

Figure 4.7 Response of 400nm deep grooved microcantilever to trichloroethylene after thinning of the microcantilever surface. (A) Unthinned, (B) Thinned by 200nm, (C) Thinned by 400nm, (D) Thinned by 600nm.

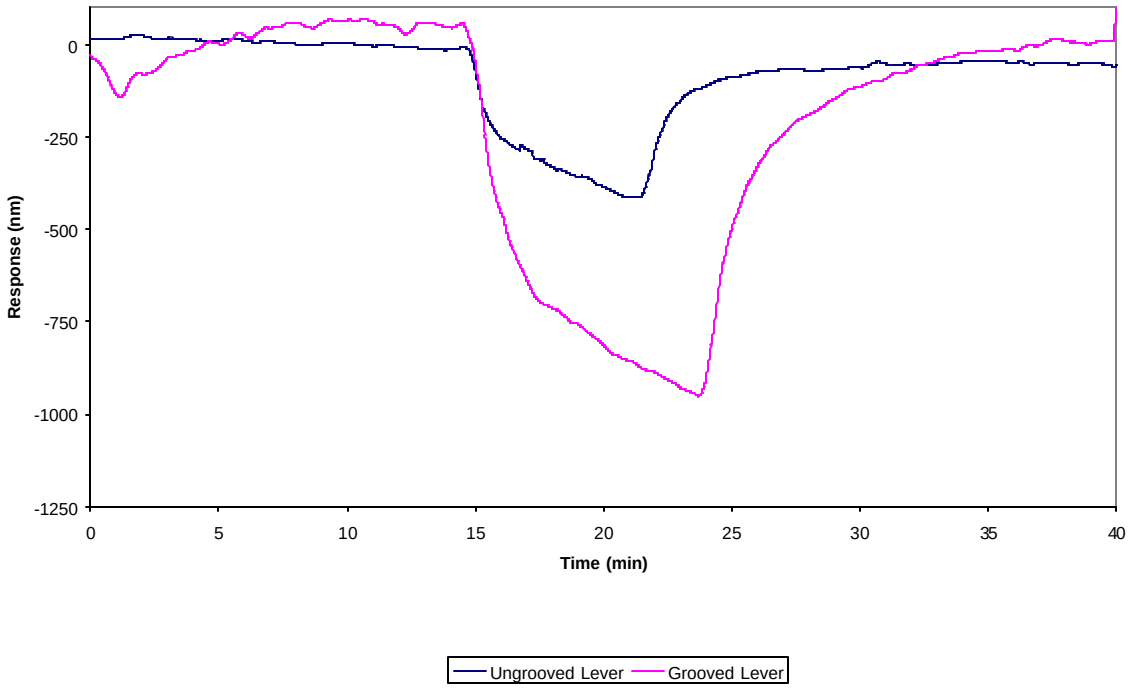

Figure 4.8 Response of ungrooved MC and a V-shaped grooved MC to 80ppm 8-hydroxyquinoline.

4.4 CONCLUSIONS

Surface modification of MCs has shown the potential to increase sensitivity of these devices as chemical sensors. This increase in sensitivity is produced by improvement of the transduction of stress created in a chemical receptor phase, by analyte adsorption or absorption, to surface stress on the MC. With an asymmetric MC this leads to a larger differential stress, which results in larger deflections of the MC tip. It should be noted that previous MC work with disordered nanostructured surfaces with smaller features yielded superior limits of detection (125 ppb for 2,3 DHN) using a similar coating[127]. This may indicate that the scale of the features on the grooved MCs (100's of nm) used in this work needs further optimization. Future optimization of MC chemical sensors will involve increasing the thickness of the coatings, and investigating further the effects of groove size and density and thinner cantilevers.

CHAPTER 5

MISCELANEOUS WORK AND CONCLUDING REMARKS

5.1 INTRODUCTION

During the course of the work described in prior chapters some other work was performed to support or follow-up other projects. In particular, two main projects that were undertaken involved an attempt to detect β-particles using MCs, and the application of a new technique, matrix assisted pulsed laser evaporation (MAPLE) to controllably apply thin films to the individual microcantilevers on a single chip. The attempt at β-particle detection was a follow-up to the development of the chelating scintillation fibers discussed in Chapter 1, while the application of the MAPLE technique was aimed at broadening the range of selective coatings we are able to apply to MCs, and improving the spatial resolution with which we could deposit multiple coatings.

5.2 b-PARTICLE DETECTION WITH MCs

Bimaterial MCs respond to thermal effects due to the differences in thermal expansion coefficients of the two materials comprising the device. They have been shown to respond to heat energies from 10^{-12} to 10^{-14} J depending on the geometry and dimensions of the MC[148-150]. Detection of radioactive

elements by the deflection of the MC caused by the heat lost by an ionizing particle as it passed through the MC was investigated. A capillary column was packed with the chelating resin used in Chapter 2, and loaded with ^{137}Cs by allowing this packed capillary to soak in a 3200 nCi/ml solution of ^{137}Cs. The capillary was then positioned within 1 cm of the MC on a positional stage. The optical beam bending technique, used for the experiments described in Chapters 3 and 4, was used to monitor the deflection of the MC. A typical measurement was started with the direct path from the packed capillary to the MC blocked by a small piece of Al foil, after measuring this background for several minutes the Al foil was removed from the path between the packed capillary and the MC. Distinct deflections due to interaction of the ionizing β-particles with the MC were not observed. The reason that no deflections were observed was most likely due to a combination of two factors. First, the β-particles are of high energy and low mass. As described in Chapter 2 β-particle of the energy emitted by the decay process of ^{137}Cs has a penetration depth of ~ 350 μm through a material with a density of 1 g/cm^3. The second factor is the minute thickness of the MCs (~ 600 nm). Combined, the penetration depth of the β-particle and the comparatively small thickness of the MC leads to the loss of a very small amount of energy as these particles pass through the MC. In fact, less than 0.5% of the particles energy would be lost assuming the energy loss is linear with penetration depth, which it is not as most of a ionizing particles energy is lost as the particle comes to rest. These factors combined with any energy lost by the β-particle as it

escaped the capillary packing, would put us below the sensitivity levels of the MC to heat energies. To date only one literature article that has appear measuring radioactive decay of an element. This article collected the charged particles from an alpha emitter ^{241}Am, on a collector plate and measured changes in the MC resonance frequency due to electrostatic interactions with the plate[151]. Another approach that may allow for indirect detection of a radioactive decay process by a MC is based upon the absorption of photons to produce the heat that causes MC deflection. Chelating scintillation fibers could be used to convert the ionizing particles into photons. These photons could then be directed at a MC with a chemical film that is a strong absorber of the wavelength of the photons emitted by the chelating scintillation fiber. The heat produced by absorption of the photons should lead to deflections of the MC.

5.3 MATRIX ASSISTED PULSED LASER EVAPORATION (MAPLE)

The development of MC sensors is beginning to move toward the use of arrays of MCs to improve the selectivity of the devices. One factor limiting the development of these array systems is the ability to deposit different chemical recognition layers onto adjacent MCs in a spatially dense array. Techniques used to coat MCs at this time (spin coating, PVD, SAM formation) lack the spatial resolution to be able to put different phases on individual, adjacent MCs. One technique that appeared to be a promising tool in overcoming this problem is the technique known as matrix assisted pulsed laser evaporation (MAPLE). MAPLE

is a descendant of pulsed laser deposition (PLD) techniques used to deposit thin films of metals, that uses an energy absorbing matrix like those used in matrix assisted laser desorption ionization mass spectrometry (MALDI-MS), to softly evaporate organic and biological materials intact. A method of using MAPLE to direct write (MAPLE DW) on a substrate has been developed and has been quoted to have spatial resolution of around 10nm[152-155]. The application of this technique to coating individual MC on an array was investigated.

Initial experiments were done in a vacuum chamber setup for typical PLD applications. A Lumonics PM-888 excimer laser was used with a Kr and F_2 gas mixture to produce a 256 nm wavelength emission. The Lumonics laser is capable of producing a 1 J photon burst. A target was prepared by dissolving a 10:1 ratio of the GC phase SP-2100 (methyl silicone), and a matrix material, polybutylmethylacrylate (PBMA) in t-butyl alcohol. This solution was then placed in a Teflon mold and frozen using liquid nitrogen. The target was removed from the liquid nitrogen and positioned inside the vacuum chamber of the PLD system. A KBr pellet was fixed 180 degrees from the target and the chamber evacuated to $1e^{-5}$ torr. Figure 5.1 is a schematic of the instrument setup. The laser was focused onto the target and the target ablated with 50,000 pulses of the laser at 5 pulses per second with a laser fluence of 0.05 J/cm^2. After coating the target was removed and an IR spectra obtained and compared with that of the bulk SP-2100. These spectra are shown in Figure 5.2. These spectra show that using the matrix the SP-2100 phase was deposited with minimal damage to the structure.

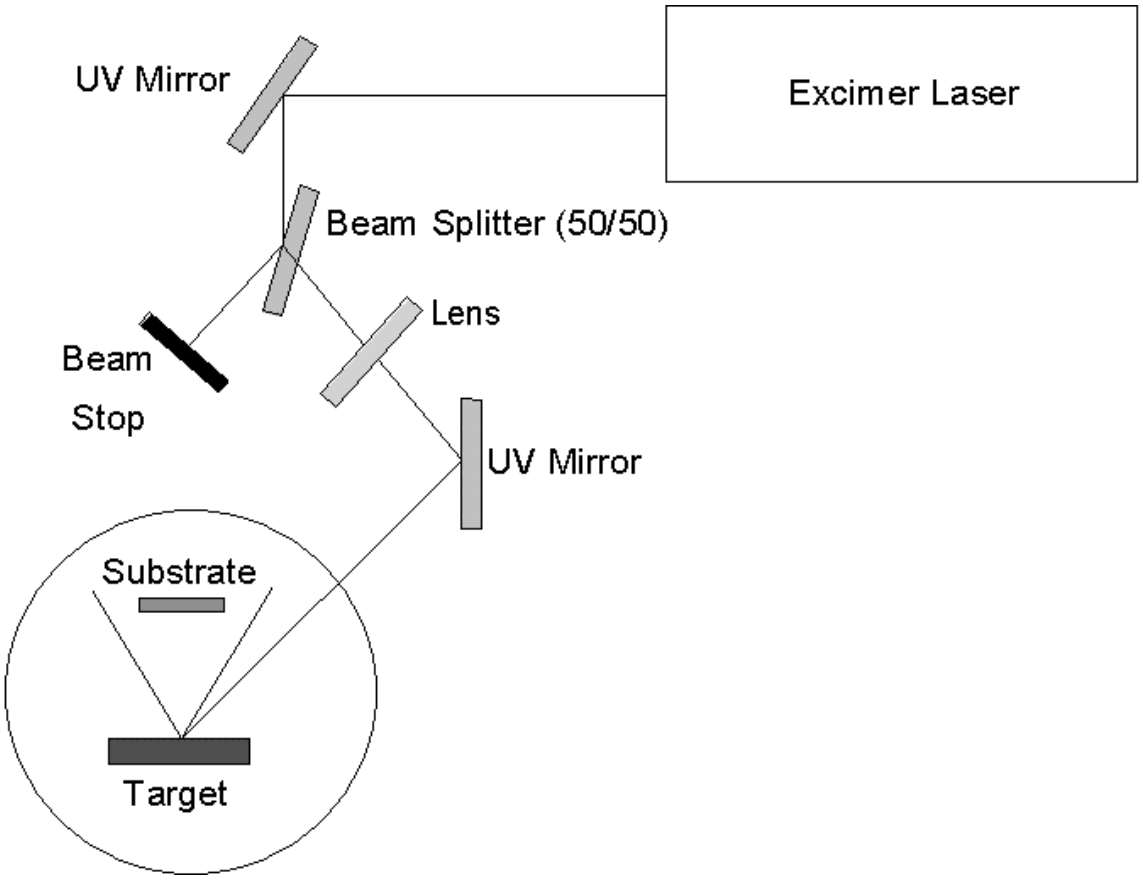

Figure 5.1 Schematic of vacuum pumped matrix assisted pulsed laser evaporation (MAPLE) system.

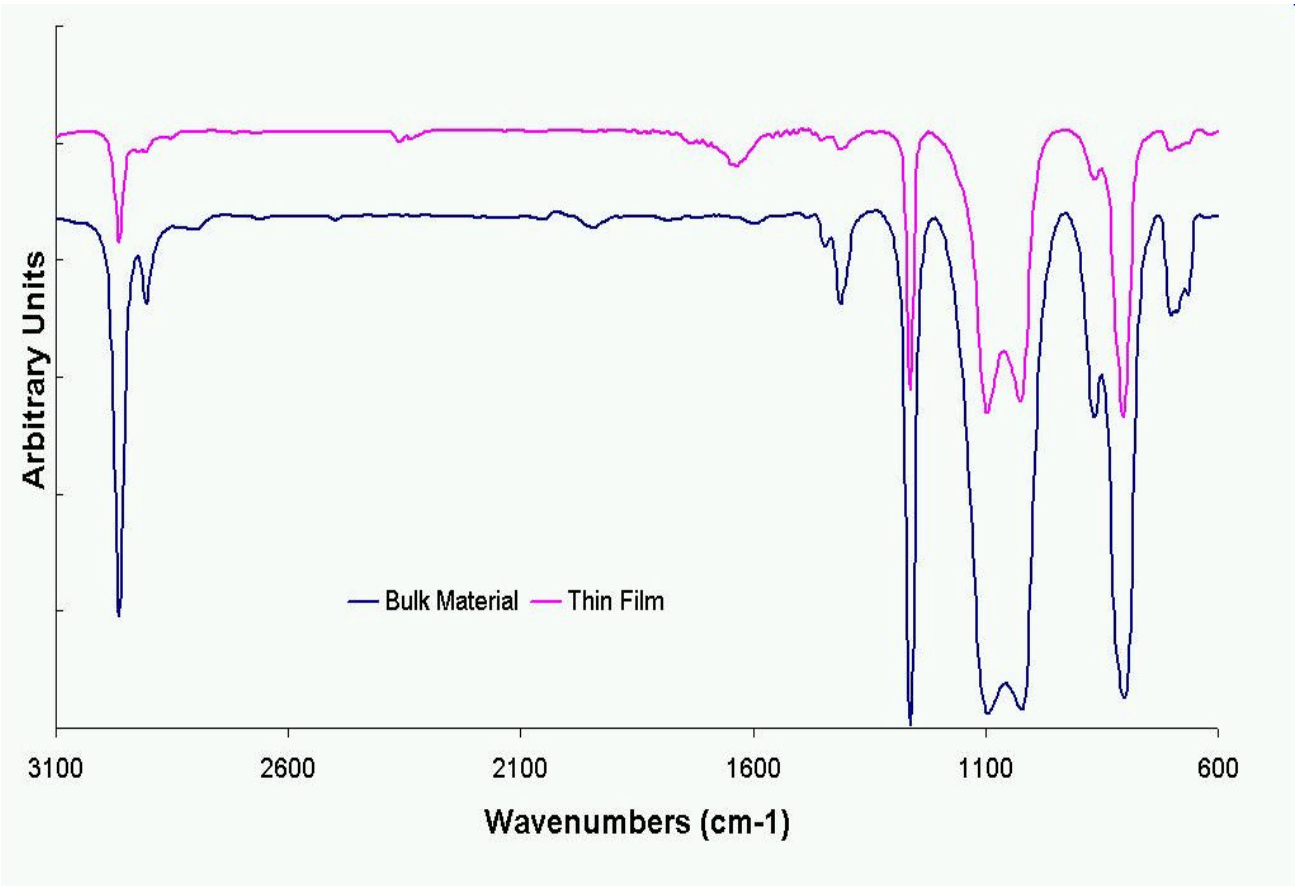

Figure 5.2 IR spectra of bulk SP-2100 and thin film of SP-2100 deposited by MAPLE technique.

To be able to deposit materials with controlled spatial resolution the setup had to be modified from that described previously. A setup similar to those described by Chrisey was constructed. In this setup the laser beam from the Lumonics excimer laser was spatially filtered by passing it through an iris. The spatially filtered beam was then reflected, using a UV grade mirror and a UV grade dichroic mirror toward a UV grade 10X microscope objective (LMU-10X-UVB) from Optic For Research (OFR) with a broadband antireflection coating. The microscope objective focused the beam onto a quartz target disk. The quartz target disk consisted of a commercially purchased quartz disk that had been spin coated with a film consisting of the GC phase SP-2100 and the absorbing matrix, polybutylmethylacrylate (PBMA) in a 10:1 ratio. The thin film was prepared by dissolving the 10:1 mixture of SP-2100 and PBMA in 10.0 ml of chloroform and dispensing 1.0 ml of this solution onto the quartz disk and thin spinning the quartz disk at 3000 rpm for 1 minute. This method produced quartz disks with a 5 μm thick film as measured by profilometry. The MCs were positioned in a Teflon mount below the quartz disk and the two were separated by a 25 μm thick spacer. Alignment of the MC under the laser beam was facilitated by two linear stages with stepping motors. The MC was imaged through the microscope objective and another lens onto a video CCD camera so that the process could be monitored and aligned properly. A schematic of this setup is shown in Figure 5.3. The focused laser spot was approximately 10 μm

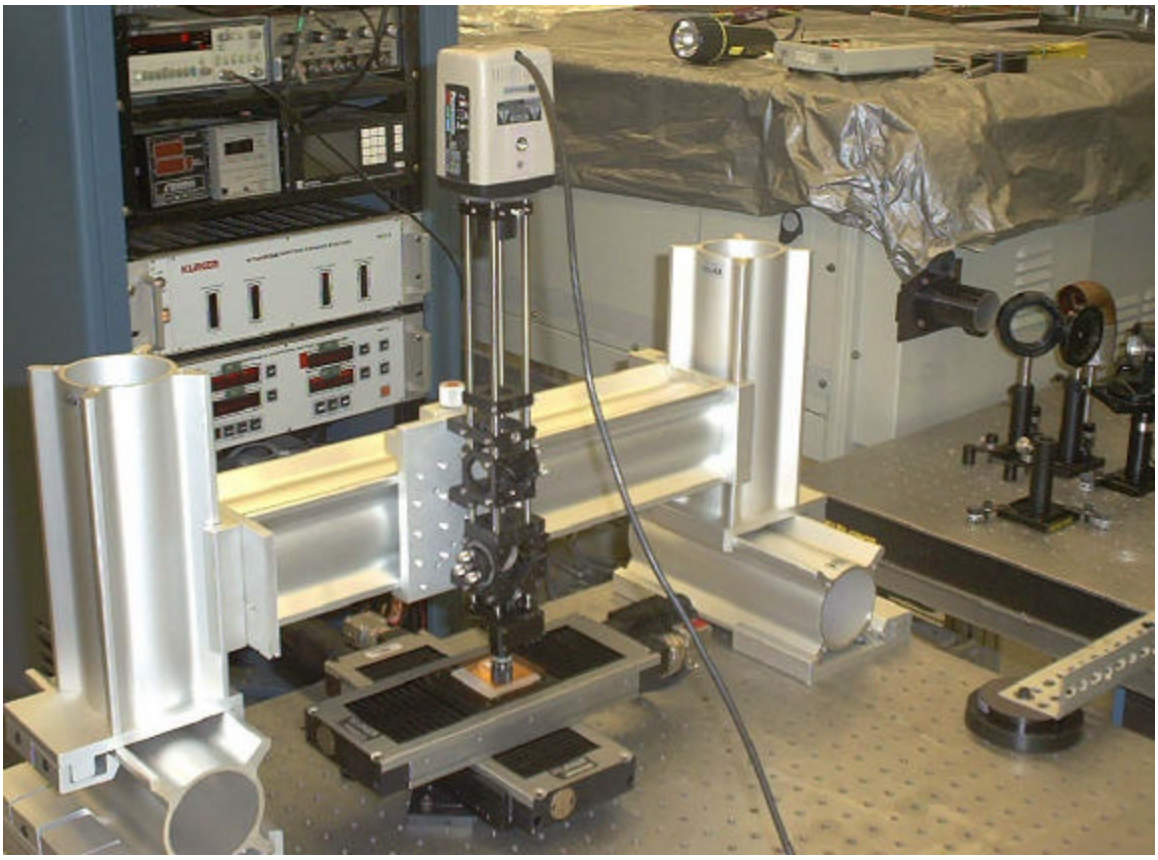

Figure 5.3 Image of setup for matrix assisted pulsed laser evaporation direct write (MAPLE-DW).

in diameter for an area of approximately 7.9 x 10^{-7} cm^2. To achieve a fluence of 0.05 J/cm^2 for this area only 39.5 μJ of energy are required at the target surface.

To achieve this most of the energy of the laser had to be removed before it was focused onto the target. To do this a 98% reflector was used to dump most of the beam energy into a beam stop, while the 2% of the energy that passed through the reflector was focused onto the target.

The problem that occurred with direct writing of materials onto the MCs was that at fluences where the thin film coatings on the quartz target were evaporated and transferred to the substrate, the MCs were destroyed or damaged; and at fluences where the MCs were not damaged, the thin film coatings were not transferred from the surface of the quartz target to the MCs. Additional difficulty was added, as the energy output of the excimer laser was not consistent from day to day, and the energy required at the target was very small and difficult to control optimally.

5.4. CONCLUDING REMARKS

Working in the area of sensor design and development has been a difficult and satisfying experience. The advancement of two different sensor transducers used for chemical sensors has been described in the previous chapters and though conclusions were presented in each of these chapters a few final thoughts on each of these topics and there future will be presented here.

The first combination of chelating resins with scintillation fibers to produce a sensor to selectively monitor metal ions in harsh, remote environments was accomplished. This sensor showed both good sensitivity and selectivity and simplified the sampling, extraction, concentration, and introduction steps generally required to measure a radioactive sample. This simplified process will significantly reduce worker handling and exposure to hazardous radioactive samples. This technique can be readily applied to nearly any radioactive metal ion, as long as a selective recognition layer for the metal is available and can be fixed to the surface of the scintillation fiber. One can envision an array of fibers coated with different selective phases capable of selectively binding different radioactive metals being used with CCD detectors to further reduce worker exposure by reducing sampling and measurement time requirements.

Structuring of MC surfaces has been shown to dramatically improve the magnitude of chemi-mechanical transduction mechanisms thus improving sensitivity of these devices over unstructured devices. It also has been shown that the scale of the features plays a part in the enhancement as smaller features provide lower LODs (disordered structures versus ordered structures). Other means of creating structured surfaces need to be investigated to see how they affect sensitivities. One method of interest is the codeposition of metal and organic materials via PVD techniques to create a mesh of organic and metals rather than distinct layers that have been used in the work described here. The development of such methods would only strengthen the understanding of the enhancement methods of these structured surfaces.

In conclusion, chemical sensors are a broadening area, utilizing many techniques from different disciplines of the science community. The use of chemical sensors will continue to increase as these devices are put to use in every imaginable situation to supply information about the chemical nature of our surroundings.

References

1. Diamond, D., Principles of Chemical and Biological Sensors, John Wiley & Sons, Inc., New York, 1998.

2. Janata, J. and Bezegh, A., *Anal. Chem.* **1988,** *60*,62R.

3. Hughes, W. S., *J. Am. Chem. Soc.* **1922,** *44*,2860.

4. Rulfs, C. L. and Elving, P. J., *J. Am. Chem. Soc.* **1951,** *73*,3287.

5. Elving, P. J. and Tang, C.-S., *J. Am. Chem. Soc.* **1950,** *72*,3241.

6. Elving, P. J. and Tang, C.-S., *J. Am. Chem. Soc.* **1950,** *72*,3244.

7. Clark, L., *Trans. Am. Soc. Artif. Intern. Organs* **1956,** *2*,41.

8. Clark, L. and Lyons, C., *Ann. N.Y. Acad. Sci.* **1962,** *148*,133.

9. King, W. H., *Anal. Chem.* **1964,** *36*,1735.

10. Thundat, T., Warmack, R. J., Chen, G. Y., and Allison, D. P., *Appl. Phys. Lett.* **1994,** *64*,2894.

11. Barnes, J. R., Stephenson, R. J., Welland, M. E., Gerber, C., and Gimzewski, J. K., *Nature* **1994,** *372*,79.

12. Kerridge, P. T., *Biochem. J.* **1925,** *19*,611.

13. Stow, R. W. and Randall, B. F., *Am. J. Physiol.* **1954,** *179*,678.

14. Guilbault, G. and Montavlo, J., *J. Am. Chem. Soc.* **1969,** *91*,2164.

15. Janata, J., *J. Am. Chem. Soc.* **1975,** *97*,2914.

16. Lubbers, D. W. and Opitz, N., *Z. Naturf.* **1975,** *30*,532.

17. Wohltjen, H. and Dessey, R., *Anal. Chem.* **1979,** *51*.

18. Peterson, J. I., Goldstein, S. R., Fitzgerald, R. V., and Buckhold, D. K., *Anal. Chem.* **1980,** *52*.

19. Schultz, J. S., Masouri, S., and Goldstein, I. J., *Diabetes Care* **1982,** *5*,245.

20. Sepaniak, M. J., Tromberg, B. J., and Eastham, J. F., *Clin. Chem.* **1983,** *29*,1678.

21. Belli, S. L. and Rechnitz, G. A., *Anal. Lett.* **1986,** *19*,403.

22. Headrick, J. J., Sepaniak, M. J., Alexandratos, S., and Datskos, P. G., *Anal. Chem.* **2000,** *72*,1994.

23. Curie, J. and Curie, P., *C.R. Acad. Sci., Paris* **1880,** *92*,294.

24. Danielsson, B. and Mattiasson, B., in Handbook of Chemical and Biological Sensors (Taylor, R. F. and Schultz, J. S., eds.), Institute of Physics Publishing, Bristol, UK, 1996.

25. Eggins, B. R., Chemical Sensors and Biosensors, John Wiley & Sons, LTD, London, 2002.

26. Danielsson, B. and Mosbach, K., *Methods Enzymol.* **1988,** *137*,181.

27. Danielsson, B., *J. Biotechnol.* **1990,** *15*,187.

28. Danielsson, B., Mattiasson, B., and Mosbach, K., *Appl. Biochem. Bioeng.* **1981,** *3*,97.

29. Mattiasson, B. and Danielsson, B., *Carbohdyr. Res.* **1982,** *102*,273.

30. Rank, M., Gram, J., and Danielsson, B., *Anal. Chim. Acta* **1993,** *281*,521.

31. Xie, B., Danielsson, B., Norberg, P., Winquist, F., and Lundstrom, I., *Sens. Actuat. B* **1992,** *6*,127.

32. Xie, B., Danielsson, B., and Winquist, F., *Sens. Actuat. B* **1993,** *15-16*,443.

33. Harborn, U., Xie, B., and Danielsson, B., *Anal. Lett.* **1994,** *27*,2639.

34. Amine, A., Xie, B., and Danielsson, B., *Anal. Lett.* **1995,** *28*,2275.

35. Jones, M. G. and Nevell, T. G., *Sens. Actuat.* **1989,** *16*,215.

36. Dabill, D. W., Gentry, S. J., and Walsh, P. T., *Sens. Actuat.* **1987,** *11*,135.

37. Gentry, S. J. and Walsh, P. T., *Sens. Actuat.* **1984,** *5*,239.

38. Catterall, R. W., Chemical Sensors, Oxford University Press, Oxford, UK, 1997.

39. Cassidy, J., F., Doherty, A. P., and Vos, J. G., in Principles of Chemical and Biological Sensors (Diamond, D., ed.), John Wiley & Sons, Inc., New York, 1998.

40. Bard, A. J. and Faulkner, L. R., Electrochemical Methods: Fundamentals and Applications, John Wiley & Sons, Inc., New York, 1980.

41. Wang, J., in Handbook of Chemical and Biological Sensors (Taylor, R. F. and Schultz, J. S., eds.), Institute of Physics Publishing, Bristol, UK, 1996.

42. Wang, J., *Electroanalysis* **1991,** *3*,255.

43. Turner, A. P. F., Karube, I., and Wilson, G. S., Biosensors: Fundamentals and Applications, Oxford University Press, Oxford, UK, 1987.

44. Ingle, J. D. J. and Crouch, S. R., Spectrochemical Analysis, Prentice Hall, New Jersey, 1988.

45. MacCraith, B. D., in Principles of Chemical and Biological Sensors (Diamond, D., ed.), John Wiley & Sons, Inc., New York, 1998.

46. Buerk, D. G., in Handbook of Chemical and Biological Sensors (Taylor, R. F. and Schultz, J. S., eds.), Institute of Physics Publishing, Bristol, UK, 1996.

47. Walczak, I. M., Love, W. F., Cook, T. A., and Slovacek, R. E., *Biosens. Bioelectron.* **1992,** *7*,39.

48. MacCraith, B. D., *Sens. Actuat. B* **1993,** *11*,29.

49. Walsh, J. E., MacCraith, B. D., Meaney, M., Vos, J. B., Regan, F., Lania, A., and Arjushenko, S., *SPIE Proc.* **1995,** *2508*,233.

50. Tromberg, B. J., Eastham, J. F., and Sepaniak, M. J., *Appl. Spectrosc.* **1984,** *38*,38.

51. Tromberg, B. J., Sepaniak, M. J., Alarie, J. P., Vo-Dinh, T., and Santella, R. M., *Anal. Chem.* **1988,** *60*,1901.

52. Tromberg, B. J., Sepaniak, M. J., Vo-Dinh, T., and Griffin, G. D., *Anal. Chem.* **1987,** *59*,1226.

53. Leutz, H., *Nucl. Instr. Meth. Phys. Res.* **1995,** *364*,422.

54. Knoll, G. F., Radiation Detection and Measurement, John Wiley & Sons, Inc., New York, 1979.

55. Sauerbrey, G. Z., *Z.Phys.* **1959,** *155*,206.

56. Forster, R., J., in Principles of Chemical and Biological Sensors (Diamond, D., ed.), John Wiley & Sons, Inc., New York, 1998.

57. Suleiman, A. A. and Guilbault, G. G., in Handbook of Chemical and Biological Sensors (Taylor, R. F. and Schultz, J. S., eds.), Institute of Physics Publishing, Bristol, UK, 1996.

58. Binnig, G., Quate, C. F., and Gerber, C., *Phys. Rev. Lett.* **1986,** *56*,930.

59. Thundat, T., Chen, G. Y., Warmack, R. J., Allison, D. P., and Wachter, E. A., *Anal. Chem.* **1995,** *67*,519.

60. Thundat, T. and Wachter, E. A., *Rev. Sci. Instrum.* **1995,** *66*,3662.

61. Thundat, T., Wachter, E. A., Sharp, S. L., and Warmack, R. J., *Appl. Phys. Lett.* **1995,** *66*,1695.

62. Davis, Z. J., Abadal, G., Kuhn, O., Hansen, O., Grey, F., and Bioisen, A., *J. Vac. Sci. Technol. B* **2000,** *18*,612.

63. Abadal, G., Davis, Z. J., Helbo, B., Borrise, X., Ruiz, R., Boisen, A., Campabadal, F., Esteve, J., Figueras, E., Perez-Murano, F., and Barniol, N., *Nanotechnology* **2001,** *12*,100.

64. Hugel, T., Holland, N. B., Cattani, A., Moroder, L., Seitz, M., and Gaub, H. E., *Science* **2002,** *296*,1103.

65. Ilic, B., Czaplewski, D., Zalalutdinov, M., Craghead, H. G., Neuzil, P., Campagnolo, C., and Batt, C., *J. Vac. Sci. Technol. B* **2001,** *19*,2825.

66. Viani, M. B., Pietrasanta, L. I., Thompson, J. B., Chand, A., Gebeshuber, I. C., Kindt, J. H., Richter, M., Hansma, H. G., and Hansma, P. K., *Nature Structural Biology* **2000,** *7*,644.

67. Albrecht, T. R., Grutter, P., Horne, D., and Rugar, D., *J. Appl. Phys.* **1991,** *69*,668.

68. Fritz, J., *Langmuir* **2001,** *16*,9694.

69. Fritz, J., Baller, M. K., Lang, H. P., Rothuizen, H., Vettiger, P., Meyer, E., Güntherodt, H.-J., Gerber, C., and Gimzewski, J. K., *Science* **2000,** *288*,316.

70. Butt, H.-J., *J. Colloid Interface Sci.* **1996,** *180*,251.

71. Raiteri, R., Butt, H.-J., and Grattarola, M., *Electrochim. Acta* **2000,** *46*,157.

72. Stoney, G. G., *Proc. R. Soc. London* **1909,** *A82*,172.

73. Brouns, T., in EMSP-TFA Workshop, Hanford, WA, 1998.

74. Bonnessen, P. V., Moyer, B. A., Presley, D. J., Armstrong, V. S., Haverlock, T. J., Counce, R. M., and Sachleben, R. A., Alkaline-Side Extraction of Technetium from Tank Waste Using Crown Ethers and Other Extractants, ORNL/TM-13241, 1996

75. Marsh, S. F., Svitra, Z. V., and Bowmen, S. M., *J. Radioanal. Nucl. Chem.* **1995,** *194*,117.

76. DOE, Integrated Data Base Report-1996: U.S. Spent Nuclear Fuel and Radioactive Waste Inventories, Projections, and Characteristics, DOE/RW-0006, Rev. 13, December 1997

77. Bunker, B., Virden, J., Kuhn, B., and Quinn, R., in Encyclopedia of Energy Technology and the Environment, John Wiley & Sons, Inc., New York, 1995, p. 2023.

78. Beauvais, R.,Ph.D. Dissertation,University of Tennessee,**1996**

79. Alexandratos, S. D., *Sep. and Purif. Meth.* **1988,** *17*,67.

80. Zhang, Z., Yank, M., and Pawliszyn, J., *J. Anal. Chem.* **1994,** *66*,844A.

81. Kocher, D. C., Radioactive Decay Tables - A Handbook of Decay Data for Application to Radiation Dosimetry and Radiological Assessment, 1981

82. Overman, R. T. and Clark, H. M., Radioisotope Techniques, McGraw-Hill Book Company, Inc., New York, 1960.

83. Bicron, Standard Plastic Scintillating Wavelength Shifting Optical Fibers, www.bicron.com/stdwaveopticalfiber.htm, 1999

84. Carlson, C. D., Comparison of Organic and Inorganic Ion Exchangers for Removal of Cs and Sr from Simulated and Actual Hanford 241-AW-101 DSSF Tank Waste, PNL-10920, 1996

85. Simon, G. P., Ion Exchange Training Manual, Van Nostrand Reinhold, New York, 1991.

86. Lehto, J. and Harjula, R., *React. & Funct. Polym.* **1995,** *27*,121.

87. Bartsch, R. A. and etal, *Anal. Chem* **1999,** *71*,672.

88. Diaz, M., Fernandez, A., Rendueles, M., and Rodrigues, A., *Ind. Eng. Chem. Res.* **1994,** *33*,2789.

89. Christensen, J. J. and etal, *Sep. Sci. Technol.* **1981,** *16*,1193.

90. Chiazrizia, R., Horwitz, E. P., Beauvais, R. A., and Alexandratos, S. D., *Sol. Extr. & Ion Exch.* **1998,** *16*,875.

91. Berger, R., Delamarche, E., Lang, H. P., Gerber, C., Gimzewski, J. K., Meyer, E., and Güntherodt, H.-J., *Science* **1997,** *276*,2021.

92. Datskos, P. G. and Sauers, I., *Sens. Actuat. B* **1999,** *61*,75.

93. Raiteri, R., Nelles, G., Butt, H.-J., Knoll, W., and Skládal, P., *Sens. Actuat. B* **1999,** *61*,213.

94. Baller, M. K., Lang, H. P., Fritz, J., Gerber, C., Gimzewski, J. K., Drechsler, U., Rothuizen, H., Despont, M., Vettiger, P., Battiston, F. M.,

Ramseyer, J.-P., Fornaro, P., Meyer, E., and Güntherodt, H.-J., *Ultramicroscopy* **2000,** *82*,1.

95. Ji, H.-F., Finot, E., Dabestani, R., Thundat, T., Brown, G. M., and Britt, P. F., *Chem. Commun.* **2000,**457.

96. Moulin, A. M., Shea, S. J., and Welland, M. E., *Ultramicroscopy* **2000,** *82*,23.

97. Harris, J. G. E., Awschalom, D. D., Maranowski, K. D., and Gossard, A. C., *Rev. Sci. Instrum.* **1996,** *67*,3591.

98. Varesi, J., Lai, J., Perazzo, T., Shi, Z., and Majumdar, A., *Appl. Phys. Lett.* **1997,** *71*,306.

99. Betts, T. A., Tipple, C. A., Sepaniak, M. J., and Datskos, P. G., *Anal. Chim. Acta* **2000,** *422*,89.

100. Fagan, B., Tipple, C. A., Xue, B., Datskos, P., and Sepaniak, M., *Talanta* **2000,** *53*,599.

101. Freeman, R. G., Graber, K. C., Allison, K. J., Bright, R. M., Davis, J. A., Guthrie, A. P., Hommer, M. B., Jackson, M. A., Smith, P. C., Walter, D. G., and Natan, M. J., *Science* **1995,** *267*,1629.

102. Grabar, K. C., Allison, K. J., Baker, B. E., Bright, R. M., Brown, K. R., Freeman, R. G., Fox, A. P., Keating, C. D., Musick, M. D., and Natan, M. J., *Langmuir* **1996,** *12*,2353.

103. Elghanian, R., Storhoff, J. J., Mucic, R. C., Letsinger, R. L., and Mirkin, C. A., *Science* **1997,** *277*,1078.

104. Liu, J., Mendoza, S., Roman, E., Lynn, M. J., Xu, R. L., and Kaifer, A. E., *J. Am. Chem. Soc.* **1999,** *121*,4304.

105. Velev, O. D., Tessier, P. M., Lenhoff, A. M., and Kaler, E. W., *Nature* **1999,** *401*,548.

106. Israelachvili, J., Intermolecular and Surface Forces, Academic Press, San Diego, 1991.

107. Frink, L. J. D. and Swol, F. v., *Langmuir* **1999,** *15*,3296.

108. Sivasankar, S., Brieher, W., Lavrik, N., Gumbiner, B., and Leckband, D., *In: Proceedings of the National Academy of Sciences of the United States of America* **1999,** *96*,11820.

109. Lavrik, N. and Leckband, D., *Langmuir* **2000,** *16*,1842.

110. Rojas, M. T., Koniger, R., Stoddart, J. F., and Kaifer, A. E., *J. Am. Chem. Soc.* **1995,** *117*,336.

111. Beulen, M. W. J., Bugler, J., Jong, M. R. d., Lammerink, B., Huskens, J., Schonherr, H., Vancso, G. J., Boukamp, B. A., Wieder, H., Offenhauser, A., Knoll, W., Veggel, F. v., and Reinhoudt, D. N., *Chem. A Eur. J.* **2000,** *6*,1176.

112. Li, R. and Sieradzki, K., *Phys. Rev. Lett.* **1992,** *68*,1168.

113. Lavrik, N. V., Tipple, C. A., Datskos, P. G., and Sepaniak, M. J., *Biomed. Microdevices* **2001,** *3*,35.

114. Dickert, F. L., Hayden, O., and Zenkel, M. E., *Anal. Chem.* **1999,** *71*,1338.

115. Lee, J.-Y. and Park, S.-M., *J. Phys. Chem. B* **1998,** *102*,9940.

116. Copper, C. L., Davis, J. B., Cole, R. O., and Sepaniak, M. J., *Electrophoresis* **1994,** *15*,785.

117. Widrig, C. A., Chung, C., and Porter, M. D., *J. Electroanal. Chem.* **1991,** *310*,335.

118. Maute, M., Raible, S., Prins, F. E., Kern, D. P., Weimar, U., and Göpel, W., *Microelectron. Eng.* **1999,** *46*,439.

119. Britton, C. L., Jones, R. L., Oden, P. I., Hu, Z., Warmack, R. J., Smith, S. F., Bryan, W. L., and Rochelle, J. M., *Ultramicroscopy* **2000,** *82*,17.

120. Datskos, P. G., Sepaniak, M. J., Tipple, C. A., and Lavrik, N., *Sens. Actuat. B* **2001,** *76*,393.

121. Jensenius, H., Thaysen, J., Rasmussen, A. A., Veje, L. H., Hansen, O., and Boisen, A., *Appl. Phys. Lett.* **2000,** *76*,2615.

122. Luginbuhl, P., Racine, G.-A., Lerch, P., Romanowicz, B., Brooks, K. G., Rooij, N. F. d., Renaud, P., and Setter, N., *Sens. Actuat. A* **1996,** *54*,530.

123. Boisen, A., Thaysen, J., Jensenius, H., and Hansen, O., *Ultramicroscopy* **2000,** *82*,11.

124. Ji, H.-F., Hansen, K. M., Hu, Z., and Thundat, T., *Sens. Actuat. B* **2001,** *72*,233.

125. Ibach, H., *Surf. Sci. Rep.* **1997,** *29*,193.

126. Shuttleworth, R., *Proc. Phys. Soc. (London)* **1950,** *63A*,444.

127. Tipple, C. A., Lavrik, N. V., Culha, M., Headrick, J., Datskos, P., and Sepaniak, M. J., *Anal. Chem.* **2002,** *In Press*.

128. Seidel, H., Csepregi, L., Heuberger, A., and Baumgartel, H., *J. Electrochem. Soc.* **1990,** *137*,3612.

129. Kovacs, G. T. A., Micromachined Transducers Sourcebook, WCB McGraw-Hill, Boston, 1998.

130. Xu, J. and Steckl, A. J., *Appl. Phys. Lett.* **1994,** *65*,2081.

131. Brugger, J., Belajakovic, G., Despont, M., de Rooij, N. F., and Vettiger, P., *Microelectron. Eng.* **1997,** *35*,401.

132. Steckl, A. J., Mogul, H. C., and Mogren, S., *Appl. Phys. Lett.* **1992,** *60*,1833.

133. Steckl, A. J., Xu, J., Mogul, H. C., and Mogren, S., *Appl. Phys. Lett.* **1992,** *62*,1982.

134. Jarausch, K. F., Stark, T. J., and Russell, P. E., *J. Vac. Sci. Technol. B* **1996,** *14*,3425.

135. Schmidt, B., Bischoff, L., and Teichert, J., *Sens. Actuat. A* **1997,** *61*,369.

136. Nakano, S., Nakagawa, S., Iskikawa, H., and Ogiso, H., *Nucl. Instrum. Methods Phys. Res. B* **2001,** *175-177*,777.

137. Nakano, S., Ogiso, H., Sato, H., and Nakagawa, S., *Surf. Coat. Technol.* **2000,** *128-129*,71.

138. Culha, M.,Ph.D. Dissertation,University of Tennessee,**2002**

139. Takeo, K., Mitoh, H., and Uemura, K., *Carbohdyr. Res.* **1989,** *187*,203.

140. Patrash, S. J. and Zellers, E. T., *Anal. Chem.* **1993,** *65*,2055.

141. Hu, Z., Thundat, T., and Warmack, R. J., *J. Appl. Phys.* **2001,** *90*,427.

142. Copper, C. L., Davis, J. B., and Sepaniak, M. J., *Chirality* **1995,** *7*,401.

143. Fox, S. B., Culha, M., and Sepaniak, M. J., *J. Liq. Chromatogr. Related Technol.* **2001,** *24*,1209.

144. Culha, M., Fox, S., and Sepaniak, M. J., *Anal. Chem.* **2000,** *72*,88.

145. Lelièvre, F., Gareil, P., and Jardy, A., *Anal. Chem.* **1997,** *69*,385.

146. Tomishenko, S., Theory of Plates and Shells, McGraw-Hill, 1940.

147. Fabian, J.-H., Scandella, L., Fuhrmann, H., Berger, R., Mezzacasa, T., Musil, C., Gobrecht, J., and Meyer, E., *Ultramicroscopy* **2000,** *82*,69.

148. Raiteri, R., Grattarola, M., Butt, H.-J., and Skládal, P., *Sens. Actuat. B* **2001,** *79*,115.

149. Moulin, A. M., Stephenson, R. J., and Welland, M. E., *J. Vac. Sci. Technol. B* **1997,** *15*,590.

150. Gimzewski, J. K., Gerber, C., Meyer, E., and Schlittler, R. R., *Chem. Phys. Lett.* **1994,** *217*,589.

151. Stephan, A. C., Gaulden, T., Brown, A.-D., Smith, M., Miller, L. F., and Thundat, T., *Rev. Sci. Instrum.* **2002,** *73*,36.

152. Chrisey, D. B., Pique, A., Modi, R., Wu, H. D., Auyeung, R. C. Y., and Young, H. D., *Appl. Surf. Sci.* **2000,** *168*,345.

153. Fitz-Gerald, J. M., Pique, A., Chrisey, D. B., Rack, P. D., Zeleznick, M., Auyeung, R. C. Y., and Lakeou, S., *Appl. Phys. Lett.* **2000,** *76*,1386.

154. Pique, A., Chrisey, D. B., Auyeung, R. C. Y., Fitz-Gerald, J. M., Wu, H. D., McGill, R. A., Lakeou, S., Wu, P. K., Nguyen, V., and Duignan, M., *Appl. Phys. A* **1999,** *69*,S279.

155. Pique, A., Chrisey, D. B., Fitz-Gerald, J. M., McGill, R. A., Auyeung, R. C. Y., Wu, H. D., Nguyen, V., Chung, R., and Duignan, M., *J. Mater. Res.* **2000,** *15*,1872.

VITA

Joseph Jeremy Headrick was born in Wurzburg, Germany on December 8, 1972, while his father served in the U.S. Army. He attended schools in the Sullivan County School System in Kingsport, TN, where he graduated from Sullivan South High School in June 1991. He entered East Tennessee State University in Johnson City, TN during the Fall of 1991 and in May of 1997 he received the Bachelor of Science in Chemistry. He entered the Doctorate program in Chemistry at the University of Tennessee, Knoxville in August 1997 undertaking research in analytical chemistry. He earned his Ph.D. in Chemistry in May 2003 and was employed as an analytical chemist with ATK Thiokol Propulsion in Promontory, Utah.